Part I: A Novel Compact Water Tunnel

Part II: Evolution of Delta Wing Surface Contour from Flat Plates to Boxfish at Low Reynolds Numbers

Thesis by
Sean Patrick Devey

In Partial Fulfillment of the Requirements for the
Degree of
Doctor of Philosophy

CALIFORNIA INSTITUTE OF TECHNOLOGY
Pasadena, California

2026
Defended July 14th, 2025

Sean Patrick Devey
ORCID: 0000-0002-8937-939X

ACKNOWLEDGEMENTS

Thank you to the Center for Autonomous Systems and Technologies (CAST) and NSF GRFP under grant no. DGE-1745301 for funding this work.

Measurement Sciences Enterprises, Inc. provided a miniLDV system which became essential to the tunnel characterization work and for measuring freestream speeds in subsequent tests. Integrated Design Tools, Inc. provided XStream Mini cameras at a discount, which were used in nearly all of the delta wing experiments.

Far too many people have helped me get to this point than can possibly be covered in a few pages, and my memory probably isn't good enough to do all of them justice. In the interest of brevity, I would like to offer my thanks and acknowledgment to the following abbreviated list.

First I must offer my sincerest gratitude to my committee: Dr. Tim Colonius, Dr. John Dabiri, Dr. John Sader, candidacy committee member Dr. Michael Dickinson, and my thesis advisor Dr. Morteza Gharib. All of you have taught me to be a better scientist. I have enjoyed our many discussions and sincerely appreciate your mentorship.

Mory in particular deserves thanks for his unwavering support and guidance through all the struggles and victories I experienced through the last five years, both within the lab and without. I could not have asked for a better mentor.

To our collaborators on the boxfish-inspired delta wing project, including committee members Dr. John Sader, Dr. Tim Colonius, Dr. Nitay Ben Shachar and Alex Nunn. Particular thanks to Caroline Cardinale, whose simulations have been tremendously useful to me, providing the first evidence of the counter-rotating vortices on the aft end of certain wings.

To the Dabiri research group, who have been generous with sharing their lab equipment and expertise, particularly Roni Goldschmit who was very helpful in setting up the constant temperature anemometer.

To the talented undergraduates who helped build two iterations of thruster arrays, characterize the tunnel, and were patient with me as I learned how to be a research mentor: Citli Carrera Arenas, Sarah Bass, Shana Hartwick, and Hannah Park.

To the friends who have made my years in Pasadena so memorable. I do not know where I would be without your support. Special thanks to the boys at Harkness, friends on Chester and Marion, and the Caltech Rugby Club.

To my friends in the 2020 GALCIT first year co-hort, without whom I might still be struggling to understand some arcane problem set to this day.

To my friends and fellow members of the Gharib research group. Most of you have fielded silly questions from me without judgment, and provided incredibly useful insights without which this work would have either been very different, or would have at least taken a lot longer. Most helped me hoist a test-section or thruster array up into an aquarium tank at some point or another. In particular: to David Jeon, whose expertise with experimental techniques and boundless patience is the stuff of legend; to Reza Nemovi, who suggested that perhaps I could make the thruster array a series of columns which can slot in and out of a frame; to many more senior lab members who taught me how to find Mory and made me feel welcome; to Meredith Hooper, with whom I first cut my teeth on research in the Gharib lab on the fishbot project, and who was always willing to be bothered as my office mate; to Alejandro Stefan-Zavala who is a constant source of joy, support, and funny doodles; and above all to Scott Bollt, who was always the first person I would turn to when I got stuck and often the person who gave me the best advice, not to mention his generosity and acumen with the experimental facility that we spent years together building.

To Sarah Pontes and Karima Guthrie, without whom all of my work would have been impossible and not to mention much less pleasant.

To the GALCIT community, which always made me feel welcome and were sometimes generous enough to laugh at my jokes.

To my previous advisors at The University of Alabama, Dr. J. Paul Hubner and Dr. Amy W. Lang, who introduced me to experimental fluid mechanics research, believed in me even when I had no idea what I was doing, and encouraged me to go to graduate school.

To the many teachers, coaches, and mentors who have worked hard to teach me to be curious, and helped shape the person I am today.

To my friends from The University of Alabama, particularly Andrew Bonacci and Mitch Johnson, who made getting a PhD sound like not such a bad idea.

To all of my family, particularly my parents who managed to trick me into loving to learn and always supported my decisions, and my siblings Luke, Ryan, Cate, Adam, and Heather, who are the best.

This thesis is presented in two parts.

Part I (Chapters 1–2) addresses a common challenge for experimentalists: the scarcity of laboratory space. Inspired by recent advances in fan-array wind tunnels, a novel, ultra-compact water tunnel was developed that uses an array of submerged thrusters to drive flow within a rectangular tank. Prioritizing space efficiency over power efficiency, the design achieves flow quality comparable to traditional facilities while occupying just 8% of the typical footprint. Flow characterization using particle image velocimetry (PIV), hot-film anemometry, and laser Doppler velocimetry (LDV) demonstrates the tunnel's effectiveness and suitability for fluid dynamic research.

Part II (Chapters 3–5) uses this new facility to investigate the aerodynamics of delta wings with extreme leeward surface contours in low Reynolds number subsonic flow. While the canonical delta wing flow field is dominated by a pair of counter-rotating leading-edge vortices (LEVs), similar vortex structures have been observed over a range of geometries—including biological forms such as boxfish. However, the influence of non-uniform thickness and large leeward surface deformations on LEV behavior remains poorly understood.

To address this, a family of 70° sweep delta wing shapes was defined using Bézier splines, spanning a continuum from flat plates to forms approaching bluff bodies. Eight 3D-printed wing models were fabricated, with systematic variation in cross-sectional curvature and thickness, including a conical apex section with a thickness-to-span ratio of 0.5. Dye visualization, stereoscopic PIV (SPIV), and load cell measurements were used to examine LEV strength, position, and wing performance across multiple angles of attack. Results show that increasing the leeward surface height, effectively confining the LEV, leads to substantial reductions in vortex strength and shifts in vortex position. Experimental evidence of a dual primary vortex structure over thick delta wings is reported for the first time. Tomographic dye reconstructions reveal complex three-dimensional vortex behavior in the aft section of the wings, including flow separation patterns reminiscent of those seen in hatchbacks and Ahmed bodies. Force measurements reflect the observed flow field, with highly non-linear force evolution with angle of attack depending on model cross-sectional and longitudinal profiles. These findings provide new insight into the interplay between surface shape and vortex structure, and further demonstrate the capabilities of the compact flow facility.

Devey, Sean and Morteza Gharib (Jan. 2025). “A large test section low-speed water tunnel in a small package”. In: *Experiments in Fluids* 66.2, p. 35. ISSN: 1432-1114. DOI: 10.1007/s00348-025-03959-5. URL: https://doi.org/10.1007/s00348-025-03959-5.

LIST OF ILLUSTRATIONS

Number *Page*

Number *Page*

Γ	circulation.
κ	vortex confinement parameter.
Λ	leading edge sweep.
ω	vorticity.
ρ	density.
θ	tangent angle of inflection point on wing surface cross-section relative to y-axis.
AOA	angle-of-attack.
b	wing span.
c	wing chord.
c_D	drag coefficient.
c_L	lift coefficient.
c_M	pitching moment coefficient about x/c=0.5.
c_N	normal force coefficient.
c_T	tangential force coefficient.
D	drag force.
h	test section height (water depth).
L	lift force.
MAC	mean aerodynamic chord, $\int_0^b c(y)dy/S$.
N	normal force.
P_i	wing surface centerline profile 2-deg Bezier spline control points.
q	dynamic pressure.
Q_i	wing surface cross-section 3-deg Bezier spline control points.
S	wing planform area.
T	tangential force.

u local freestream velocity.

U, U_∞ mean freestream velocity.

U_x out of plane velocity.

U_z vertical in-plane velocity.

u_{rms} velocity rms ($\sqrt{\overline{(u-U)^2}}$.

w test section width.

X, Y, Z lab frame coordinates.

x, y, z body-fixed coordinates.

y_i spanwise location of inflection point on wing surface cross-section.

y_{LEV} y-axis location of LEV.

y_{LE} local semi-span, $x/tan(\Lambda)$.

z_0 height of wing surface at y=0.

z_{LEV} z-axis location of LEV.

CTA Constant Temperature Anemometry.

DPIV Digital Particle Image Velocimetry.

FLOWTUB Free-surface Low-speed Optically-accessible Water TUnnel in a Box.

FMS Flow Management System.

LDV Laser Doppler Velocimetry.

Part I

A Novel Compact Water Tunnel

Devey, Sean and Morteza Gharib (Jan. 2025). “A large test section low-speed water tunnel in a small package”. In: *Experiments in Fluids* 66.2, p. 35. ISSN: 1432-1114. DOI: 10.1007/s00348-025-03959-5. URL: https://doi.org/10.1007/s00348-025-03959-5.

BACKGROUND AND METHODS

1.1 Introduction

Background

Low speed water tunnels are common facilities for a wide range of experimental studies ranging from biological swimming to fundamental fluid mechanics. Water tunnels exist to create a (typically steady and uniform) flow of water through the test section. Typical water tunnels require large supporting elements to accomplish this goal (R. Gordon and Imbabi, 1998), which means that the footprint of the full tunnel is much larger than the test section (Figure 1.1a).

The overall size of a tunnel is generally understood as a trade-off with flow quality and power efficiency (Barlow, Rae, and Pope, 1999). The typical design philosophy for a closed-circuit tunnel is to contract the flow into the test section and to minimize flow separation, which involves devoting most of the tunnel footprint to carefully designed diffusers, corners, and contraction sections (Barlow, Rae, and Pope, 1999; Mehta and Bradshaw, 1979; Cattafesta, Bahr, and Mathew, 2010). A larger tunnel (larger contraction ratio) tends to produce more uniform, lower turbulence flow (Breuer et al., 2022; Mehta and Bradshaw, 1979). Larger contraction ratios also reduce flow speeds before the contraction, which garners efficiency benefits for screens and honeycombs at that location (Mehta and Bradshaw, 1979).

Small water tunnels common in academic laboratories often achieve a somewhat reduced footprint by replacing the return section with relatively small diameter piping, at the cost of power efficiency (Da Silva Ássi et al., 2005; Sargison et al., 2009). To some extent, designers of wind and water tunnels have also been successful at reducing tunnel diffuser size using screens to counter the adverse pressure gradient associated with rapid expansion of the flow (Mehta and Bradshaw, 1979; Breuer et al., 2022). In general, past efforts to create compact water tunnels have either sacrificed flow quality (Zahari and Dol, 2015; Persen and Saetran, 1983), or presented only marginal improvements to overall tunnel size (R. Gordon and Imbabi, 1998).

Compact open-return wind tunnels composed of an array of independent fans have become popular over the past several decades. To the knowledge of the authors, the first computer-controlled multi-fan tunnels were built at Miyazaki University in 1993 and included relative modest 2:1 contractions (Nishi, Miyagi, and Higuchi, 1993). Early computer fan tunnels with no contraction

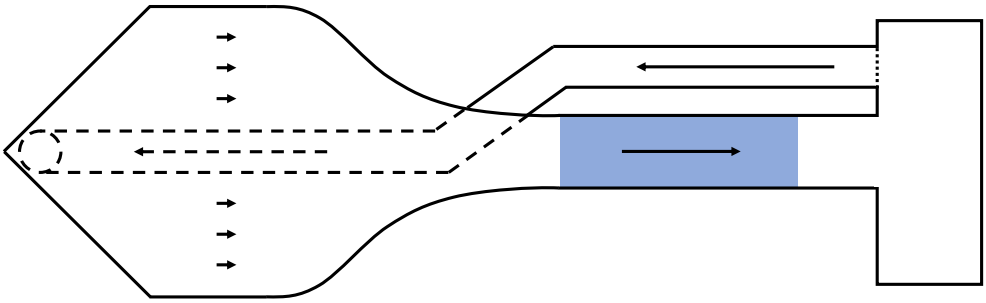

(a) ELD 505

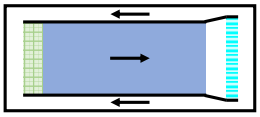

(b) FLOWTUB

Figure 1.1 To-scale top view schematic of a representative traditional low speed water tunnel design (Engineering Laboratory Design (ELD) 505, top) compared with the FLOWTUB tunnel (bottom). Test sections (blue) have the same 61x61cm cross-sectional area. Flow direction is indicated by arrows. In the FLOWTUB design, flow through the test section is driven in suction by an array of submersible electric thrusters (cyan stripes), returns around the outside of the test section, and passes through a flow management system (FMS, green grid) at the test section inlet. The FLOWTUB is also capable of operating in reverse (blowdown) to generate spatially and temporally non-uniform flows.

and uniform fan inputs were built at the Strategic Air Command Museum in Nebraska and the University of Kentucky, followed by similar tunnels with row-wise control at Oklahoma State University in 2009 (E. Johnson and Jacob, 2009) and at Caltech in 2011 (Kim et al., 2013). A tunnel in which the angle of the driving fans is modulated was developed at Tianjin University in 2015 (Jia-Ying et al., 2015), and large arrays of independently-controlled fans were developed by Caltech students for the Center for Autonomous Systems and Technologies (CAST) facility in 2017 and to test the Ingenuity Mars Helicopter within the confines of a vacuum chamber in 2018 (Dougherty, 2022; Veismann et al., 2021). Since then, fan array wind tunnels have become commonplace (Noca et al., 2019; L'Ecuyer, 2021; Olejnik et al., 2022; Li et al., 2023).

Objective

The current work takes inspiration from this growing body of compact wind tunnel research to develop a low cost, low speed, free-surface research water tunnel with comparable flow quality to a typical academic free surface tunnel (uniformity $< \pm 5\%$, turbulence intensity $<1\%$) but with a test section to total volume ratio an order of magnitude higher than traditional tunnels. It is also

desirable that the tunnel be capable of producing a wide range of flow velocities. Lower limits on tunnel speed are often imposed by the minimum rpm of the driving pump, and flow quality concerns due to the common issue of persistent low-frequency slosh. At higher speeds, flow visualization by dye injection becomes increasingly difficult due to increased turbulent diffusion. The best dye visualization results are obtained for flow speeds less than 15 cm/s (M. Ol, 2001). Another potential concern is free-surface waves in the test section, which become problematic at around the same speed. For these reasons, the design goal of the tunnel was a top speed of only 20 cm/s, with a minimum speed of less than 1 cm/s. In addition, the new tunnel design should be simpler and less expensive to manufacture than traditional designs and must offer maximal optical access to the test section. An additional goal was to minimize the upfront engineering cost, which was enabled by eschewing a bespoke contraction and turning vanes. This design will heretofore be referred to as FLOWTUB: Free-surface, Low-speed, Optically-accessible, Water TUnnel in a Box.

Thruster Array Tunnel Concept

To allow for a dramatically smaller footprint for a given test section size, this work demonstrates a new type of low speed closed-circuit water tunnel which aims to maximize test section size while minimizing construction cost and complexity and maintaining acceptable flow quality. Comparable flow quality to much larger traditional tunnels is maintained through the use of a novel drive system consisting of an array of electric thrusters and aggressive flow conditioning.

In contrast to traditional tunnel designs, this tunnel does not employ a contraction section, turning sections, or settling chambers. Asymmetries associated with aggressive flow turning are minimized by wrapping the return path around both sides and underneath the test section (Figure 1.1b). This arrangement allows the entire tunnel to be contained within a single rectangular tank, and each tunnel component to be placed inside this tank with less regard towards waterproofing than is typically necessary. In general, the test section size within the tank is maximized at the expense of power efficiency.

Driving fluid flow creates flow structures on the spatial and temporal scales of the propeller/impeller blades. Because smaller flow structures tend to dissipate more readily, it is desirable to minimize propeller size. At the same time, the test section area should be large relative to the propeller area, and bulky area-changing sections (contraction and diffusers) should be avoided to minimize total footprint. These goals are realized using an array of electric thrusters to drive the flow rather than a single larger pump. Each thruster consists of a brushless electric motor which drives a propeller inside a duct. The motors are identical to those used in the ubiquitous small uncrewed aerial vehicle (UAV) market save for additional epoxy waterproofing. Submersible electric thrusters

have improved in price and availability in recent years as they are increasingly used for hobbyist applications like electric paddleboards and kayaks (Mann et al., 2023) in addition to traditional applications in uncrewed underwater vehicles (UUVs) (Christ and Wernli Sr., 2014).

The thruster array is positioned at the end of the test section to allow any flow structures generated by the thrusters to dissipate along the length of the return section. At either end of the test section, the flow must execute a 180° turn: first from the thruster array into the return section and then from the return section back into the test section inlet. Such sharp flow turning is generally avoided to minimize flow separation, which can be a source of unsteadiness and persistent non-uniformity in the flow (Barlow, Rae, and Pope, 1999). At the first turn, the favorable pressure gradient from the thruster array acts to reduce the potential for separation; the turn into the test section inlet presents a greater challenge. Turning vanes were not employed to limit upfront engineering costs and simplify construction. Instead, an iterative procedure was used to design the flow management system (FMS) at the test section inlet to produce the desired uniform low-turbulence flow. Details of the implementation of this design are provided in Section 1.2 with flow characterization techniques and results in Sections 1.3 and 2.1, followed by a discussion in Section 2.2.

1.2 Technical Implementation

The FLOWTUB tunnel was constructed within a 0.89x0.89x2.11m aquarium tank (Figure 1.2). Sizing the test section cross-sectional area to roughly equal the return path area, this outer tank can fit a 0.61x0.61x1.37m test section, comparable to commercial water tunnels like the ELD 505 (Figure 1.1). Thus about 30% of the tank volume is occupied by the test section. This particular test section size was selected to be large enough to mount a gantry above the tunnel for dual use as a tow tank, and to enable varied experiments in biological fluids and vortex dynamics. In addition to the four glass sides and open top, four windows on the tank floor provide optical access. The function and construction of each element of the tunnel are discussed below.

Test Section

The two sides and bottom of the test section are flat sheets of 9.5mm thick clear acrylic plastic. An external frame composed of 316 stainless steel strut channel holds these panels in place. Alignment features and draw latches at each end of the test section allow for removable connection to the FMS and thruster array.

A 50% open 304 stainless steel perforated plate and 5cm thick 6.4mm cell honeycomb separate the test section from the thruster array. These elements enforce a pressure drop to isolate the flow in the test section from any downstream pressure irregularities arising from the thrusters. At the

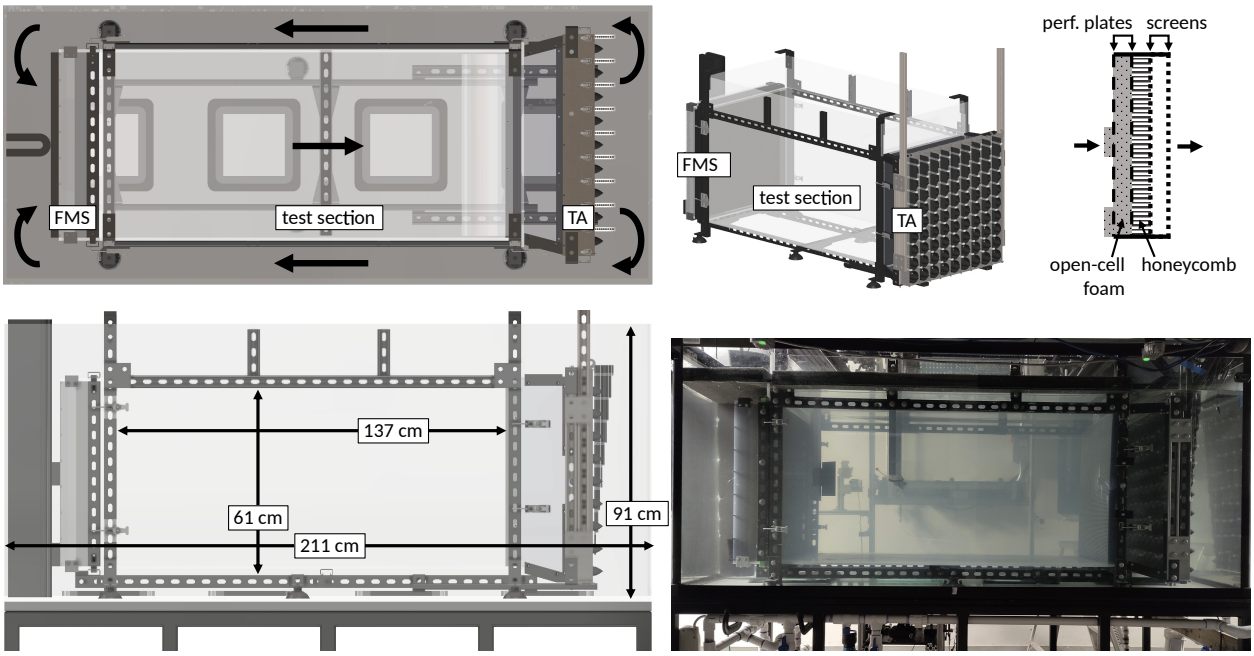

Figure 1.2 Computer-aided design (CAD) images of the FLOWTUB tunnel design including top, side and angled views (arranged counterclockwise), photograph of the tunnel (bottom right), and detail of the FMS construction (top right). In each view, the FMS and vertical baffle can be seen on the left side, test section in the center, and thruster array (TA) on the right. The angled view does not include the outer tank. Flow direction is indicated by black arrows in the top view.

opposite end of the test section, the FMS section aims to eliminate non-uniformity and temporal variation of the flow entering the test section.

Flow Management System (FMS)

To enter the test section, fluid from the return path outside the test section must execute a 180 degree turn. Rather than trying to avoid flow separation with bespoke turning vanes and a larger turn radius, this design relies on uniform blockage by a series of elements at the test section inlet. Because drag scales with the square of velocity, faster fluid experiences proportionally greater resistance due to a uniform blockage than does a slower fluid, which improves flow uniformity (Barlow, Rae, and Pope, 1999).

Four kinds of flow management devices were employed: perforated plates, honeycomb, screens, and reticulated (open-cell) polyester foam. All of these elements present approximately uniform blockage to the flow, with perforated plates being the most aggressive. The primary purpose of the honeycomb is to reduce swirl and spanwise flow. Screens serve to break up turbulence to small length scales on the order of the screen openings and wires (Barlow, Rae, and Pope, 1999). Less

prevalent in the literature is reticulated foam (Sabatino and Maharjan, 2015), which was used here both to break up flow structures to the size of the open cells and to encourage spanwise momentum exchange.

These elements were combined in several configurations in an iterative process to minimize deviations from a uniform velocity profile as measured by digital particle image velocimetry (DPIV, Section 1.3). The primary flow management system, represented schematically in the top right of Figure 1.2, is composed of four 9.5mm thick clear acrylic sides forming an open duct in which can be placed any combination of conditioning elements. After experimental iterations, the final configuration consists of a 50% open 304 stainless steel perforated plate followed by two layers of 2.5cm thick reticulated foam, one 12 pores per cm (ppc) and one 16 ppc. Next the water passes through a 60% open perforated plate followed by a 5cm long, 6.4mm cell diameter honeycomb and a stainless steel screen. Each of these components was stacked without gaps, occupying a streamwise length of just over 10cm. After a gap of about 5cm, the flow passes through a final stainless steel screen at the exit of the FMS into the test section.

Outside the FMS, a vertical baffle serves to redirect the flow into the inlet and inhibit spanwise flow. This baffle spans from the center of the FMS inlet to the tank wall and from the tank floor up out of the water. It is composed of a single 2.5x30x91cm piece of 8 ppc reticulated foam folded in half around a 2cm diameter stainless steel rod. In addition, two 2.5x10cm strips of 8 ppc reticulated foam were placed horizontally across the FMS inlet at the bottom and center to reduce the flow velocity within the test section at those locations.

Thruster Array

Water is propelled through the tunnel by a 9 by 9 array of Diamond Dynamics TD1.2 thrusters. Each thruster consists of a brushless electric motor with an anodized aluminum housing and epoxy-coated windings attached to a 58mm diameter propeller and mounted inside of a plastic duct with outer diameter of 73mm. The thrusters are capable of operating in forward or reverse depending on the pulse-width of a control signal sent to its electric speed controller (ESC).

The array is grouped both mechanically and electrically into 9 columns of 9 thrusters each. To minimize the total angular momentum of the array (and of the resulting flow), the rotation direction of the thrusters is alternated in a checkerboard pattern. Each row receives 12V power from a 1200 W server power supply (HP HSTNS-PL30) and rpm commands from a PCA9685 servo control board. Incidentally, a very similar power and control architecture was used in a recently published work using a grid of computer fans for a wind tunnel (Li et al., 2023). In the current implementation, each

power supply is supplied with 120VAC and is capable of outputting up to 900 W of power. A single Arduino Uno runs a custom script to receive control inputs from the tunnel operator and distribute these commands to the PCA9685 boards over I2C. During experiments, the rpm commands are sent via serial to the Arduino with a Python script. Hardware control is also available through a potentiometer knob and a switch. Each thruster has a unique address and it is possible to send each thruster a different rpm command. In the interest of generating low-turbulence uniform flows, only uniform rpm commands were sent to all thrusters for all the results shown in this paper, excepting the shear layer demonstration.

Each column of 9 thrusters is mounted on a 3mm thick 316 stainless steel plate. Each plate was cut from sheet stock on a waterjet to have a foot at the bottom edge and a groove to accept a latch at the top edge. To receive and support these column plates, a frame was constructed of 316 stainless steel 3mm sheet and strut channel with matching slots at the bottom and top such that each column plate can be inserted into the frame and latched in place. Each thruster power cable is routed through a series of lasercut acrylic clips along the leeward edge of the column plate up out of the tunnel where it connects to the power and control electronics through screw terminals on a DIN rail. This design makes it possible to service and replace any single thruster without impacting its neighbors.

Two vertical strut channel bars connect the outer frame of the array to the tunnel superstructure to support the thrust load during tunnel operation. The cross-sectional area inside the thruster array is larger than that of the test section, 70.8 cm wide by 67.5 cm tall. An 18cm long truncated pyramid diffuser composed of flat trapezoidal 9.5mm thick acrylic panels adapts the test section area to the larger thruster array.

Free Surface Management

At each station of the tunnel flow loop, the water level changes during operation as a function of the flow speed. The pressure changes across the FMS and thruster array are visible as changes in the free surface height across that element. These surface height gradients have the potential to cause water to cascade over tunnel elements, entraining air bubbles down into the water which can obfuscate measurements. The most effective solution to these issues of air ingestion from the free surface is to float sheets of closed-cell polyethylene (PE) foam on the water to quiet free surface instabilities. As much of the water surface as is practical is covered with sheets of PE foam during testing. The buoyant foam is able to rise and fall with changes in surface height as the tunnel speed is changed. This has the added benefit of adding damping to gravity waves, which reduces slosh in response to flow acceleration.

Maintenance Systems

A persistent challenge during the development of the tunnel was limiting the growth of algae. Chlorinating the water (similar to a swimming pool) was effective, but increases oxidation of the tunnel structure, thruster motors, and experimental models. Constant sediment filtration was also effective for limiting algae growth, but has the undesired effect of removing PIV seed particles. A 12 gpm 55W ultraviolet (UV) filter from Bluonics was found to be most effective at removing algae growth without impacting PIV seeding or causing corrosion.

The filtration system intake is a 3 ft length of PVC pipe capped with a vacuum brush and wire mesh filter that connects to the rigid PVC system outside the tank via a check valve and a 10 ft length of flexible vacuum hose. Thus the intake can easily be used to vacuum all areas of the tank and can be removed before testing. Piping from the intake leads to two electrical pumps in parallel. One pump (Lanchez 1/2 hp 960 gph shallow well jet pump) is used only to prime the system for operation of the second pump (1500 gph Sicce Multi 5800 aquarium pump) which is capable of continuous operation and happens to be significantly quieter. Experiments in the tunnel are conducted with both pumps switched off. The pumps drive water through a series of filters (including the UV, 100 micron, 5 micron and carbon filters), each of which can be bypassed as desired with a network of ball valves. The UV filter is connected to the PVC system through two 16 in copper water heater pipes to prevent stray UV light from degrading the PVC plastic in the rest of the system. Filtered water reenters the tank through an outlet pipe on the tank wall next to the the thruster array. Near the outlet, a hose connects to a laboratory sink, which is the source of the deionized water used to fill the tank as well as the drain.

1.3 Experimental Techniques

To validate the tunnel flow quality, measurements were made using planar DPIV and a hot-film constant temperature anemometer (CTA). Dye visualizations were also conducted as a qualitative demonstration of tunnel capabilities.

Digital particle image velocimetry (DPIV)

Flow-field measurements were acquired with DPIV in a streamwise plane centered spanwise within the test section. Raw images captured with an IDT XStream Mini-3520 camera were cropped to an area of interest 25.6 cm in the streamwise direction and 59.3cm tall, with the upstream edge about 40.6 cm from the test section inlet and the lower edge positioned 2cm from the test section floor. DPIV analysis was conducted in PIVview from PIVTEC using a multi-pass FFT correlation algorithm. Post-processing, including conversion to physical units and plotting, was

executed by a series of custom Matlab scripts. Vertical velocity profiles were produced by averaging this data in the streamwise direction and in time. Additional averaging in the vertical direction produced the mean velocity values used for thruster array calibration and calibration of hot-wire measurements. The camera frame rate was selected between 30 fps and 200 fps to keep particle displacements close to 5 px/frame at each rpm set-point. Two hundred frames were recorded for each experiment, which corresponds to total convective particle displacements of about the length of the viewing window. The water was seeded with hollow silver-coated glass spheres (Potters Industries AGSL150-30TRD). The laser was a continuous 445nm 10W diode laser originally manufactured for laser engraving.

Hot-film CTA

Turbulence intensity measurements were made using a TSI IFA-300 CTA with a 1210-20W hot-film probe. For single-point measurements of the turbulence intensity variation with velocity (Figure 2.5), the hot-film sensor was positioned 56cm from the test section inlet, 40cm from the test section floor, and 33cm from the left wall of the test section. At each tunnel speed, the CTA voltage was sampled at 1,000 Hz for 30 seconds using a National Instruments PCIe-6320 data acquisition card. Turbulence intensity was estimated from the root-mean-square fluctuations of the hot-film voltage and voltage sensitivity as determined by a King's Law calibration, following procedures outlined by Bruun (1995) and Bruun (1996).

Drift of the CTA voltage can complicate CTA measurements in water, brought about by fouling of the probe with particles, corrosion, or changes in the water temperature (Bruun, 1996). These effects were most significant during measurements of the variation of turbulence intensity with freestream velocity, which involved running the tunnel at high power for an extended period of time. To minimize this effect for these measurements, data was collected in three consecutive sweeps from low to high velocity and each sweep was fitted with King's Law to determine the voltage sensitivity. Spatially and temporally averaged PIV data provided the velocity reference for this set of measurements. The standard deviation of the fitted sensitivities was then propagated to estimate a 95% uncertainty in the turbulence intensity.

A common issue with CTA measurements in water is bubble formation on the sensing element (Bruun, 1996). In cases where a bubble was observed on the wire (characterized by a sharp decrease in the bridge voltage), the corresponding data was rejected and recaptured if necessary. This was only observed on two occasions during testing.

Additional measurements of the spatial distribution of these velocity fluctuations were taken sep-

arately by manually adjusting the position of the hot-film sensing element through a 5x5 grid centered in the test-section at 48 cm downstream from the test section inlet (Figure 2.6). For these sweeps, data was again recorded at 1000Hz, but the length of the recording was adjusted to be the highest of either 30 seconds, or one convective time based on the freestream speed and the length of the test section. At the lowest freestream speed, that convective time is three minutes. For this set of measurements, a separate calibration was conducted using the LDV probe with its sensing volume positioned about 1 cm upstream of the hot film sensor.

Laser doppler velocimetry (LDV)

For the spatial uniformity measurements in Figure 2.2 and spatial distribution of velocity fluctuations in Figure 2.6, mean velocities were measured using a 1D-miniLDV-G5L-500 system from MSE. Laser Doppler Velocimetry (LDV) measures the signal from particles passing through a fringe pattern created by the interference of two coherent laser beams. The miniLDV system from MSE combines the laser, optics and detection hardware in a single unit which is aligned and calibrated by the manufacturer. The system has a nominal probe volume width of 150μm and length of 1.2mm with a standoff distance of 49.1 cm, but refraction of the light path into water multiplies this standoff distance by the refractive index ratio to a maximum of about 65.5 cm. Data acquisition and conversion to velocity measurements were carried out using the MSE 1D Acquistion Manager software.

An MSE miniLDV G5B with a nominal standoff distance of 28.5cm, volume width of 200μm, and volume length of 3mm was used to record the tunnel's acceleration response to startup and slowdown signals. Starting from a quiescent tank, the thrusters were sent a throttle signal which linearly increased from neutral throttle to a throttle corresponding to 100mm/s freestream over the course of 8.5s. The rate of the signal ramp up was chosen as a balance between speed and robustness of the serial communication to the Arduino which controls the thrusters. Starting from a freestream throttle setting of 100mm/s, a second series of signals were sent which linearly decreased back down to zero at the same rate. The miniLDV settings were selected to maximize its dynamic range to capture the slowest speeds possible as well as the full 100mm/s setting. The minimum speed the miniLDV could resolve with a signal to noise ratio above 2 was around 6mm/s. Three startup and three slowdown sequences were recorded at a point near the center of the test section, and each LDV recording was shifted such that t=0 corresponded to the time at which the velocity first crossed 50mm/s.

Fluorescent dye flow visualization

In addition to DPIV and CTA measurements, fluorescent dye (Bright Dyes FWT Red Powder) was used for qualitative flow visualization. The dye system was gravity-fed from a reservoir near the lab ceiling through flexible Tygon tubing. Dye flow was toggled on and off with ball valves and finely adjusted with a series of pinch valves.

A series of visualizations was recorded of the von Karman vortex street behind a 5.9 mm diameter circular cylinder. Acrylic endplates were used to hold the cylinder in place and to minimize end effects. To capture wakes at Reynolds numbers from 40 to 490, the tunnel velocity was varied between 0.8 cm/s and 8.7 cm/s.

Dye visualization was also conducted on a planar shear flow as a demonstration of the diverse capabilities afforded by the thruster array architecture. For this demonstration, the tunnel was run in a blowing configuration (reverse from the rest of the results in this thesis) and the rpm command to the top four rows of the thruster array was reduced by 8% relative to the bottom five rows, yielding a velocity twice as large on the bottom as on the top. A trapezoidal piece of poster foam board was positioned within the diffuser as a splitter plate to separate the two different velocity streams. Dye was injected through a wand made of a 12in length of 1.6mm outer diameter, 0.8mm inner diameter length of stainless tubing with its outlet pointed downstream within the honeycomb between the diffuser and test section. During tunnel development, the same wand was used as a qualitative tool to inform the iterative design of the FMS.

RESULTS AND DISCUSSION

2.1 Flow Quality

Uniformity

The vertical velocity profile in the tunnel was measured for a range of thruster array rpm for dozens of iterations of the FMS. Figure 2.1a shows the tunnel velocity profile without any FMS at the test section inlet. With no flow management, the measured profile was unsteady and exhibited large velocity gradients across the test section. Each of the measured rpm setpoints produced very different velocity profile shapes, with variations from the mean profile in excess of 40%. The inconsistency and large gradients in these measured profiles is likely driven by flow separation as the flow turns 180° from the return section into the test section. Such large gradients in the flow preclude this configuration from being useful for experiments, illustrating why water tunnels are not typically built in such a small space.

However, with the flow management elements described in Section 1.2, not only are the measured profiles consistent across different rpm setpoints, the velocity gradients and deviations from the mean are markedly reduced. The final velocity profile shown in Figure 2.1b indicates less than a ±4% deviation from the mean for the full velocity range outside of free surface and boundary layer effects. The 95% confidence interval associated with streamwise averaging the PIV field of view was smaller than ±2.6% for all locations in the lower 80% of the test section.

Additional flow uniformity measurements were taken with LDV at a cross section located 48cm downstream of the test section inlet (Figure 2.2). Similar to the vertical velocity profiles, the velocity at each location is within a few percent of the spatially averaged mean, although a somewhat large (roughly 6 to 8%) velocity deficit exists in the top corners near the free surface. This level of uniformity is acceptable for the purposes of this research facility, but could be improved by varying the thickness of the open cell foam in the FMS if desired. Additional LDV measurements taken in roughly 10 minute intervals over a 3.25 hour experiment indicated less than a 0.4% linear drift in mean velocity at 10.8 cm/s in the center of the test section.

Thruster array rpm calibration

A thruster array calibration curve with the final FMS is presented in Figure 2.3. The percent rpm is referenced to the maximum rpm level of a thruster. As expected, tunnel speed has a linear

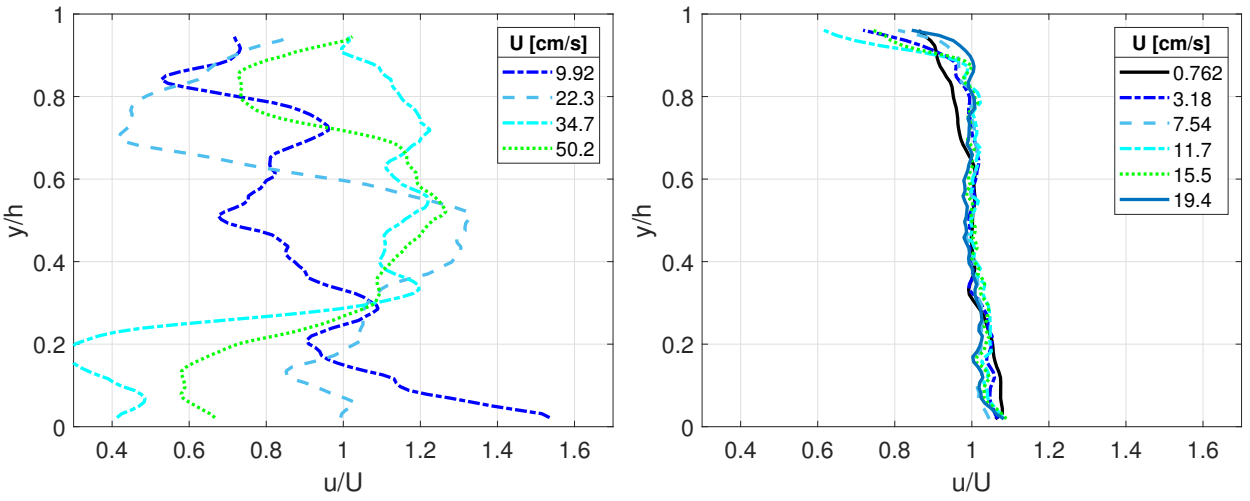

(a) No FMS (b) Final FMS

Figure 2.1 Comparison of streamwise velocity profile across vertical extent of test section with and without the FMS. Velocity is normalized by mean velocity at given thruster rpm, vertical position is normalized by the test section height (61 cm). Measured 40.6 cm downstream from test section inlet on the center plane of the test section. Each of the curves on the left plot had the same throttle setting as the corresponding curve on the right.

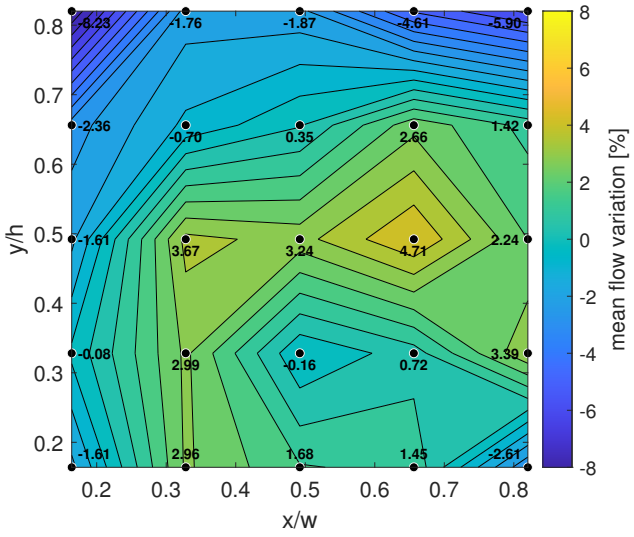

Figure 2.2 Variation of mean velocity at each sampled location as percentage of the spatially averaged mean of 11.0 cm/s. Cross section measured 48 cm downstream from the test section inlet with vertical (y) and horizontal (x) position normalized by the test section height (h) and width (w)

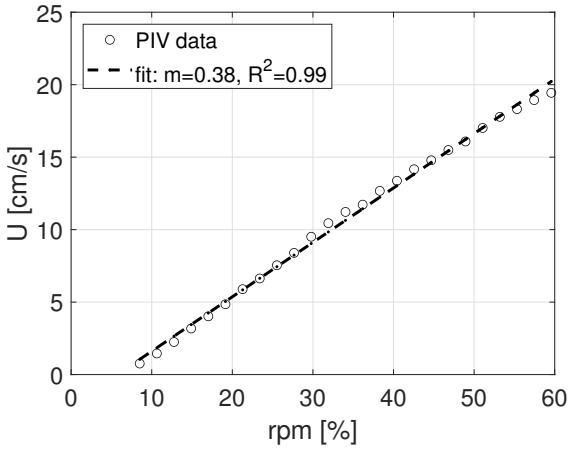

Figure 2.3 Thruster array velocity calibration

relationship with thruster rpm. In exchange for flow uniformity, the FMS reduces the average speed of the tunnel for a given percent rpm setpoint by about 70%. At a 46.8% rpm, for example, the tunnel with no FMS generates an average freestream speed of 50cm/s, while the uniform flow generated with the FMS has a speed of 15cm/s. The operational tunnel speeds with the FMS range from as low as 0.76 cm/s to about 20 cm/s.

Startup and Stop Response

The tunnel velocity response to a smooth start and smooth stop throttle signal is provided in Figure 2.4. In both Figure 2.4a and 2.4b, three trials have been aligned so t=0 corresponds to the moment when the LDV velocity signal crosses 50mm/s. After the first initial rapid rise, the tunnel continues to speed up more slowly to its setpoint. The first phase is related to the rate at which the thrusters are spinning up, and the second slower rise is the water in the tank lagging behind after the thrusters have reached a constant setpoint. With this signal, the tunnel is capable of accelerating to 99% of its set point value (100mm/s) within about 10s. Deceleration takes a bit longer: roughly 20s from the start of the deceleration until the velocity drops below the measurement range of the LDV. Agreement between the three trials is quite good, indicating a high level of repeatability.

Turbulence intensity

Turbulence intensity estimates are presented at a single location for the velocity range of the tunnel in Figure 2.5. Because a low speed facility such as this is dominated by lower frequencies, a 16 Hz low-pass filter was applied to the data to minimize the influence of building vibrations on measurement. The measured turbulence intensity is below about 0.5% for the operating range

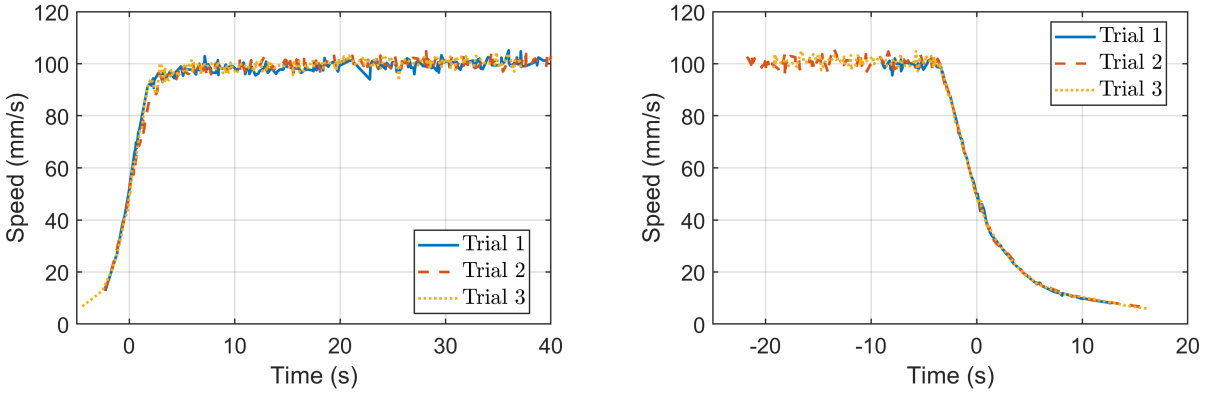

(a) Startup response

(b) Stop response

Figure 2.4 Tunnel response to acceleration signals, measured with MSE miniLDV

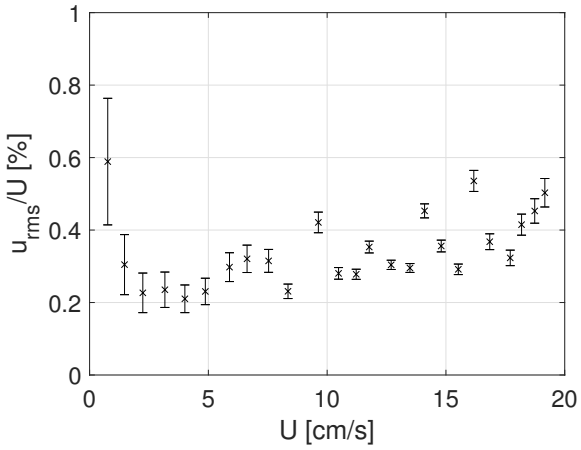

Figure 2.5 Turbulence intensity from hot-film CTA measurements taken at 56cm downstream from the test section inlet, 40cm from the test section floor, and 33cm from the left wall of the test section. Error bars represent uncertainty due to voltage drift during measurement

of the tunnel. Even without the lowpass filter (including building vibrations, not pictured), the measured turbulence intensity remains below 2% for all speeds above 5 cm/s. Further discussion of the influence of building vibration on CTA measurements is offered in appendix A.

A spatial sweep with the hot-film probe also measured the turbulence intensity in a square grid cross section located 48cm downstream from the test section inlet (Figure 2.6). For this set of measurements, the structure supporting the probe was isolated from the building vibration as much as possible, and no filtering was applied.

In this case, the measured velocity fluctuations agree well with the results presented in Figure

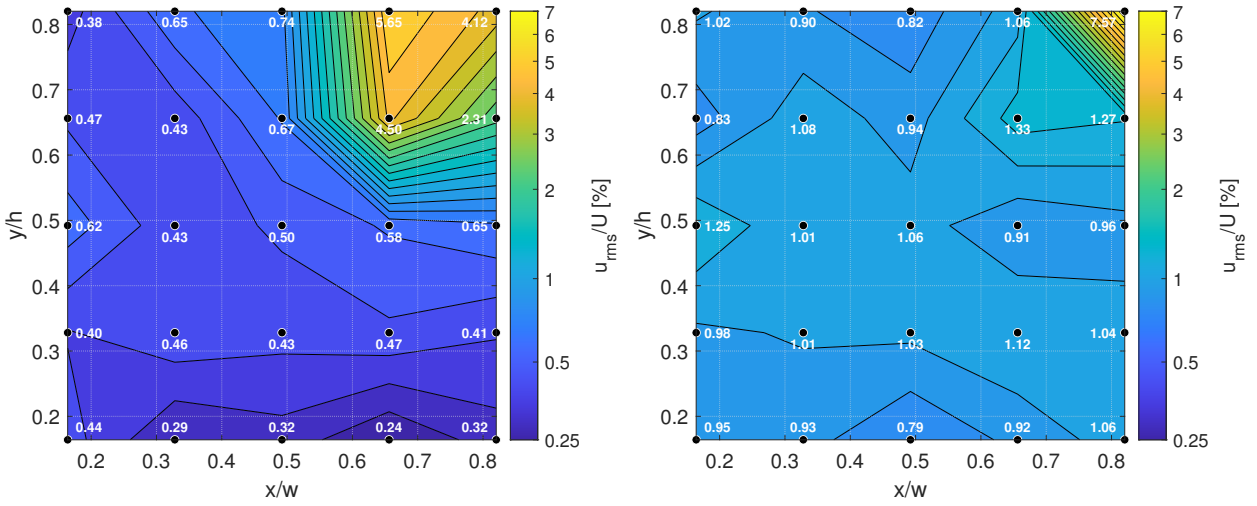

(a) U = 0.76 cm/s

(b) U = 11.0 cm/s

Figure 2.6 Spatial distribution of velocity fluctuations. Cross section measured 48 cm downstream from the test section inlet with vertical (y) and horizontal (x) position normalized by the test section height (h) and width (w)

2.5 despite the lack of filtering and the fact that the power spectrum still contains evidence of contamination from building vibration. At all tested speeds, the measured turbulence intensity remains at or below 1% across the full cross section of the tunnel, with the exception of the top right corner near the free surface. At that location, a small leak in the test section wall was discovered which allowed water from the return section to bypass the FMS and enter the test section directly. Due to the low pressure difference between the return section and test section such leaks can easily be stopped with a silicone sealant.

Dye visualization demonstrations

Visualizations of the von Karman vortex street behind a circular cylinder at a variety of Reynolds numbers (Figure 2.7) give a qualitative indication of the low freestream turbulence of the tunnel, and demonstrate the sort of experiments that are possible with this facility. The cylinder wakes appear as expected: at the lowest Reynolds number of 40 no shedding is observed, shedding begins somewhere before Reynolds number of 80, and the wake has transitioned to turbulent by Reynolds number of 490 (Batchelor, 2000).

An additional demonstration of the tunnel capabilities when operated in a blowing configuration is shown in Figure 2.8. Injected dye traces the classic Kelvin-Helmholtz instability in a shear layer created by commanding an 8% slower rpm to the lower 5 rows of thrusters with a splitter plate placed within the diffuser. Mean velocity above and below the shear layer was measured with LDV

Figure 2.7 Dye visualization of the wake behind a 5.9 mm circular cylinder at Reynolds numbers of 40, 58, 80, 250, and 480 (top to bottom)

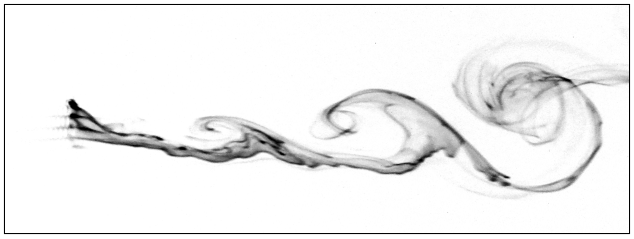

Figure 2.8 Dye visualization of a shear layer created by running the thrusters in reverse with a lower rpm command sent to the top four rows. Mean velocity above the shear layer is 4.7mm/s and below is 9.6mm/s

at 0.47cm/s and 0.96cm/s, respectively.

2.2 Discussion

Flow Quality

The above results demonstrate that, despite being far more compact, this water tunnel is able to achieve flow quality comparable to or better than most water tunnels used for academic research (Pinapatruni et al., 2024; Moreto and Liu, 2020; Sargison et al., 2009; Da Silva Ássi et al., 2005; R. Gordon and Imbabi, 1998; Persen and Saetran, 1983; Charters and Miles Anderson, 1980). At present, the FLOWTUB tunnel's maximum speed is about 20 cm/s. At this top speed, the thrusters are operated at only 60% rpm. The current speed limit is imposed by the level of the water in the tunnel and the height of the tank walls necessary to avoid flooding the laboratory. Higher speeds could be achieved if necessary by raising the tank sides, lowering the water level, or reducing the pressure drop throughout the flow circuit. However, the goal of this facility is to enable low-speed dye flow and DPIV investigations for which the lower speeds are an asset rather than a limitation.

The cylinder dye visualizations provide a potent demonstration of the utility of a facility that is able to operate at extremely low speeds, which enable low Reynolds numbers at which the quality of flow visualization is improved due to reduced turbulent diffusion. At the same time, this particular test occupied only a very small portion of the test section and the lower end of its speed range. A larger 6cm diameter cylinder with a blockage ratio of 10% operated at the top tested speed of 20 cm/s would be able to achieve Reynolds numbers above 10,000. It is also worth noting that it is uncommon for even low speed water tunnels of this size to achieve acceptable flow quality at such low speeds. The ELD 505 for example has a nominal minimum speed of around 3 cm/s, whereas the FLOWTUB tunnel achieves acceptable flow quality at less than 0.8 cm/s.

Power Requirement

The low speeds of the tunnel are the direct result of the high pressure losses through the tunnel circuit caused by the tight corners, aggressive flow conditioning, and omission of the contraction section. This is evident in Figure 2.3, where the speed at a given rpm setpoint was reduced 70% by the addition of the FMS. This represents a test section power loss of over 97%, and a reduction of 91% of the test section dynamic pressure. At the current scale however, the total amount of power that the FLOWTUB requires (2.3 kW) at the maximum tested velocity (20 cm/s) is comparable to the power required by a kitchen dishwasher, or four NVIDIA RTX-5090 GPUs. If all 2.3 kW of that energy went to heating the tank water, it would take about one hour to raise the temperature by 1°C. In reality, the water temperature has yet to change more than 0.1°C in the course of an experimental campaign because there is no operational need to run the tunnel full speed for extended periods of

time. If long run times at full speed become desirable, a heat exchanger could likely be added in the return path without adversely effecting flow quality in the test section.

Compared to a common traditional tunnel, such as the ELD 505 (which has the same test section cross-sectional area), the current tunnel consumes about 10x more power for a given flow speed. It should be noted that the power associated with driving a fluid of a given density through a given cross section increases with the cube of the flow velocity, so this factor will become more important at higher flow speeds. The power tradeoff is reflected in the reported maximum speeds of the tunnels. Extrapolating based on the maximum rpm of the thrusters, the FLOWTUB could reach about perhaps 33cm/s (about 1/3 of the 1m/s top speed of the ELD 505) if the tank walls were extended higher. If even higher flow speeds are desirable, there is ample opportunity to optimize the FMS and corners to minimize pressure drop. In the development of the FMS for example, no attempt was ever made to remove conditioning elements. Adding turning vanes at the corners would likely be effective at decreasing power and increasing speeds as well. In addition, it is perhaps worth noting that the FLOWTUB design results in a much smaller total volume of fluid for a given test section volume, which should reduce the power associated with flow acceleration relative to a larger traditional tunnel.

Tunnel Size

Often a bigger contributor to the usefulness of a water tunnel than the power required to run it is the laboratory space it requires (Breuer et al., 2022; Zahari and Dol, 2015; R. Gordon and Imbabi, 1998). Figure 1.1 presents a to-scale visual comparison of the size of the FLOWTUB tunnel to that of the ELD 505 tunnel. The FLOWTUB occupies less than 8% of the total bounding rectangular footprint area and 3% of the total bounding box volume of the ELD 505 tunnel, despite the two tunnels having the same test section cross sectional area. The FLOWTUB design admits a test section cross sectional area of about 20% of the total available footprint area. Traditional designs like the ELD 505 have test section cross sectional areas about 1.5% of total footprint area. Thus for a given footprint, the FLOWTUB design has a test section area about 13x larger than a traditional design. A larger test section will admit larger test models, which can be an advantage when manufacturing precision is a constraint.

Reynolds Number

We can analyze the achievable Reynolds numbers for a FLOWTUB design versus a traditional tunnel like the ELD 505 for a given amount of laboratory space. While the power requirement of a tunnel scales with the cube of velocity, the Reynolds number scales linearly with velocity and with

length.

In a hypothetical scenario where a given area is available for the construction of a water tunnel and the goal is to achieve the highest possible Reynolds number, the FLOWTUB design admits a 3.6x longer/wider model than a traditional tunnel. This 13x larger cross-sectional area will require a commensurate increase in power to achieve a given flow speed, and perhaps another 10x for power on top of that based on the relative efficiency of the FLOWTUB tunnel. Thus a FLOWTUB tunnel with the same footprint and flow speed would take 130x more power to run than a traditional tunnel, but would achieve a 3.6x larger Reynolds number given its larger test section size.

Given the high power requirement, it likely makes sense to operate the FLOWTUB tunnel at a reduced speed relative to a traditional tunnel. If the FLOWTUB facility was supplied with 5 times the power, the resulting flow speed would be 1/3 as fast, but the Reynolds number would be about 20% higher than for a traditional tunnel. This speed ratio is similar to what the FLOWTUB tunnel presented here could achieve if the thrusters were run at maximum rpm. An additional advantage of having a larger test section size at a given Reynolds number is that the dynamic pressure is proportionally lower, which minimizes structural challenges for models in the tunnel. Alternatively, for the same power input, the FLOWTUB would run at 1/5 the speed of the traditional tunnel, but with 72% of the Reynolds number.

In general, the FLOWTUB design trades power efficiency for simplicity and a larger test section. At the scale described here, this power difference is negligible, but as the tunnel footprint and Reynolds number requirements grow the power requirements could begin to drive the design.

Acceleration ability

The startup and stopping LDV plots presented in Figure 2.4 give some indication of the capabilities of this type of tunnel for producing accelerating flows, like gusts or startup flows. The throttle signals used to produce these plots were open loop and not optimized in any way. Faster response times without overshoot are likely possible by providing closed-loop non-linear throttle signals. In the case of the deceleration test, the thrusters can be run in reverse to actively decelerate, instead of the passive deceleration dictated only by the resistance in the circuit.

Relative to a single large pump, each thruster has a much smaller rotational inertia and so can be spun up and down more quickly. The FLOWTUB design also has significantly less fluid volume than a similarly sized traditional tunnel (about 15% the amount of water used by the EDL 505), and does not contract the flow into small diameter piping anywhere in the circuit. This means that the FLOWTUB is able to accelerate more quickly than a traditional tunnel. Such a quality may allow

testing of the sort only previously available to tow-tank facilities. One can even imagine running the tunnel in closed loop along with a gantry system to produce a arbitrarily long startup sequences by matching the gantry and flow speeds. Incidentally, the current FLOWTUB does have a gantry system installed above, and the high damping of the FLOWTUB tunnel significantly reduces the amount of time it takes for the tank to reach a quiescent state between startup tests using the gantry. Fast response times are also helpful for static measurements, by making nulling less onerous.

Multi-sourced opportunities

In addition to uniform steady flows, the FLOWTUB propulsive configuration is particularly well suited to investigate phenomenon characterized by complex spatially and temporally varying flows. Each of the 81 thrusters that drive the flow are uniquely addressed and controlled by software such that inputs of arbitrary complexity can be realized. Each thruster is also capable of operating in forward or reverse, so the tunnel can easily be operated in a blowing configuration if it is desirable to specify spatially and temporally non-uniform flows. Similar capabilities have begun to be explored with air as the working fluid (Nishi, Miyagi, and Higuchi, 1993; A. Nishi et al., 1997; E. Johnson and Jacob, 2009; Jia-Ying et al., 2015; Noca et al., 2019; L'Ecuyer, 2021; Dougherty, 2022; Olejnik et al., 2022) and have found success in applications with significant space constraints (Veismann et al., 2021). There is naturally a large opportunity for similar experiments in water.

A particularly interesting avenue of research may be the generation of turbulence on demand by varying the inputs to the thrusters in space and time (A. Nishi et al., 1997; L'Ecuyer, 2021; Dougherty, 2022). Somewhat similar setups using arrays of synthetic jets are used to generate isotropic turbulence in in the absence of mean flows (Variano, Bodenschatz, and Cowen, 2004; McCutchan and B. A. Johnson, 2023). There may be opportunities with FLOWTUB facilities to investigate isotropic turbulence with non-zero mean flows without additional components like active grids.

Manufacturing differences

An additional difference between FLOWTUB and traditional tunnels is the complexity of its constituent components. Each element of the FLOWTUB was purchased as raw material and assembled by a single graduate student. It is readily apparent in Figure 1.2 that the tunnel consists of easily manufactured right angles and straight lines. The only tools required for the creation of the water tunnel structure are a drill, wrenches, hacksaw, 3D printer, waterjet, and lasercutter—all of which are inexpensive or readily available at most research institutions. Traditional contraction, settling, turning, and diffuser sections are often geometrically complex and bulky components that

must be manufactured offsite, shipped to location, maneuvered into position, and fastened with water-tight seals. The FLOWTUB design omits such elements entirely, resulting in a large cost savings for tunnel manufacturing and installation.

Because the test section is contained within the outer tank, it is not essential that it be completely water-tight. Gaps are to be minimized, of course, but removing the requirement to make every seal of the water tunnel completely sealed greatly simplified the design and allows the separate elements to be truly modular. This was extremely useful during iterations of the FMS, in which the entire unit could be removed from the tunnel, modified, and reinserted in the span of minutes rather than hours, all without draining the water. Traditional tunnels often have the honeycombs and screens exposed at the free surface for this reason, but these elements are often so large that they become difficult to move and replace for this scale of test section.

The test section itself, by virtue of having water on both sides of each surface, was able to be composed of inexpensive 1cm thick acrylic sheets rather than more expensive and heavy glass or thicker acrylic. The total dry weight of the test section is less than 50 lbs, such that lifting it into and out of the tank is a manageable operation without any specialized equipment beyond a handful of people and some rope. Acrylic plastic (polymethyl methacrylate, PMMA) expands as it absorbs water, with linear expansion as high as 0.5% (Rose et al., 1955). This was accounted for relatively easily in this design by over-sizing clearance for bolt holes to allow the material to expand as needed. This design requirement could be more challenging for traditional tunnels where the test section must be completely water-tight, which is one reason such tunnels often opt for glass over cheaper and lighter acrylic.

Cost and thruster longevity

The nominal lifespan of the hobby-grade thrusters used in this work is on the order of one year. Roughly half of the 81 thrusters ceased to function within about a year and a half of first installing them in the tank. During the PIV experiments described above, 10 thrusters (12.3%) had stopped working. After replacing the thruster array, no changes in tunnel flow quality were measured, though the flow speeds for a given thruster rpm increased roughly in proportion to the number of operational thrusters. Decreased friction in the new set of thrusters meant that they were also able to spin at lower rpm, keeping the minimum flow speed unchanged. Because the top speed is limited by the water level in the tank rather than thruster power, the overall operating range of the tunnel was essentially unchanged as well. This demonstrates that the FLOWTUB design is inherently robust to thruster failures. The cause of these failures appears to have been corrosion of the aluminum motor housing, which was accelerated by chlorinating the water to prevent algae growth. Avoiding

the use of chlorine has solved the motor housing corrosion problem, as no motors have failed in over a year since replacing the array.

The Diamond Dynamics TD1.2 thruster motors used for this tunnel had a unit cost of $41.50 including the cable and electronic speed controller. This price is low enough that replacing all 81 thrusters would cost less than $3,500. The cost of the entire FLOWTUB tunnel (not including labor) was about $30,000, with about one third of that cost coming from the outer aquarium tank. A traditional water tunnel with a similarly sized test section would cost over $200,000, not including the cost of lab space.

Maintenance and Operations

The simplicity of the tunnel geometry has obvious benefits for maintenance. The glass tank and open top affords visual and physical access to everywhere in the tunnel, which is invaluable for cleaning, maintenance, diagnosing flow quality concerns, and for optical flow measurements. A common issue for traditional tunnels is that particulates (including seed particles for DPIV) tend to settle out or stick to surfaces in the slower flow regions upstream of the contraction. The FLOWTUB tunnel has a more uniform cross-sectional area, which largely eliminates this issue.

For experiments with a visual/optical component, the tank-within-a-tank architecture does present some possible complications. The optical path from outside the tank to inside the test section includes a glass wall, return flow water, the acrylic test section, and the test section water. However, because the acrylic wall is surrounded by water on both sides, refraction is not of any more concern than a traditional single-walled water tunnel test section. Looking through the return flow has also not been an issue for DPIV studies because only the field of view is illuminated by the laser and is in the camera's focal plane.

In a recirculating flow facility, injecting dye for flow visualization can create a situation where contrast is reduced as dye concentration in the bulk flow rises. This limitation is commonly dealt with by introducing chlorine bleach to break down dye in the water, but as mentioned above, chlorination has negative side effects, namely corrosion of the thrusters. Instead, the tunnel is typically drained and refilled when necessary.

2.3 Conclusion

A novel water tunnel design has been developed which generates comparable flow quality and test section size to traditional tunnels at a small fraction of the total size and cost. Flow uniformity is within ±4% of the mean and the turbulence intensity is less than about 0.5% for all speeds. The test section has about 13 times larger cross-sectional area than would be afforded a more traditional

water tunnel in the same footprint area. These results are realized by driving the flow with an array of small electric thrusters through a test section that is centered within a large aquarium tank. An aggressive flow management system without any contraction, settling, or turning sections ensures comparable flow quality to traditional tunnels at the expense of a lower power efficiency. The thruster array architecture also affords inherent versatility to generate spatially and temporally varying flows and benefits for operations, maintenance, and overall cost. The FLOWTUB tunnel is actively being used for fluid mechanical studies at GALCIT and presents multifarious opportunities for continuing research.

Part II

Evolution of Delta Wing Surface Contour from Flat Plates to Boxfish at Low Reynolds Numbers

INTRODUCTION

A wing with swept leading edge can generate a vortex which acts to reduce the pressure on its leeward surface, augmenting the wing's lift. Delta wings, sharing their shape with the Greek letter, are a particularly well-studied class of such wings. Interestingly, similar vortices are generated from the keels of a variety of bony fish known as boxfish. Boxfish have many obvious morphological differences from a flat, swept wing, perhaps chief among them being their height. The tall body of the fish constrains the space available for a vortex to form relative to a flat wing with similar planform.

The confinement of this vortex and the resulting changes to the flow-field over the wing and wing performance at low Reynolds numbers will be addressed in the remaining chapters of this thesis. Such questions have relevance beyond our understanding of boxfish biology to a wide variety of aerospace vehicles for which vortex lift and large internal payload volumes are desirable, such as blended-wing-body airplanes, hypersonic reentry vehicles, and UCAVs.

3.1 Delta Wing Background

Delta wings are classified by their triangular planform shape, defined primarily by the sweepback angle of the leading edge (Λ, Figure 3.1a). It is useful to refer to a body-fixed reference frame with the x-axis aligned to the wing chord, y-axis pointing starboard, and z-axis up from the wing surface. The body x-axis aligns with the freestream flow direction at an angle-of-attack (AOA) of zero.

In addition to the lift (L), drag (D), it can be helpful to consider the force components normal (N), and tangential (T) to the wing (Figure 3.1b). The pitching moment is often reported about the quarter point of the mean aerodynamic chord (MAC), which is defined as $MAC = \int_{-b/2}^{b/2} c(y)dy/S$, where $S = bc/2$ is the wing planform area, b is the wing span at the trailing edge, and c is the wing chord (Schlicting and Truckenbrodt, 1979). Positive moments pitch the wing up. Force results later in this thesis are reported as coefficients normalized by the wing planform area and dynamic

pressure ($q = 1/2\rho U_\infty$) as follows:

$$c_L = \frac{L}{qS} \quad \text{(Lift coefficient)}$$

$$c_D = \frac{D}{qS} \quad \text{(Drag coefficient)}$$

$$c_N = \frac{N}{qS} \quad \text{(Normal force coefficient)}$$

$$c_T = \frac{T}{qS} \quad \text{(Tangential force coefficient)}$$

$$c_M = \frac{M}{MACqS} \quad \text{(Pitching moment coefficient).}$$

Reynolds numbers are reported based on freestream speed and wing chord from apex to trailing edge.

Delta wing flow field

The flow field over flat delta wings has been well studied over the past nearly 100 years. The swept leading edges of delta wings create a pair of stable counter-rotating vortices emanating from the wing apex across a wide range of geometries and angles of attack (Earnshaw and Lawford, 1964). These vortices are referred to as leading edge vortices (LEVs), or primary vortices. In many cases, the LEVs induce an outboard flow along the wing surface under the LEVs, which separates due to ordinary boundary layer separation into another pair of secondary vortices with opposite sense. A cartoon of the general delta wing flow structure as viewed from behind is provided in Figure 3.2 after Deitrich Hummel (1981). Between the LEVs, flow along the wing surface can be attached and aligned to the x-axis direction.

On an ideal delta wing of infinite chord in an inviscid fluid, there is no length scale to differentiate the flow field at different spanwise cross-sections, so the flow-field is necessarily self-similar. This permits a class of potential flow solutions using the assumption that the flow is conical (Brown and Michael, 1954; Mangler and J. H. B. Smith, 1959; J H B Smith, 1971; Pullin, 1975; Nutter, 1981). In reality, observed delta wings LEVs do tend to follow straight-line trajectories near the apex, but must eventually bend to match the freestream flow direction near the trailing edge.

The leading edge vortices themselves are formed when a shear layer formed by separation at the leading edge rolls up into a region of concentrated vorticity with an axial velocity typically higher than the freestream speed. The vorticity generated at the leading edge is then convected along the vortex axis, maintaining the stability of the vortex over the wing. A similar leading edge vortex is

formed over wings of lower sweep at startup, but without axial convection to remove vorticity no stable LEV is observed (M. Lee and Ho, 1990).

As the angle of attack is increased, a phenomenon known as vortex breakdown occurs in which the LEV undergoes a sudden increase in diameter, often accompanied by a reversal of the axial flow direction (Lucca-Negro and O'Doherty, 2001). This process can be understood as being caused by the balance of vorticity determined by the flow geometry at the leading edge (W. H. Wentz Jr. and Kohlman, 1971). A Rossby number that describes the ratio of azimuthal to axial velocity in the vortex, or the helix angle, can be a useful parameter for predicting when bursting may occur (Delery, 1994; Spall, Gatski, and Grosch, 1987). Increasing the angle of attack also affects the position of the LEV over the wing surface, tending to move it inboard and away from the wing surface (Grellmann, 1964; J. H. B. Smith, 1968).

A useful model for understanding and predicting the normal force of delta wings was proposed by Polhamus (Polhamus, 1966). This model separates out the contribution of an attached flow over the wing and the non-linear incremental force contributed by the vortex suction. Experimental data matches this prediction well, and also shows wing stall occurring at some critical angle of attack related to the breakdown of the LEV and separation of the centerline flow (W. H. Wentz Jr. and Kohlman, 1971; Earnshaw and Lawford, 1964). Typically stall occurs much higher for delta wings than it does for higher aspect ratio wings, with peak lift reached around $AOA = 30$. Stall tends to be accompanied by an undesirable pitch-up which has been the focus of much research (Hirschel et al., 2021).

Effect of delta wing geometry

Similar to the angle of attack, the sweepback angle or aspect ratio of a delta wing affects the ratio of normal to tangential flow incident on the leading edge, changing the strength and position of the LEVs, the amount of vortex lift, and the angle of attack at which stall occurs (Polhamus, 1966; Earnshaw and Lawford, 1964; M. V. Ol and Gharib, 2003).

Slender delta wings (typically referring to wings having sweepback angles $\Gamma > 65°$) have higher vortex lift than non-slender wings with lower sweepback. As the sweepback angle is reduced, the LEV tends to move much closer to the wing surface, which can cause it to interact more strongly with the surface boundary layer (I. Gursul, R. Gordnier, and M. Visbal, 2005). This can increase the dependence of the flow field on Reynolds number (Taylor, Schnorbus, and Ismet Gursul, 2003). For 50° wings at Re$\approx 10^4$, the LEV has been observed to split into a dual-primary structure at low angles of attack (Raymond Gordnier and Miguel Visbal, 2003; I. Gursul, R. Gordnier, and

M. Visbal, 2005; Taylor, Schnorbus, and Ismet Gursul, 2003). The dual vortex structure reverts back to a single primary LEV as the AOA is increased and the LEV moves away from the surface. Lower sweep angles have also been observed to cause earlier vortex breakdown and stall (Earnshaw and Lawford, 1964).

The shape of the leading edge can also have a large effect on the delta wing flow field (Bartlett and Vidal, 1955; Kegelman and Roos, 1989). Generally, a blunter leading edge will produce less lift and less drag (Henderson, 1976; Luckring and Dietrich Hummel, 2013). A sharp leading edge has a fixed separation point to satisfy the Kutta condition, while separation off a rounded leading edge will depend on its radius, Reynolds number, and angle of attack (Hirschel et al., 2021; Verhaagen, 2011).

Generally, the effect of delta wing airfoil shape or leeward surface shape is understood to be small relative to the effects of leading edge and planform geometry (Hirschel et al., 2021). However, most studies concerned with the thickness of delta wings have focused on thicknesses less than 20% of the chord. Lift is substantially reduced and profile drag increased with increasing wing thickness (Sharifi Ghazijahani and Yavuz, 2019; Kirby and D L I Kirkpatrick, 1971).

A body of literature exists examining a mechanism intended to reduce lift-induced drag by angling the leeward surface forward nuder the LEVs such that a component of the suction force counteracts drag (G. Lee, 1959; Shaw, 1970; D. I. I. Kirkpatrick, 1965; Traub, 2000a). Much research has also looked into deviations from a planar planform via leading edge devices, gurney flaps, and conical or spanwise camber. A series of studies by Traub found that pure anhedral on thin wings can augment lift by moving the LEV closer to the wing surface (Traub, 2000b; Traub, 2000a).

Delta-wings with larger cross-sections have been found to produce significantly less normal force and higher drag for both rhombic (D. I. I. Kirkpatrick, 1965) and triangular (Grellmann, 1964) cross-sections. Despite having large thickness, these extreme variations on delta wing geometries still exhibited a flow field similar to classical flat deltas, albeit with vortex positions strongly influenced by cross-sectional shape. Increasing rhombic cross-section height at a given angle of attack sifts LEVs up and outboard up to a critical surface height when they begin to move back down and outboard (D. L. I. Kirkpatrick and Field, 1966). A similar study by Grellmann (1964) found that triangular cross-sections first move the LEV inboard, then outboard as surface height is increased for a given angle of attack. These studies were conducted at Reynolds numbers of around 10^6 and predated the development of experimental techniques such as particle image velocimetry (PIV) which allow for field measurements of quantities like velocity and vorticity. They were also limited to only cross-sections composed of straight lines for ease of manufacturing and to limit the

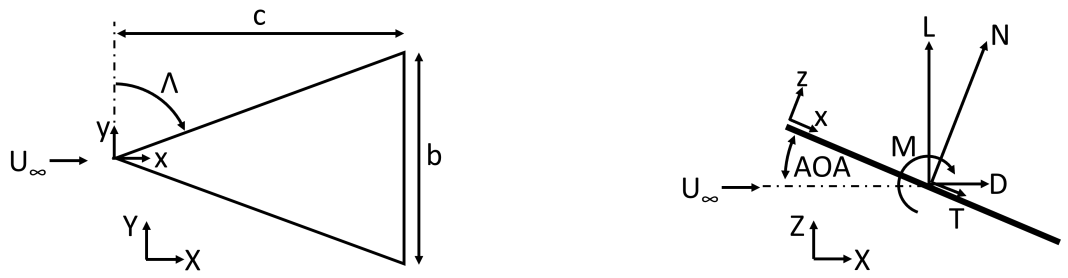

(a) (b)

Figure 3.1 Top (a) and side (b) views of flat delta wing geometry.

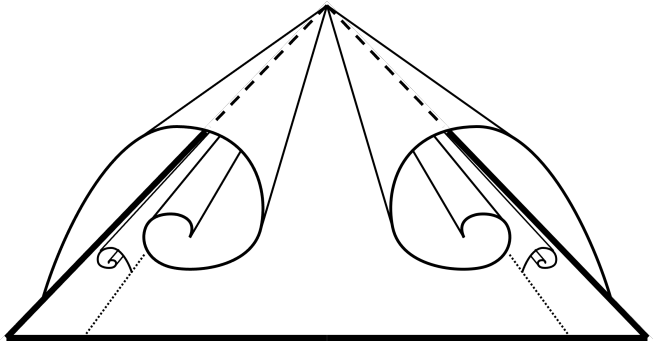

Figure 3.2 Cartoon of vortex sheets over a flat delta wing viewed from the rear.

number of parameters, which meant that the leading edge sharpness and cross-section shape could not be controlled as separate variables.

3.2 Boxfish

Boxfishes are tropical reef-dwelling fish of the genus Ostraciidae. All boxfishes have a rigid bony carapace covering their entire body, which has attracted interest from engineers looking for inspiration to improve performance of rigid engineered systems like underwater robots and automobiles (Kodati and Deng, 2006; Chen, Cai, and Bi, 2023; Qiu et al., 2023). While it is likely that the rigid exoskeleton evolved primarily for protection against predation, boxfish manage to swim and maneuver using a variety of gaits with their five fins (Walker, 2000; M. S. Gordon et al., 2000).

Boxfishes' unusual body geometries prompted a series of studies of the hydrodynamical function of their carapace shapes. Starting with I. K. Bartol et al. (2002) and Ian K. Bartol, Gharib, Weihs, et al. (2003), vortical structures similar to those over delta wings have been documented over various longitudinal keels when the fish are yawed or pitched relative to the freestream. This has been found

to be true for a variety of different species with substantially different morphologies, including on live swimming fish Ian K. Bartol, Gharib, Webb, et al., 2005; I K Bartol et al., 2008. There has been some debate about the impact of the carapace vortices on pitch and yaw stability, with different studies producing conflicting results (Wassenbergh et al., 2015; Boute, Van Wassenbergh, and Stamhuis, 2020), but all studies have confirmed the existence of such structures. Ian K. Bartol, Gharib, Webb, et al. (2005) posited that the longitudinal keels of boxfishes act similar to the leading edges of delta wings and that the concave region next to the keels may be important to create space for the vortex to occupy. This raises the question of just how much space is required for a leading edge vortex to exist, and how does an adjacent surface affect the growth and characteristics of such a vortex?

3.3 Objective

A sort of continuum of wing types exists described by aspect ratio or leading edge sweep in which the flow field varies from attached, primarily two-dimensional flow to being dominated by leading edge vortices caused by separation at the leading edge (Hirschel et al., 2021). Intermediate sweep angles, while historically less well studied than either extreme, exhibit interesting flow physics (M. Ol, 2001; Taylor, Schnorbus, and Ismet Gursul, 2003).

The existence of boxfish with similar leading edge vortex dominated flow field suggests a different continuum between flat delta wings and tall, contoured boxfish-like shapes, even approaching bluff bodies.

The intention of the current study is to begin to probe that spectrum of shapes, beginning with perturbations to the canonical flat slender delta wing. This also provides an opportunity to revisit geometries like triangular cross-sections with modern experimental methods like SPIV. In particular, we would like to provide experimental evidence on the effect of a surface proximal to a leading edge vortex on both the vortex and the overall performance of the wing. This can help to understand the basic physics and to begin to unravel possible design levers available to future designers of thick delta wings with subsonic performance requirements.

METHODS

The flow fields over delta wings of various surface contours were investigated using a combination of experimental techniques, including fluorescent dye visualizations, stereo particle image velocimetry (SPIV), and load cell measurements. Each of these methods, as well as the model geometries, are described below. All experiments were conducted in the FLOWTUB water tunnel described in the first part of this thesis.

4.1 Model Geometries

The basis of all the different delta wing shapes presented in this thesis is a 70° sweep flat delta wing with a chord length of 150mm. This flat wing has thickness of 3mm, and a 60° windward bevel at the leading edge. The top surface was then modified according to a custom parameterization to examine the effects of changing the leeward surface contour. All 3D modeling was conducted in SOLIDWORKS.

To minimize number of parameters involved and to retain the possibility of comparisons to conical theory, all models were designed with a conical apex region. First the centerline profile ($z_0(x)$) is defined running from the model apex to trailing edge in the x-z plane. As seen in Figure 4.1, this profile is linear from the leading edge to x/c=0.6, where a tangent 2-degree Bézier spline returns it to a height of 0 at the trailing edge. The free control point of this Bézier spline is placed at x/c=0.8, midway between the end of the conical section and the trailing edge of the wing. For the entire conical front portion of the wing, the profile height was set to match the local semi-span (y_{LE}) which produces a cross section that is twice as wide as it is tall. The resulting maximum height is about $y/c = 0.23$ and is attained aft of the conical section at approximately $x/c = 0.68$. These parameters result in an tangent angle of about 55.5° where the centerline spline meets the wing trailing edge. All models examined in this thesis (except the flat wing) share this same centerline profile.

To enable features like the concavities near the LE seen on the smooth trunkfish, the cross-sections of the models are described by a 3-degree Bézier curve (Figure 4.2). The cross-section profile curve is constrained to have a horizontal tangent at the model centerline and the leading edge (spline control points Q_0 and Q_3). The remaining two degrees of freedom (corresponding to the positions along the horizontal of spline control points Q_1 and Q_2) are set indirectly by specifying

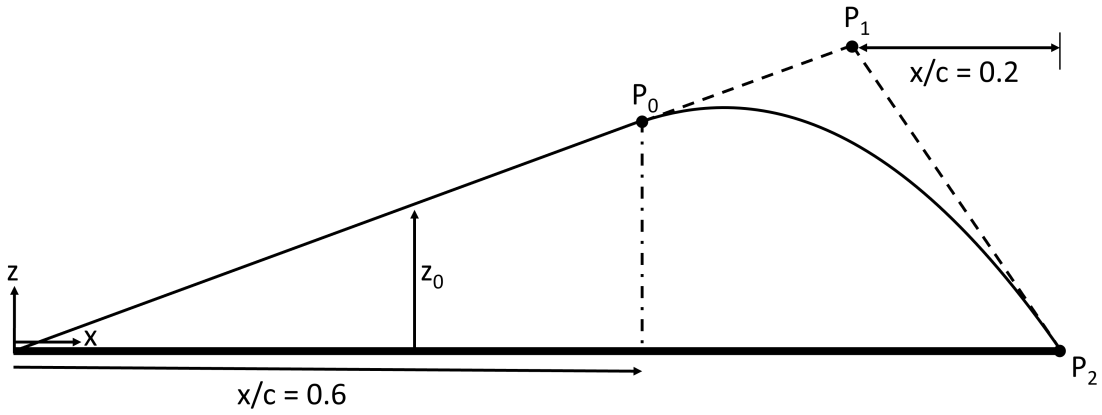

Figure 4.1 Centerline profile definition for contoured delta wings

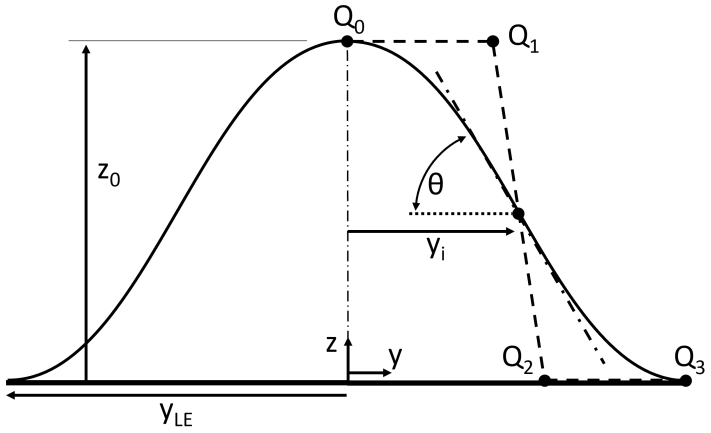

Figure 4.2 Cross-section profile of delta wing leeward surfaces

the location of the spline's inflection point (y_i) and the tangent angle (θ) at that point. In the aft section of the wing, the height of this cross section curve scales with spine height, while the width of the cross section continues to expand with the local span. The resulting surface is smooth everywhere to 2nd order, and is fixed at z=0 at both leading and trailing edges.

In the particular case where the inflection point is located on the midpoint of line Q_0Q_3, this point becomes coincident to the midpoint of line Q_1Q_2 and the spline becomes rotationally symmetric. Four of the models in this thesis comprise a family of shapes in this condition, changing only the value of the tangent angle θ to range between 45° and 90°. The symmetry of this cross-section ensures that all the models in this family have the same cross-sectional area (and thus the same internal volume) regardless of the value of θ. Cross-sections for this family of surfaces where $y_i/y_{LE} = 0.5$ are overlaid in Figure 4.3.

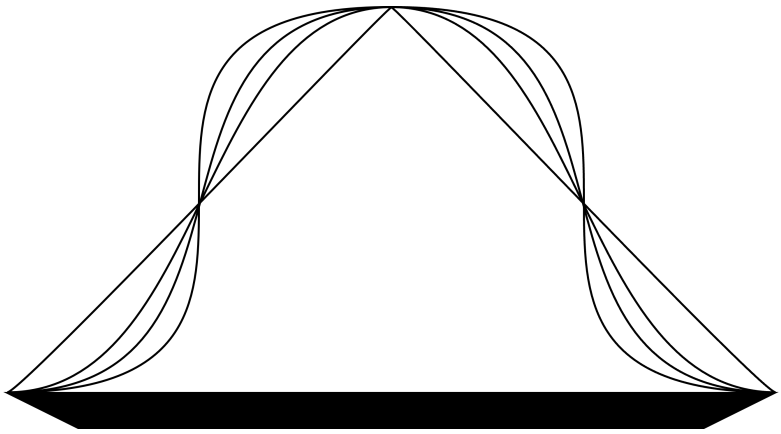

Figure 4.3 Cross-section geometries for $x/c < 0.6$ of a family of delta wing surface geometries in which $y_i/y_{LE} = 0.5$ and $\theta = 45°, 60°, 75°, 90°$.

Eight different model shapes were investigated, seven of which were generated with this parametrization. The remaining model was a variation of the flat wing with a vertical fence separating the wing along the centerline. The centerline profile of the the "vert" model matches all the other models, but the cross section deviates from the parametrization described above in that it is composed of orthogonal straight line segments. The thickness of the centerline fence expands from zero at the apex to about 3mm at $x/c = 0.6$, spreading at an angle of 2°. After $x/c > 0.6$, the fence has a constant thickness of about 3mm.

In addition to the models already mentioned, an extreme geometry was produced in which the cross-section is nearly semi-circular, heretofore referred to as the dome model. This model demonstrates the broad scope of this parametrization approach with the use of only two primary parameters: y_i/y_{LE} and θ. Notably, this parametrization maintains the same leading edge sharpness for all models except the dome and th45 models, which are less sharp due to a different surface tangency at the leading edge.

Parameters describing all eight models are listed in table 4.1. Cross-section profiles for all these models in the conical region are overlaid in Figure 4.4, cross-sections at different x-locations for each model are overlaid in Figure 4.5, and 3D wireframe views are provided in Figure 4.6.

On the windward side, a set of mounting tabs near the trailing edge allow the model to be bolted with countersunk flat-head M2 bolts to a 3mm thick stainless steel sting arm. Sting arms were cut from sheet stock on a water-jet table. Two dye injection ports near the model apex are routed through the models to a small hole at the rear, into which is inserted 1.5mm diameter stainless steel hypodermic tubing for dye injection. The ports for each model were designed to exit the model as

Model Name	x-section	z_0/y_{LE} $(x/c < 0.6)$	y_i/y_{LE}	θ [°]
flat		0.0001	—	—
vert		1	—	—
r001		1	0.01	88
th90		1	0.5	90
th75		1	0.5	75
th60		1	0.5	60
th45		1	0.5	45
dome		1	0.98	80

Table 4.1 Delta wing geometries and parameters

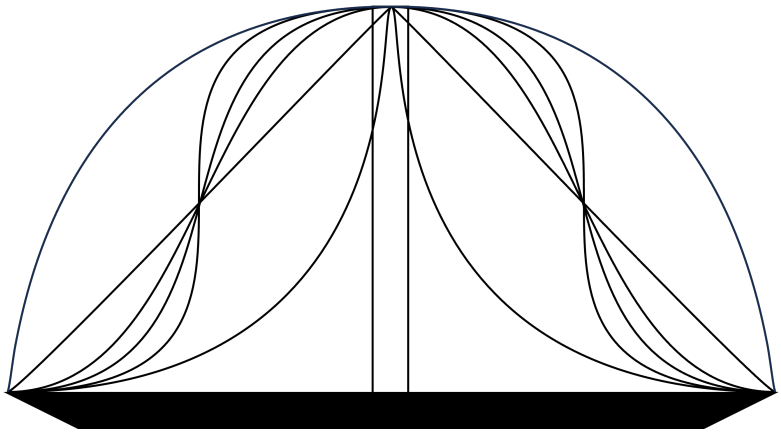

Figure 4.4 Delta wing surface cross-section geometries for $x/c < 0.6$

normal to the surface as possible.

Two different mounting orientations were used in the course of the experimental campaign. In the first, a long sting arm held the models with leeward surface facing downward (Figure 4.7a). In this configuration, the angle of attack was set manually and measured to a precision of $\pm 1°$ using a digital inclinometer. The second mounting configuration used a geared servo motor to set the angle of attack automatically, with the model's leeward surface facing the side wall of the test section (Figure 4.7b). In both configurations, the model and sting arm were suspended from an ATI Delta IP65 load cell which was mounted on a two axis gantry (Figure 4.8).

Each model was manufactured using a Phrozen Sonic Mega UV resin 3D-printer out of 3D-Materials ENGR-R42L resin. This particular material contains a proportion of inert ceramic dust meant to increase its stiffness and dimensional stability, with a quoted modulus of 6.0 GPa. It was

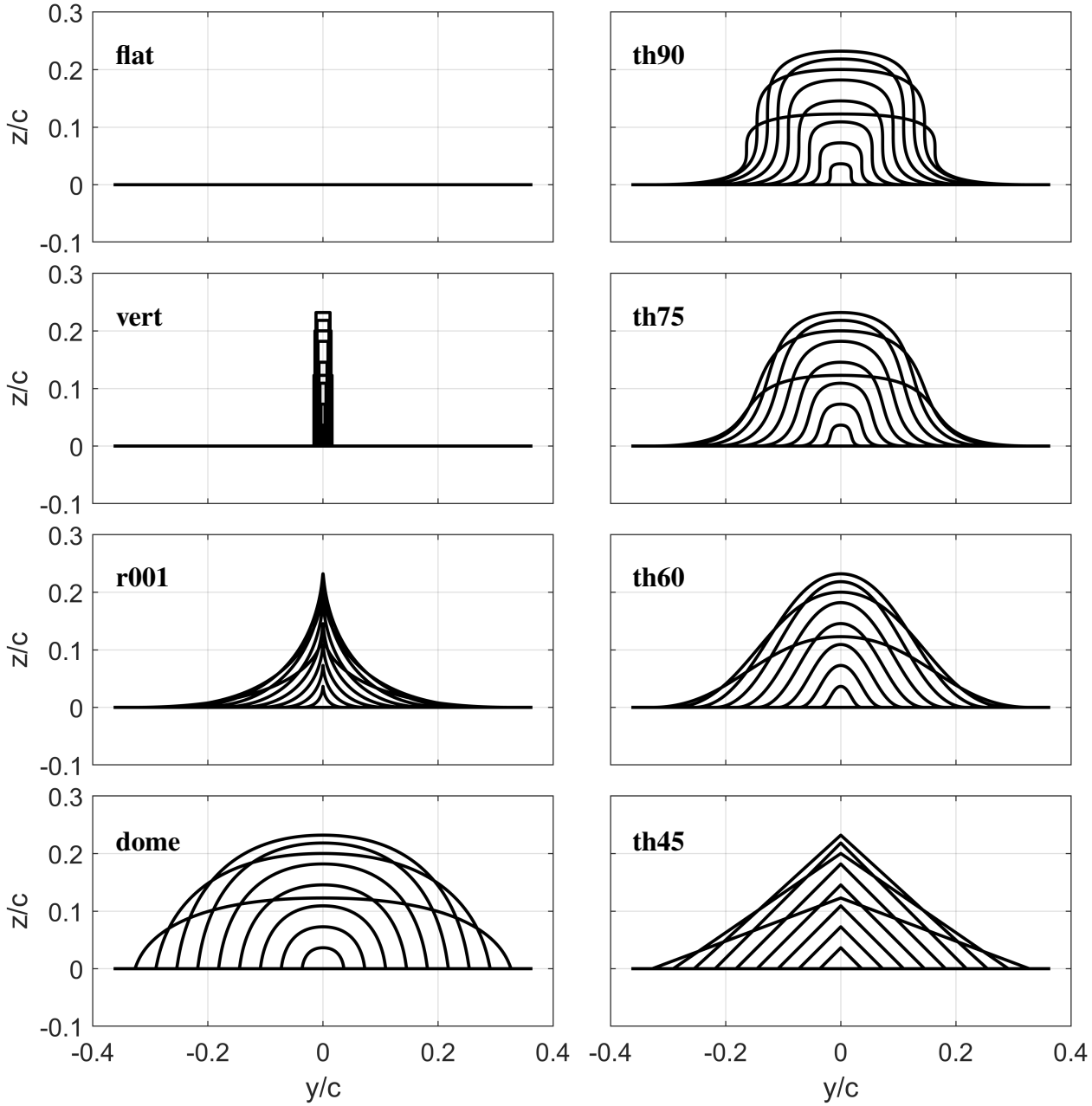

Figure 4.5 Delta wing model cross sections at x/c = 0.1, 0.2, 0.3, ... , 0.9, 1.0. Leeward bevel and bottom z/c = 0.02 not pictured.

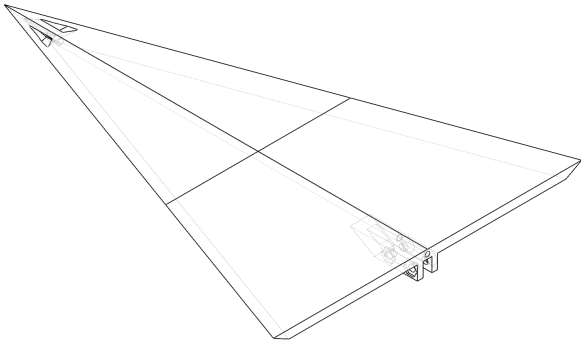

flat

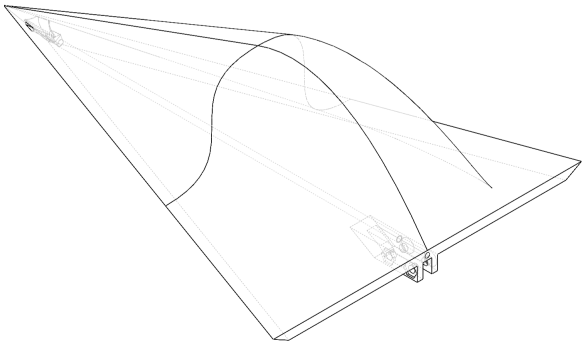

th90

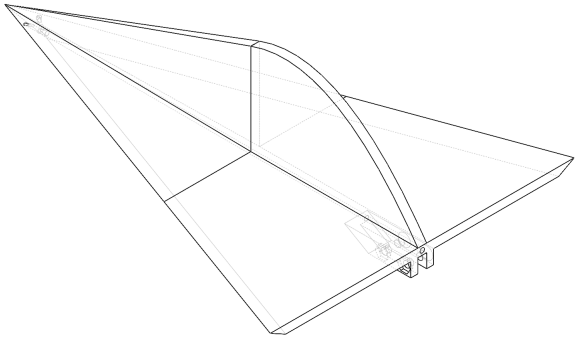

vert

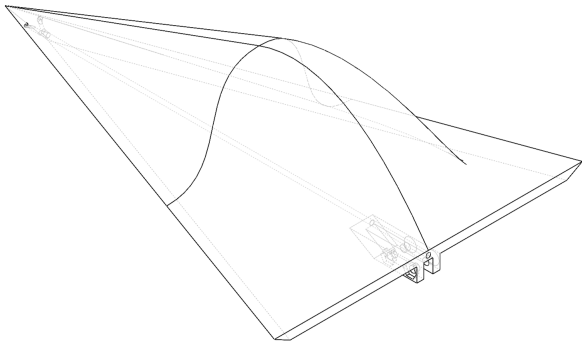

th75

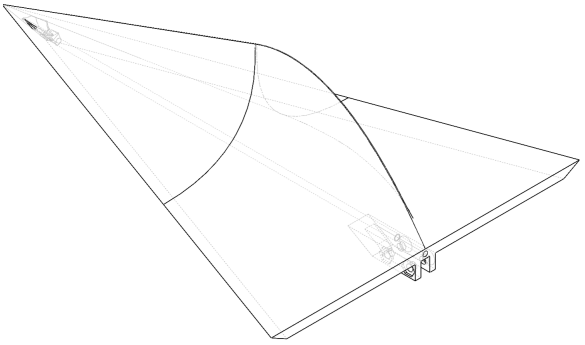

r001

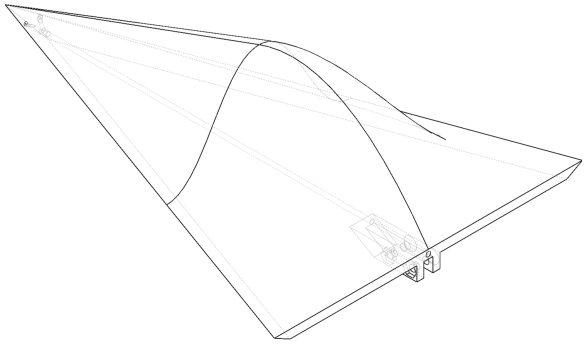

th60

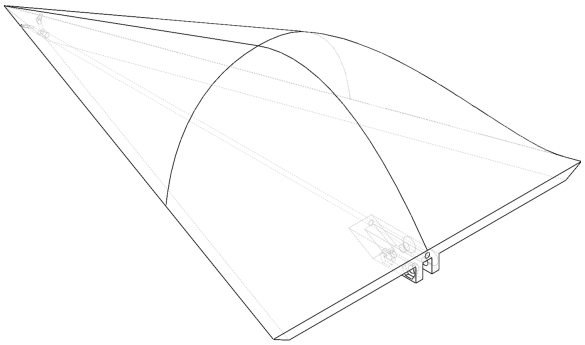

dome

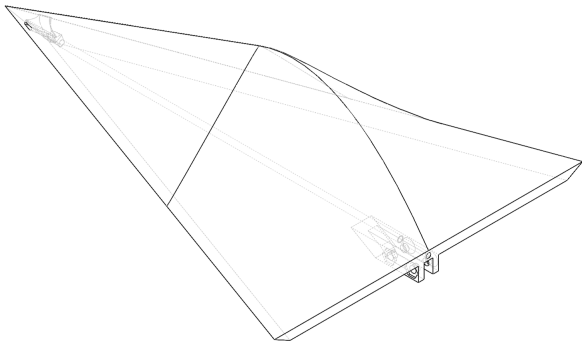

th45

Figure 4.6 3D CAD wireframe views of all delta wing models

(a) inverted (b) horizontal

Figure 4.7 Delta wing mounting configurations off of gantry. Gantry and tunnel not pictured for clarity.

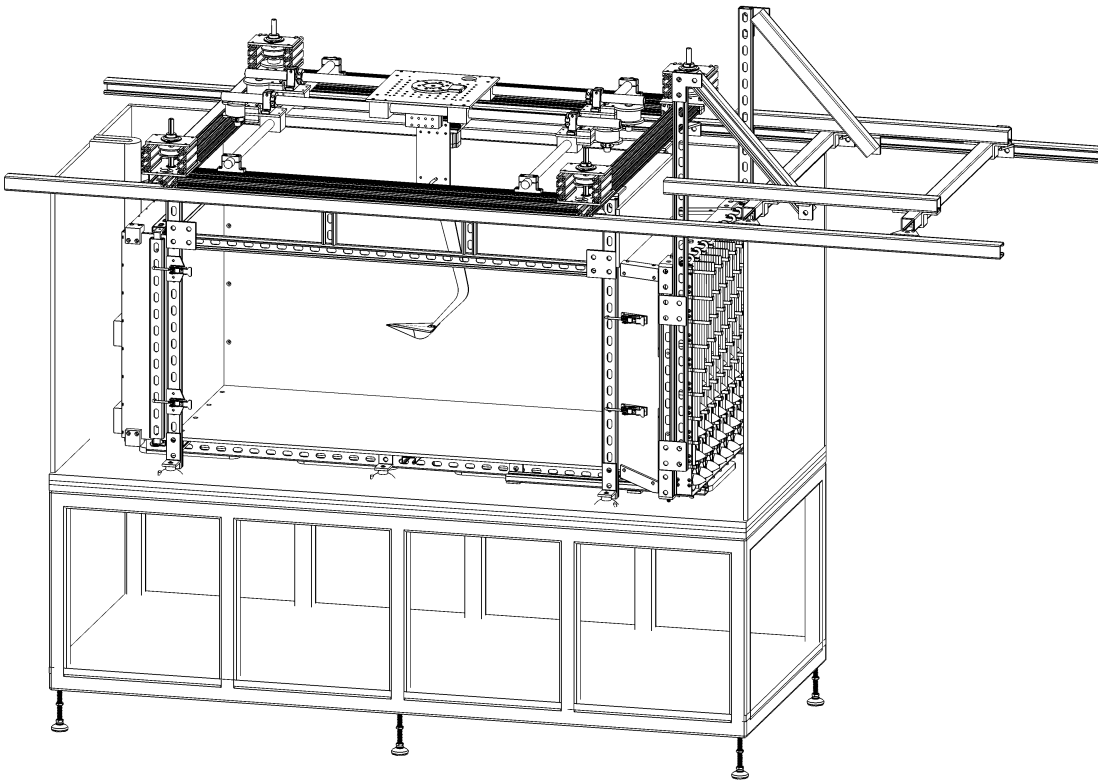

Figure 4.8 Wireframe CAD of tunnel with superstructure, gantry, and delta mounted inverted on sting arm.

difficult to mitigate the problem of models warping after printing, particularly in earlier attempts with Phrozen's Aqua Grey resin. Models printed with the ENGR-R42L resin hold their shape best when not exposed to UV light, including the fluorescent lights in the laboratory. All models were painted black after post-curing, both to protect them from UV, and to reduce their reflectivity for flow visualizations and SPIV studies.

4.2 Fluorescent Dye Visualization

As has been noted by many previous authors (Lambourne and Bryer, 1962; Owen and Peake, 1986; M. Ol, 2001; Erm and M. Ol, 2012), the strong vortices of the delta wing flow field lend themselves well to visualization by dye injection in water tunnels. This was a factor in the decision to use a low-speed water tunnel for this investigation. Dye injected near the model apex tends to be swept into/around the leading edge vortices, rendering them visible to an observer or cameras. Two implementations were used to capture dye flow visualizations. In the first configuration, one camera was placed under the tunnel, and one to the side. In the second configuration, the camera setup for SPIV (described in Section 4.3) was repurposed to image dye in the plane normal to the freestream flow direction and a gantry was used to capture three-dimensional tomographic images.

2D Dye Visualization

For the 2D dye visualizations, the model was positioned inverted such that the leeward flow field could be imaged simultaneously in two orthogonal views. A 10W continuous diode laser (the same used during the tunnel characterization PIV and later for SPIV) was expanded through two orthogonal cylindrical lenses to illuminate the entirety of the leeward flow field. For all models save the flat wing, the starboard side of the model is shadowed by the model surface, so the dye on that side is not visible. Two IDT IDT XStream Mini-3520 cameras with Rokinon T1.5 50mm AS UMC Cine DS lenses and Tiffen red 25 filters were focused on the lee-side of the wings, one through a window below the tunnel, and one from the port side. A schematic of this arrangement is provided in Figure 4.9.

Dye was injected through a pair of injection ports in the model leeward surface near the apex, driven by a Harvard Apparatus PHD 2000 syringe pump. The typical procedure for acquisition of steady flow two-view dye visualizations was to turn on the tunnel, wait 30 seconds to avoid startup effects, then start the dye injection and camera recording at 100 fps for two seconds. Recordings were also taken in which dye was only injected prior to the tunnel turning on, to provide a validation case in which no dye is injected during data acquisition. The flow visualizations obtained in this manner agree well with the steady dye injection visualizations, but are not presented here because they have

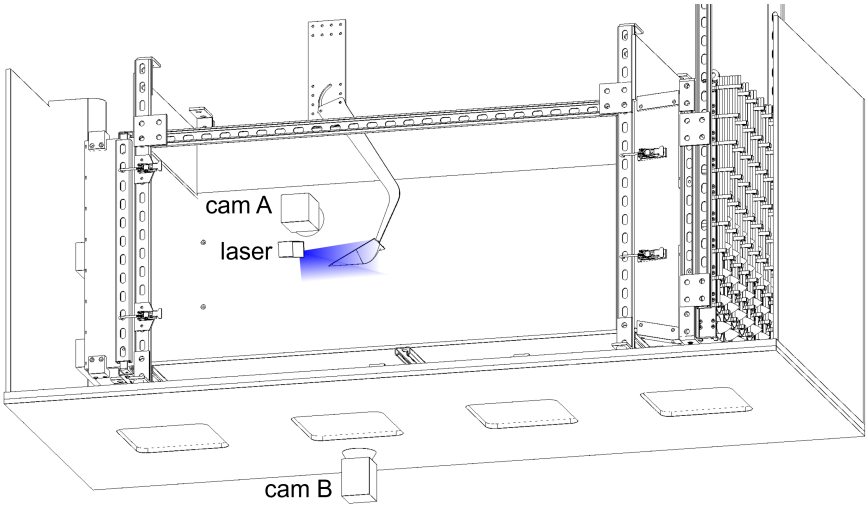

Figure 4.9 Schematic of 2D dye testing configuration. Syringe pump, dye injection tube, and supporting structures not pictured.

lower contrast.

Two sets of images were taken of each model at three angles of attack, 10°, 20°, and 30°. The first set of images was taken without dye injection with the model illuminated by white flood lights. These images were used to determine the model's position and orientation in each view. A custom matlab post-processing script streamlined the process of manually identifying points on the model edges. The second set of images were recorded with the flood lights off, the laser and dye injection on, and the water tunnel operating at a speed of 10cm/s, Re 15300 based on model chord. Several dye injection flow rates were used ranging from 3 to 16.6 mm^3/s. These flow rates through the injection ports on the models produce flow speeds less than 5% of the freestream.

As a simple validation of this dye injection, additional tests were run in which dye was injected for a few seconds with the tunnel off, forming a region near the model apex with high dye concentration. After halting dye injection, the tunnel was then rapidly brought up to speed, which caused the dye to sweep over the models and visualize flow structures. This method minimizes any potential impact of the dye injection on the visualized flow, but results in much lower contrast images because the dye concentration decreases with time. Because of this limitation, startup image sequences were recorded for less than 10 convective times based on freestream speed and wing chord. Thus these sequences may not converge to the steady state flow configuration.

The images from the side view and top view of the wing were then used to identify the location of the leading edge vortex relative to the leading edge using a custom MATLAB script. Images

were filtered with imbinarize, bwareaopen, and imclose. Next regionprops was used to identify the LEV based on its aspect ratio and orientation. Finally, the group of pixels representing the LEV was fit with a line in the conical apex region. Repeating this procedure in the top and port view images provided measurements of the LEV angle inboard of the leading edge, and elevation angle above the wing z=0 plane. With a bit of simple trigonometry, these angles were used to calculate the position of the LEV in the model z-y plane.

Tomographic Dye Visualization

The second dye-visualization technique took images of injected dye in a plane normal to the freestream direction. By translating the wing through a stationary laser sheet while injecting dye, a full 3D tomographic image can be captured. A similar technique was employed by Yoda and Hesselink (1990) with a scanning laser sheet and stationary model. This setup was optically identical to the SPIV configuration described below (Figure 4.10), but additionally used the x-axis of a gantry system installed above the tunnel to translate the models through the laser sheet as the camera recorded continuously. The wings were oriented in the horizontal configuration, with angle of attack controlled by the gantry (Figure 4.7b). The model was positioned such that the maximum extent of the leeward port side of the wing could fit within the camera's field of view, in some cases missing part of the wing apex or wingtip. Only camera A was used for these experiments, with a Tiffen Yellow 2 #8 filter placed between the lens and sensor to cut out most of the blue laser light while leaving the model surface visible. Dye was injected near the apex as in the 2D dye visualizations, and from a 1.5mm outer diameter stainless steel tube run from the trailing edge along the model surface to $x/c = 0.86$.

The tunnel flow speed during these tests was 10.0 cm/s. The model was always started with the apex 3 cm downstream of the laser sheet and ended with the trailing edge 3mm upstream of the laser sheet. At the start of each run, the gantry moves to the start position, the tunnel ramps up, the program waits at least 25s to reach steady state, then the dye and camera are triggered as the model begins to move forward at a constant speed of 5 mm/s. This movement results in a total flow velocity over the models of 10.5 cm/s, or a Reynolds number of 16500. Images were recorded at 30 fps at maximum exposure (33ms), so each exposure captures 21 convective time units ($\tau = (U_\infty + U_{gantry})/\Delta t_{frame}/\Delta x_{frame} = 1 + U_\infty/U_{gantry}$) at a given cross-section.

This creates a series of images with an x-y resolution of 0.04 mm/px and a linear spacing in z of 0.167 mm. Each image was dewarped using calibration images and the PIVmap software distributed by PIVtec. Under the assumption that the flow-field is essentially steady in time, each sequence of images was stacked together into a 3D image of the model and dye using 3D-slicer software (Fedorov

et al., 2012). First the images were imported through the SlicerMorph module (Rolfe et al., 2021) using the ImageStacks utility, then reconstructed into a volume in the Volume Rendering module.

4.3 SPIV

The flow field over a delta wing of finite chord is inherently three dimensional, so flow measurement techniques capable of producing three dimensional measurements can be particularly useful. One such technique is stereo particle image velocimetry (SPIV), which uses the perspective difference between two (or more) cameras to combine simultaneous 2D velocity measurements of the same planar field of view to calculate a three-component velocity field.

Two IDT XSM-3520 cameras were used with Rokinon 135mm T2.2 Cine DS lenses. The water was seeded with hollow silver-coated glass spheres (Potters Industries Conduct-O-Fil® SH400S20). The laser was a 445nm 10W continuous diode laser originally intended for engraving. Two sets of cylindrical lenses were used to focus the laser in the streamwise direction to a thickness of around 0.5 mm and expand it to a height of around 10 cm where it intersects the cameras' field of view. Using two opposing lenses in each axis makes it possible to finely adjust the laser focus/expansion by varying the spacing between the lenses.

SPIV measurements were acquired on a single cross-section plane oriented normal to the freestream direction and intersecting the models at $x/c = 0.5$, in the conical region of the models. To maximize the measurement resolution, only the leeward port side of each model was imaged. All SPIV data was acquired at AOA 20° with a freestream speed of 10.2 cm/s (Re 15500). Camera exposure was set to $1050\mu s$ at a rate of 600 fps for 200 frames.

Viewing arrangement

The complexity in SPIV measurements derives from the necessity of imaging the field of view with cameras positioned off-axis. To achieve similar accuracy for the in-plane and out-of-plane velocity, the two cameras should have an angle of roughly 90° between their viewing axes, or a 45° angle to the object plane. Such extreme viewing angles are necessary to produce the parallax that contains depth information, but requires a different lens position relative to the camera sensor to produce focused images. A rotational scheme such as is described by Willert (1997) and M. Ol (2001) was used here. The lens and camera were rotated such that the lens plane, sensor plane, and object plane all intersect at the same line according to the Scheimpflug criterion.

Without optical access from the rear of the water tunnel test section, the only viewing arrangement which enables two orthogonal cameras to view a cross-section of every model without occlusion at all angles of attack less than 35° is with both cameras looking through a single side wall of

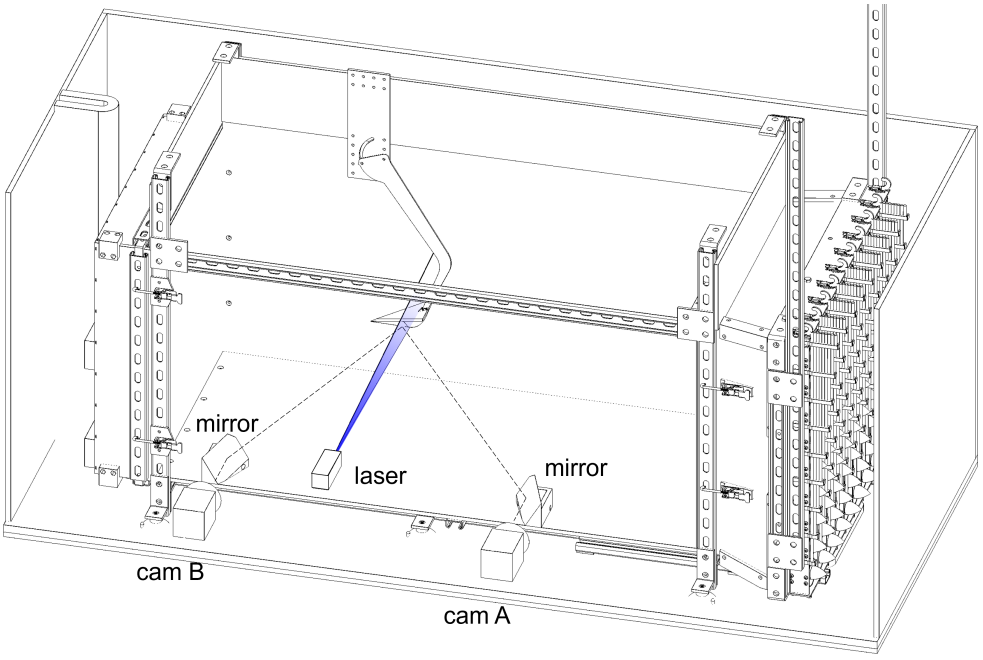

Figure 4.10 Schematic of SPIV testing configuration. Centerline of optical path is indicated as a dotted line. Lenses for laser and camera, camera orientation, gantry, and support structures are not pictured.

the tunnel. Conveniently, this arrangement leaves space for a laser sheet to enter the tank directly between the two cameras through the same wall. A schematic of this arrangement is given in Figure 4.10

An additional complication exists for water tunnel experiments as compared to wind tunnel experiments due to the index of refraction difference. These can be mitigated either using water-filled prisms or mirrors placed inside the tank to make the refractive interface normal to optical path (Raffel et al., 2018). The latter choice was selected in this case because it was hoped to be simpler to implement, and can avoid the slight astigmatism that is introduced by looking through an oblique sheet of material with a different index of refraction. Initially, mirrors were placed outside the water tunnel test section in the return flow where they would have minimal impact on the test section flow. However it was found that looking through the 10 cm thick acrylic test section walls at an oblique angle caused a significant astigmatism, despite having water on both sides. Instead, both mirrors are placed inside the test section in the bottom corners as far from the model as possible. The positions of the mirrors, camera, lens and wing were modeled in SOLIDWORKS to design an arrangement in which both cameras could view every model's entire cross section at any angle of attack below 35°. Custom 3D-printed mounts hold each mirror at the pre-determined optimal

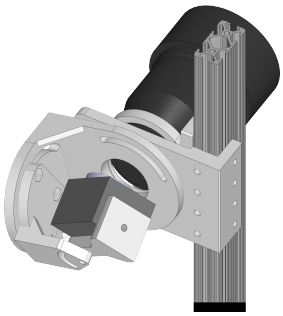

Figure 4.11 CAD of custom camera tilt and rotate adapter behind separately mounted lens.

angle. A stainless steel bar connects the two mirror mounts and enforces their streamwise location within the test section. The mirror mounts rest on the test section floor against the test section wall and are weighted with lead to discourage movement.

Custom mounting and alignment hardware holds the lenses, cameras, and laser. The lens mount is always positioned normal to the tunnel wall. The camera mount has three degrees of freedom; allowing for the camera sensor plane to be rotated about the sensor normal, tilted about a vertical line in the sensor plane, and for the axis of that tilt to be rotated about the lens axis. All of these rotations are facilitated by a PLA 3D-printed mount which was designed to maintain the position of the sensor plane center point relative to the lens in all orientations (Figure 4.11). This setup decouples the degrees of freedom relevant to the alignment of the camera, mirror, lens, laser, and wing to the greatest practical extent.

Alignment procedure

Alignment of this system begins with placement of the mirrors at the predetermined location and orientations. The laser is aligned to produce a vertical sheet of light spaced midway between the two cameras. The laser plane is aligned normal to the tunnel wall by ensuring that the laser light reflected off the tank is coincident to the incoming light. Next the lenses are positioned normal to the tunnel wall pointing at the center of each mirror, and the camera is placed behind the lens with its sensor plane rotation set such that the camera view is aligned to the tilt axis of the camera mount. The camera focus can then be adjusted such that the focal plane intersects the laser plane. This produces an image of a particle field in which only a single line is in focus. This is why the Scheimpflug criterion is necessary. Because the camera axis is aligned to the tilt axis, the tilt axes is rotated about the lens axis until the camera image shows that the focus line is aligned with the tilt axis. The sensitivity of this technique is best when the camera aperture is widest (narrowest depth of field). The camera is then tilted until the entire field of view is as focused as possible.

At this point both cameras are focused, but still need further alignment to ensure they both see the region within the laser plane. A model is mounted within the laser plane and the cameras and lenses are translated relative to the mirrors to align the views of both cameras to one another. This of course necessitates that the tilt alignment procedure be repeated. Once the cameras are focused on the same field of view as well as is practical, the cameras can be rotated about the sensor axis to optimize the orientation of the field of view without affecting the tilt alignment. In practice, this whole process must be repeated several times to produce satisfactory results. In all cases, astigmatism and coma in the final focused images required the camera aperture to be closed somewhat to increase the depth of field at the expense of the amount of light.

Calibration and processing

The Scheimpflug criterion ensures that the object plane is in focus, but the amount of magnification varies across the field of view. This effect must be removed via a calibration. A calibration target was constructed consisting of a grid of 1mm diameter black dots spaced 2mm apart printed on a sheet of transparency film. The transparency film was sandwiched between two 1.5mm thick sheets of acrylic plastic using UV curing Norlan Optical Adhesive 68. A combination of laser-cut acrylic and a 3D-printed adapter connect this sandwich to the same mounting arm used for holding the wing models, which simplifies the process of switching out the calibration target for a model and vice-versa. A calibration target constructed in this manner was suggested in Raffel et al. (2018). A gantry above the tunnel was used to translate the calibration target from -1.2mm to 1.2mm relative to the laser plane in 0.4 mm increments to acquire seven calibration images.

It was found that deformation of the test-section wall during tunnel operation (caused by the pressure difference between the test section and the return path) was large enough to displace the field of view of the cameras to such a degree that calibrations taken when the tunnel is off are not valid when the tunnel is running. Therefore calibrations were recorded with the tunnel set to the same speed as the SPIV measurements (10.0 cm/s). This caused the calibration target to vibrate with a less than 0.5mm amplitude, presumably due to bluff body vortex shedding. This challenge was circumvented by recording a time series of calibration images at each position and using only the median image for calibration purposes.

PIVmap3, a software program packaged with PIVview by PIVtec, was used for calibration grid detection and to compute an order 1 non-linear back-projection mapping, and to estimate camera positions based on a first-order pinhole camera model. PIVview3C was then used for both the two-dimensional DPIV analysis and trigonometric stereo reconstruction based on the camera position model. For each camera view, three pass multi-grid cross-correlation was used to extract a 2D

velocity field ending with 32x32px windows and 50% overlap. Residuals in all cases were at or below about 0.5px.

Post-processing

The velocity field output by PIVview permits the calculation of the out-of-plane vorticity. After averaging the velocity field through time, vorticity was calculated based on a circulation estimate around the neighboring eight points as described by Raffel et al. (2018). To identify an approximate boundary of the LEV, a thresholded region in which $z/y_{LE} > 0$ and $\omega > 2.5/s$. Thus this boundary contains both the LEV and the leading edge shear layer. The total circulation in this region was calculated using a trapezoidal integration scheme, and diffusive vorticity fluxes around the region boundary were computed as described by Eldredge and Jones (2019). The location of the center of the LEV was estimated by the peak of a 2D paraboloid fitted to the 3x3 neighborhood of the peak vorticity value. Profiles of several quantities including azimuthal (Ux) and axial velocity (Uz), vorticity, and local helix angle ($atan(Ux/Uz)$) were also computed and plotted in a horizontal line ($z = const.$) through this peak.

4.4 Force Measurements

A six-axis ATI Delta IP65 load cell was used to measure the lift, drag, and pitching moment of the wings. The quoted resolution of this load cell is 0.031 N, 0.0019 Nm. At a freestream speed of 10 cm/s, the dynamic pressure experienced by the wings is only around 5 Pa, and the wing planform area is around 0.008 m^2, so the maximum lift force at $C_L \approx 1$ is of the same order as the load cell resolution. Fortunately, the quoted resolution can be dramatically improved upon for steady state measurements by averaging out high-frequency noise over a suitably long time period. Another limitation on the measurement accuracy is drift of the load cell voltage output, which is likely caused by slight temperature variations. Drift is minimized by turning the load cell on more than 15 minutes before taking measurements, but some non-linear drift is unavoidable. By taking null recordings before and after each measurement this drift can be removed to first order. This sets up the classic tradeoff between longer recording times minimizing random errors and shorter recording minimizing bias error. A simple Allan variance experiment was conducted to determine that a recording length of about 60s produces the lowest uncertainty.

To measure the forces on a model, first a null is taken with the tunnel off, then the tunnel is turned on and after 30s for the tunnel to reach steady state the model forces are recorded. The tunnel thrusters are then switched off and after another 30s a second null is recorded. This process is repeated 20 times for the same angle of attack. The sting arm is mounted on a servo motor

which can control the angle of attack to within 0.1°. A custom python program automates this procedure such that a full angle of attack sweep can be acquired without any manual intervention after installing the appropriate model. To improve the accuracy of the non-dimensionalization, an MSE mini-LDV G5B system was triggered to record the freestream velocity at the same time as the force measurements. The freestream speed was 10.1 cm/s on average during these tests, yielding a Reynolds number of 16200.

Post-processing of these measurements was conducted using a custom post-processing script in Matlab. Linear drift for each run is determined from the two nulls and is subtracted off. All 20 runs are then averaged together to get an estimate of all three components of force and moment in the load cell reference frame. Separately, the same procedure is followed without the model mounted to measure the forces associated with only the sting arm. These forces are subtracted from the model measurements to isolate the forces and moments on the model. Next the lift, drag, normal force, tangential force, and pitching moment are calculated using the known offset and rotation from the load cell reference frame to the wing mid-chord, which is the theoretical aerodynamic center (Schlicting and Truckenbrodt, 1979). A 95% uncertainty associated from the variation within and between runs for a single model and the sting-only forces are propagated to first order to produce the error bars on the reported plots. The freestream velocity, water density, wing planform area and mean aerodynamic chord are all used to compute aerodynamic coefficients from the dimensional forces. Water density is determined from water temperature measurements made with an analog thermometer under the assumption of 1 atm atmospheric pressure. Zero degrees angle of attack was set as the angle at which the flat delta model produced zero lift.

RESULTS

5.1 2D Dye Visualizations

Summaries of the top and side dye visualization views of all the delta wings are presented in Figures 5.1 and 5.2. Dye injected near the apex leading edge is swept into the leading edge vortex, rendering it visible. It is worth noting here that only flow structures which are seeded with dye become visible, so other flow structures may exist which are not visualized with this technique. LEVs on some wings appear thicker than others, but this is primarily a function of the dye being entrained at some distance from the vortex core, causing a spiral pattern which manifests as a wavy line in a 2D image. Each image presented in Figures 5.1 and 5.2 is a single frame out of a 2s sequence captured at 20 fps. The position of the primary and secondary vortices was found to be quite steady through time, which enabled the tomographic dye visualizations described in Section 5.4.

A clear LEV is observed in all cases except the th45 wing at 10° AOA and the dome wing at all angles, where the dye remains attached to the surface before separating off the back end. The LEVs over all models follow a linear trajectory in the conical region of the wing ($x/c < 0.6$). Models with thickness contours generally have the LEVs displaced outward closer to the leading edge (top view) and upward away from the wing surface (side view). After the conical region, the displaced LEVs tend to curve inwards as they approach the trailing edge.

Secondary vortices are also evident in some cases. Over the flat model, clear secondary vortices can been seen to burst near $x/c = 0.5$ for AOA 10° and 20°. Similar secondary vortices are observed over the vert and r001 wings at 20°, with a significant delay in bursting over the latter. At 30° secondary vortices are observed near the apex of almost all of the wings, the only exceptions being and th90 wing. The th75, th60, and th45 wings exhibit particularly long-lasting secondary vortices at 30°, bursting not much sooner than the primary LEV.

At 20° AOA, vortex bursting is visible near the trailing edge for models th75, th60, and th45. All models exhibit LEV bursting at AOA 30° at a similar chordwise position around $x/c = 0.7$.

Injecting dye only before turning the tunnel for a 20° angle of attack for a subset of models on yields similar results (Figure 5.3). With a broader initial dye location, additional features are visible including secondary vortices and structures aft of the wing's maximum thickness. These frames

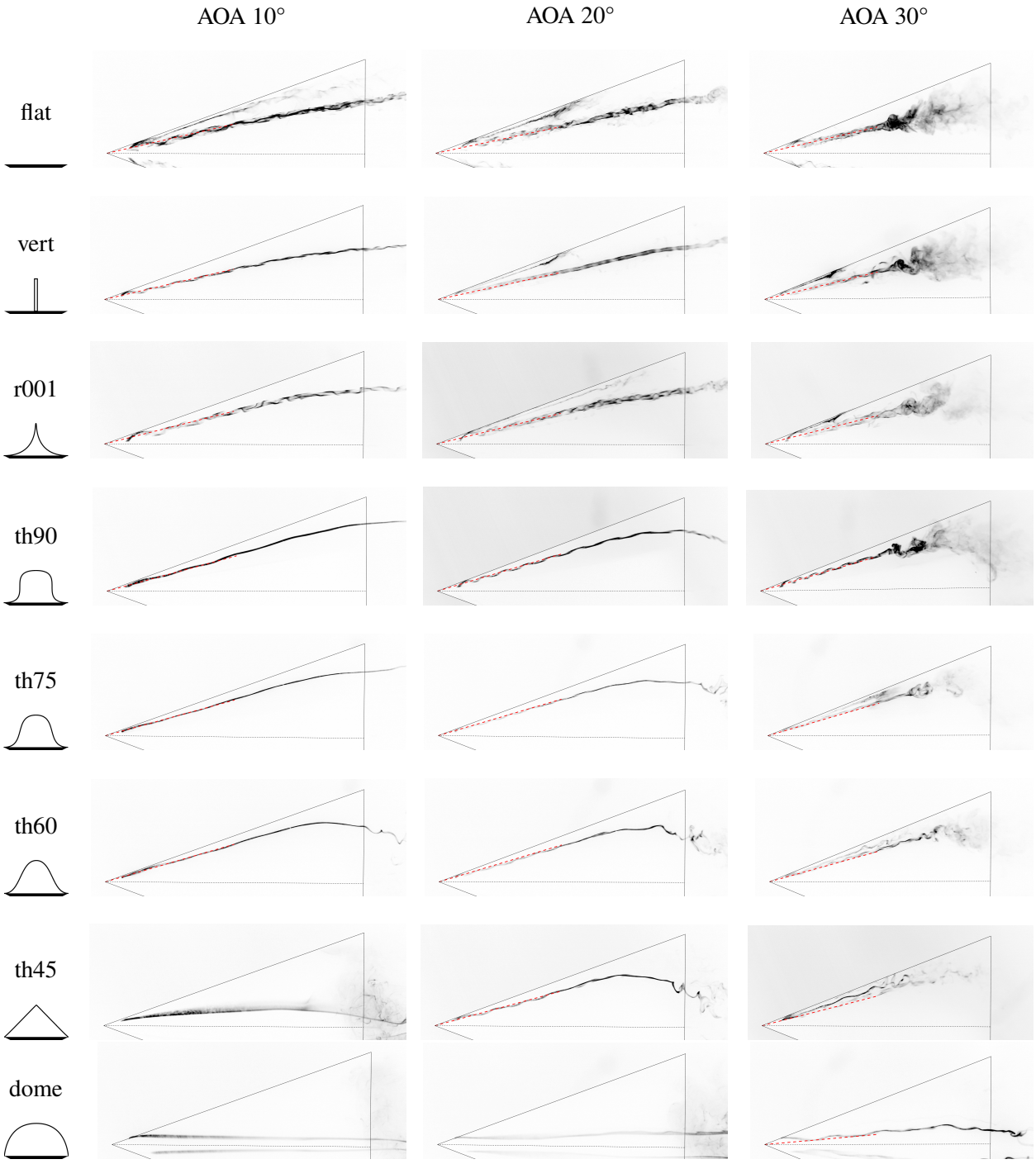

Figure 5.1 Top views of fluorescent dye over delta wing models at Re 15,300. Wing leading and trailing edges are outlined in black for clarity, centerline is denoted with dotted black line. LEV position is indicated by a red dashed line. Only port side of wings are shown; images are flipped vertically.

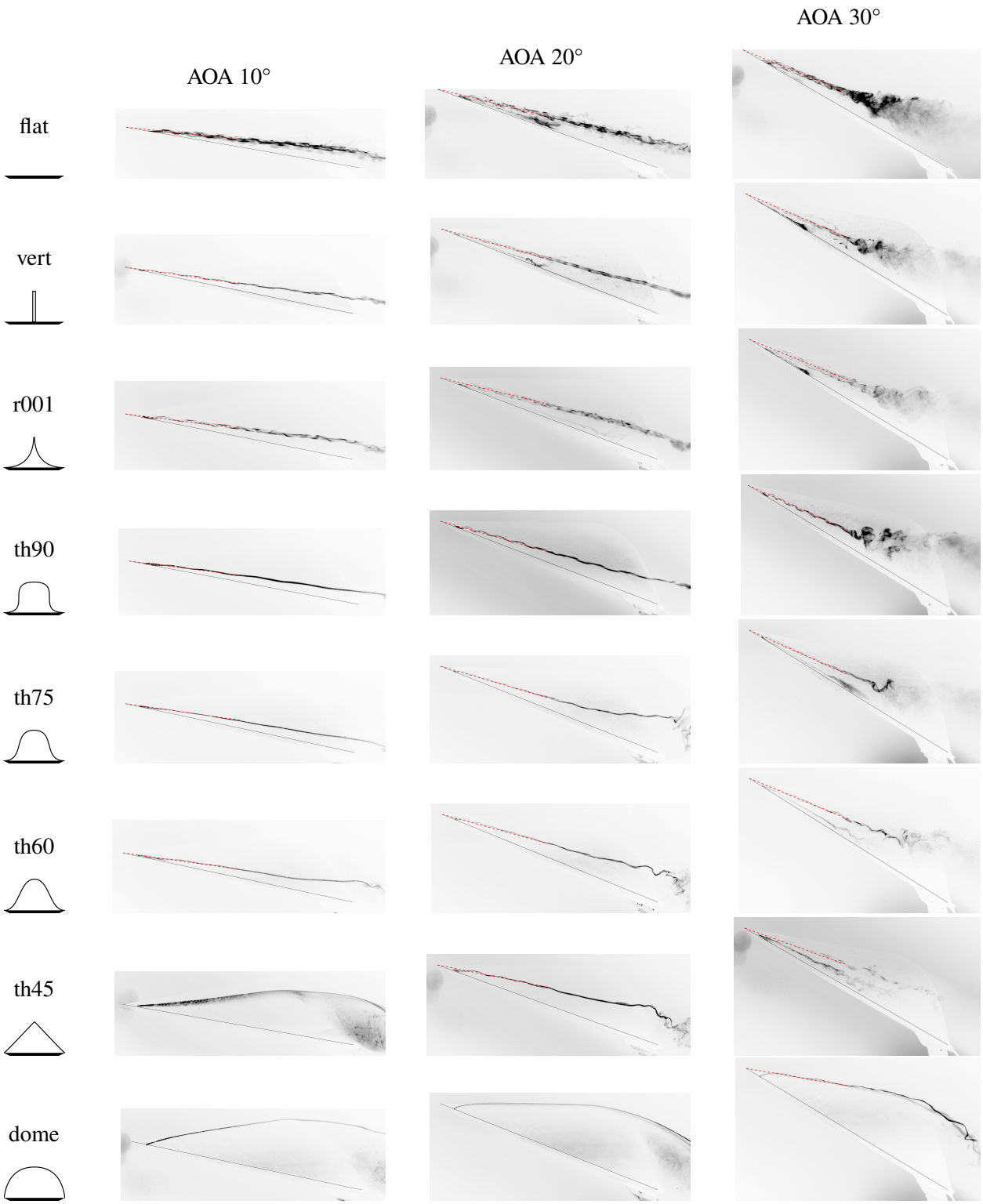

Figure 5.2 Port side views of fluorescent dye over delta wing models at Re 15,300. Wing leading edge is outlined in black for clarity. LEV position is indicated by a red dashed line.

were captured roughly 4 convective times after the start of the tunnel based on wing chord and final freestream speed.

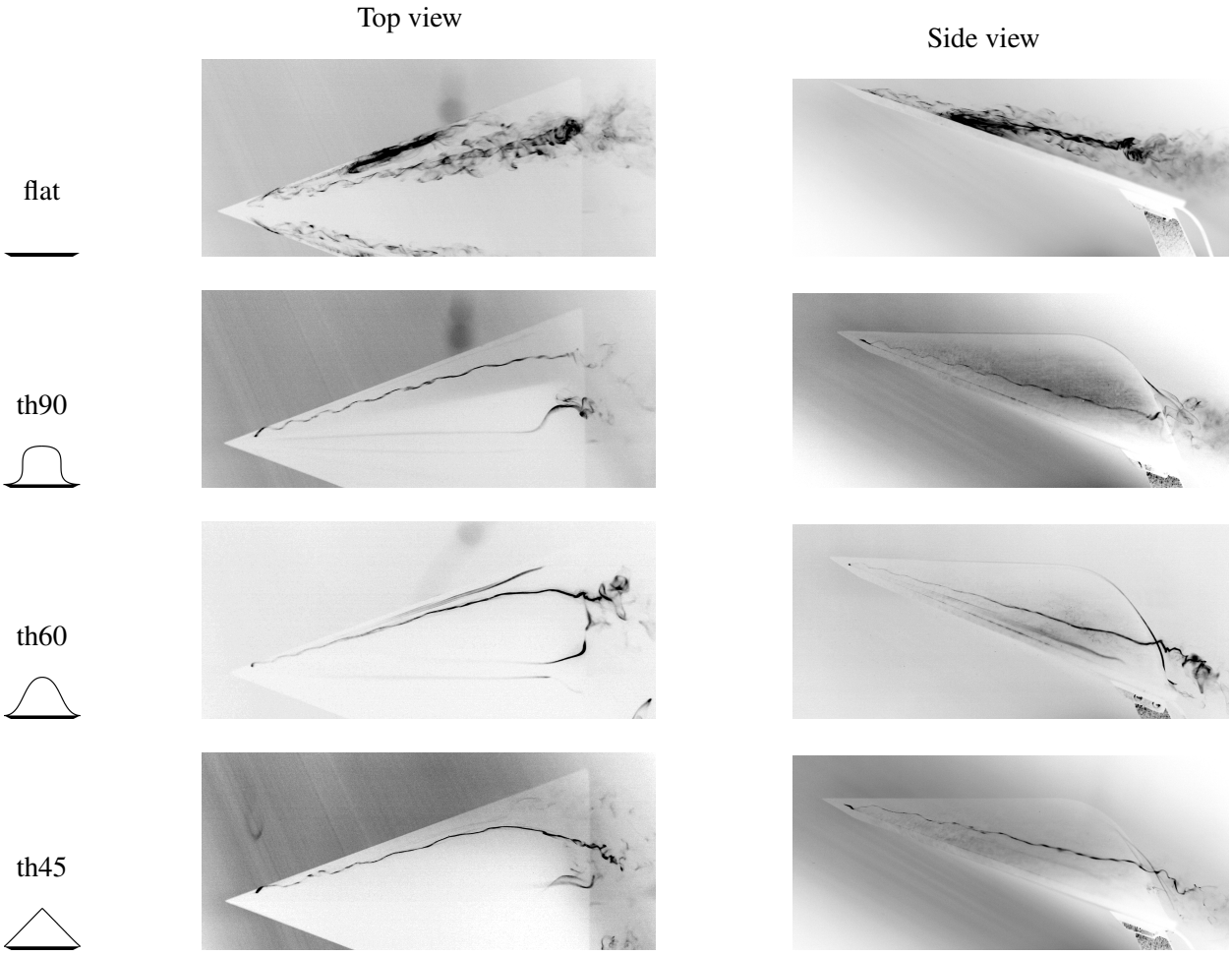

Figure 5.3 Top views and side views of fluorescent dye over delta wing models after impulsive start to Re 15,300. Only port side of wings are shown; images are flipped vertically.

Leading Edge Vortex Location

Changes in the leading edge vortex position extracted from Figures 5.1 and 5.2 are summarized in Figures 5.4 and 5.6a. For the flat model, as angle of attack increases, the LEV shifts upward away from the wing surface and slightly inward toward the wing centerline. This trend generally holds for all the tested wings. Wings with larger cross-sectional area, particularly the th90 and th75 wings, maintain a constant LEV spanwise location as the AOA is raised from 10° to 20° before shifting inward at 30°.

Compared to a flat wing, models with larger cross-sectional area have LEVs farther outboard (away from the wing centerplane). The vertical position of the LEV can either increase or decrease with cross-sectional area. At 10°, the LEVs over all wings are at approximately the same height. Models with a smaller surface slope in the vicinity of the flat plate LEV position (th45, th60, r001) have elevated LEVs at 20° and 30°. Conversely, models with steeper surfaces (th75, th90) have LEVs closer to the model x-y plane than the flat wing at high angles of attack. This information is presented more directly in Figure 5.5 and 5.6a, which show each model's cross-sectional shape along with the LEV location in the cross section plane. Generally, the LEV appears to be displaced in a direction related to the local surface normal direction.

The distance of the LEV to the nearest point on the wing surface tends to decrease as the model surface is raised in the vicinity of the LEV (Figure 5.7a). The angle of the vector connecting the closest point on the wing surface to the LEV depends on the particular cross-sectional shape and angle of attack (Figure 5.7b). As the LEV tends to move inboard and upward with increasing angle of attack, the nearest point on the model cross section changes. For the th90 wing for example, at 30° the LEV is positioned horizontally from the nearest point on the wing surface, which has a vertical slope.

5.2 SPIV

The two dimensional dye visualizations described above showed that all models have a well defined LEV at 20° AOA, but that the location of the LEV and the existence of secondary vortices varies across model shapes. To further understand the differences in the apex region flow fields, stereo PIV measurements were taken at $x/c = 0.5$, which the dye visualizations have demonstrated is within the conical apex region of each wing before vortex bursting.

Vorticity Contours

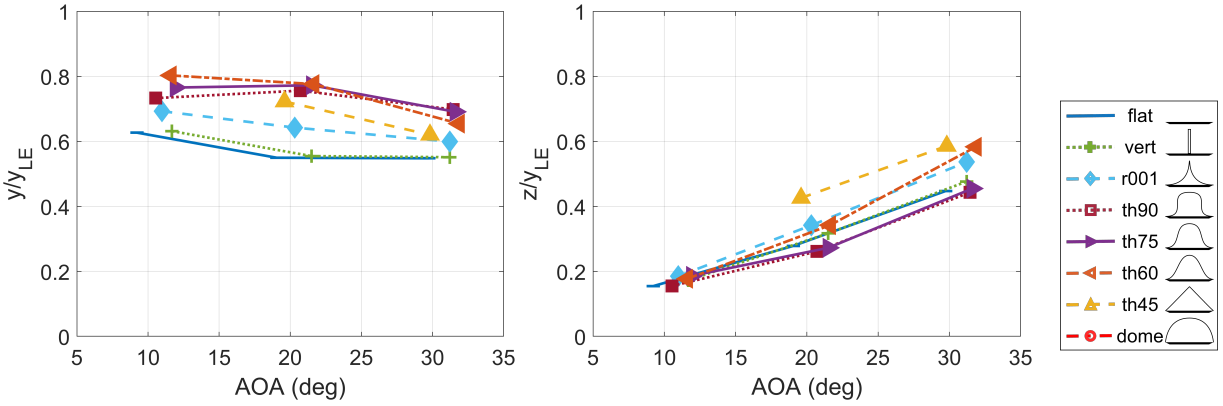

(a) top view (b) side view

Figure 5.4 Change in location of LEV with AOA relative to leading edge in spanwise (a) and normal to leading edge plane (b) directions.

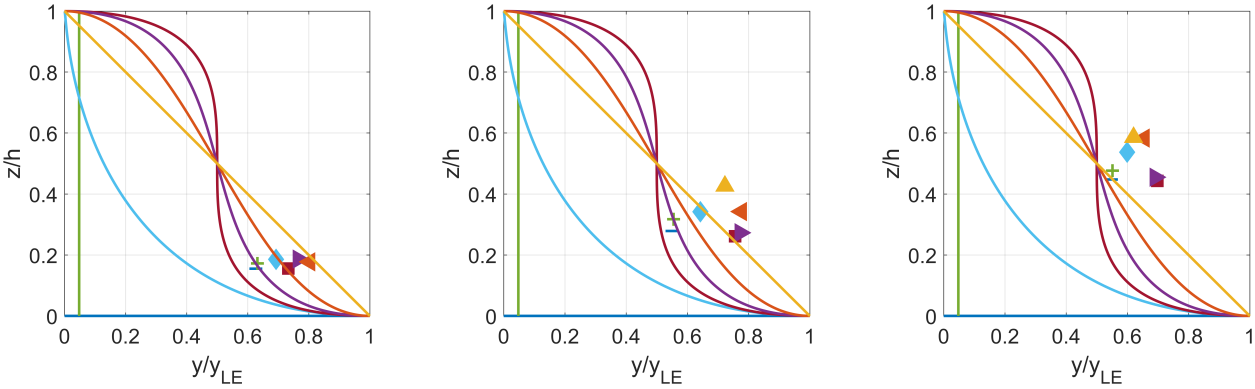

(a) AOA=10° (b) AOA=20° (c) AOA=30°

Figure 5.5 Position of LEV in cross section of various delta wing models. The port half of each model's cross-section profile is represented by a solid curve, with the LEV for that model marked in the same color. LEV position is plotted at AOA 10°, 20°, and 30° for all wings, except th45 which has no visible LEV at 10°, and the dome model.

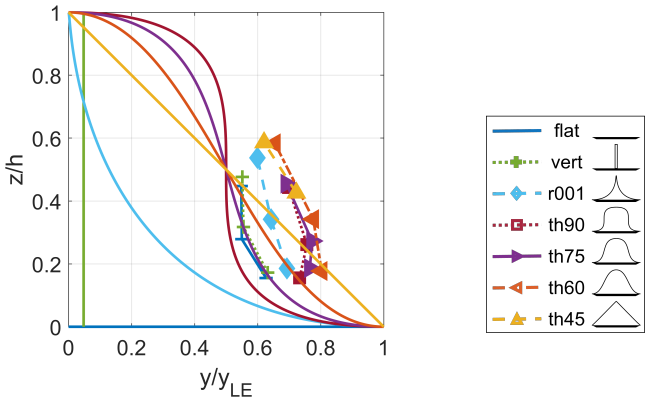

(a)

Figure 5.6 Position of LEV in cross section of various delta wing models at AOA 10°, 20°, and 30°. LEVs generally move up and inboard with increasing AOA over a given wing.

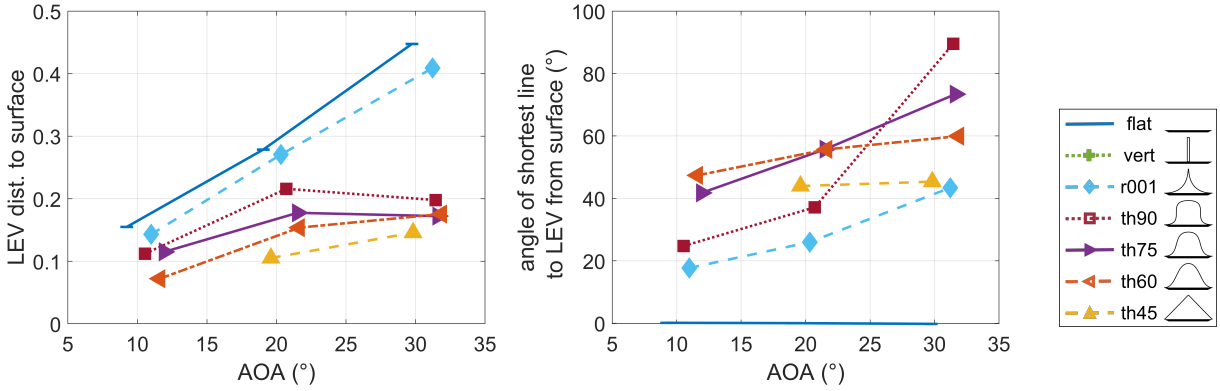

(a) (b)

Figure 5.7 Distance from LEV to wing surface (a), and angle of shortest line between wing surface and LEV referenced to vertical (b).

Figure 5.8 compares time-averaged contours of vorticity in a plane normal to the freestream for each model. Velocity vectors (downsampled by 3 for clarity) are overlaid, and the location of peak vorticity is indicated by a black x. The model surfaces were masked out before processing, so the resulting edge of the PIV results represents the cross-section shape reasonably well. All contour plots share the same colormap, which is included at the right side of the figure.

The leading edge vortex is clearly visible over all of the wings (except the dome wing) as a region of positive vorticity which originates at the leading edge (y/y_{LE}). Vorticity of opposite sign can be seen on the leeward surface of the models due to the boundary layer flow induced by the LEV. Concentrations of this negative vorticity are visible between the LEV and leading edge on most models as well. This matches the classical expectation of secondary vortices caused by ordinary

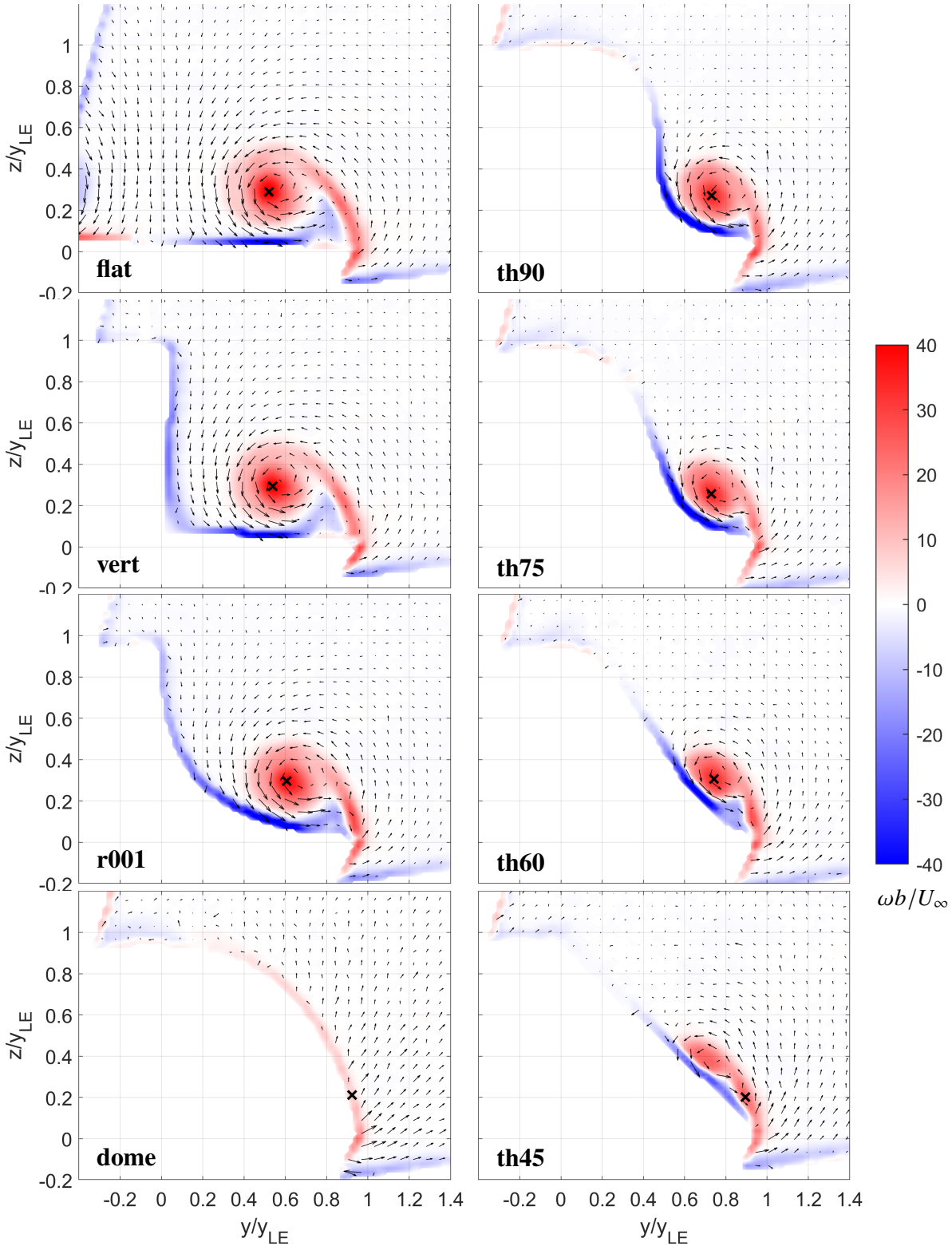

Figure 5.8 Vorticity contour plots for all wings at AOA 20°, Re 15,500. Black arrows indicate in-plane velocity. Peak vorticity location marked with black x.

separation of the induced flow boundary layer, although dye flow measurements detailed in 5.1 indicated that secondary vortices on all models (with the possible exception of r001) are either nonexistent, or have already burst upstream of this x/c=0.5 cross-section.

As the model surface is brought closer to the location where the LEV resides over the thin wing, the LEV becomes smaller and less circular. For the family of wings with equal cross-section shown in the righthand column the round region concentrated vorticity that exists at th90 warps monotonically from round to a thin higher aspect ratio smear close to the wing surface at th45. In the extreme case of the dome model, the LEV appears to be suppressed entirely.

The th45 model has a region of positive vorticity which is elevated off the model surface, but is no longer obviously distinct from the leading edge shear layer. Two peaks of vorticity exist over this model, one near the top of the region, and one about halfway up from the leading edge. These two peaks have magnitudes within 1.5% of each other. A similar second peak is visible on the th60 model, but in that case has an 18% lower value than the primary peak.

Out-of-plane Velocity Contours

Another set of contour plots in Figure 5.9 show the velocity in the freestream direction normal to the measurement plane normalized by the freestream velocity. For the flat plate model, a region of higher velocity exists is coincident to the LEV (jet-like profile). Following a similar trend to the size and symmetry of the LEV, this region disappears as the surface is expanded outward. Velocity deficits and even reversal are observed on the flat and vert wings between the LEV and leading edge (wake-like profile) where a secondary vortex might be expected to reside. This is consistent with the dye visualization in Figures 5.1, 5.2 which indicated that both these models have a secondary vortex which bursts upstream of the measurement plane.

Profiles Through LEV

Profiles of several parameters are plotted along a horizontal line through the location of maximum vorticity ($z = z_{LEV}$) in Figures 5.10. The left hand column gives profiles in horizontal positions relative to the wing, and the right hand profiles have all the profiles shifted to align the location of the LEV at $(y - y_{LEV})/y_{LE}$=0. An axial velocity surplus occurs near the LEV location, and the flat and vert models again show a deficit related to the secondary vortex (Figures 5.10a and 5.10b). The out of plane velocity converges to match the freestream velocity near the leading edge for all models.

Figures 5.10c and 5.10d give similar profiles for the vertical velocity (U_z) along the same horizontal line. On this particular line through the center of the LEV, U_z represents the azimuthal velocity

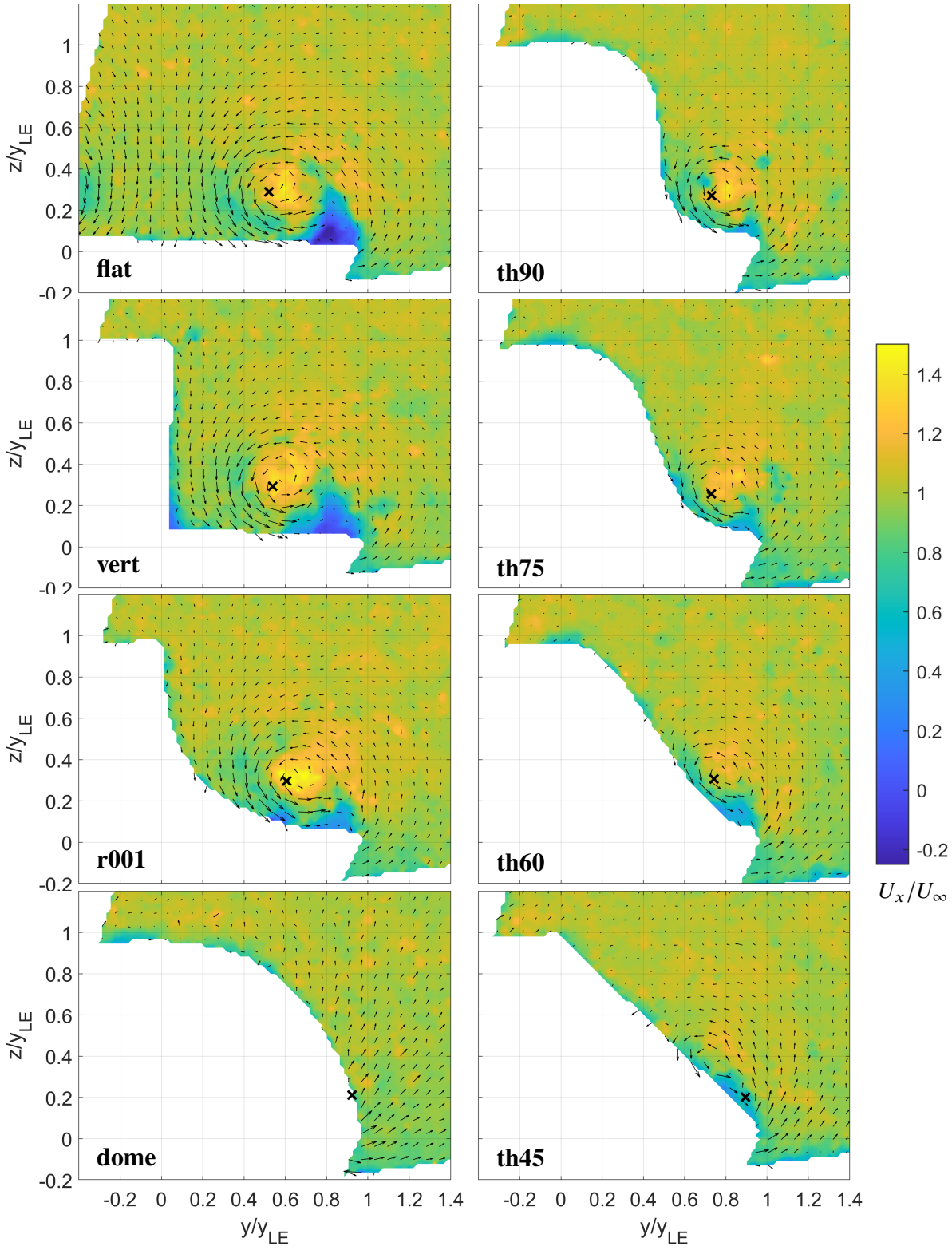

Figure 5.9 Contour plots of out-of-plane velocity for all wings at AOA 20°, Re 15,500. Black arrows indicate in-plane velocity. Peak vorticity location marked with black x.

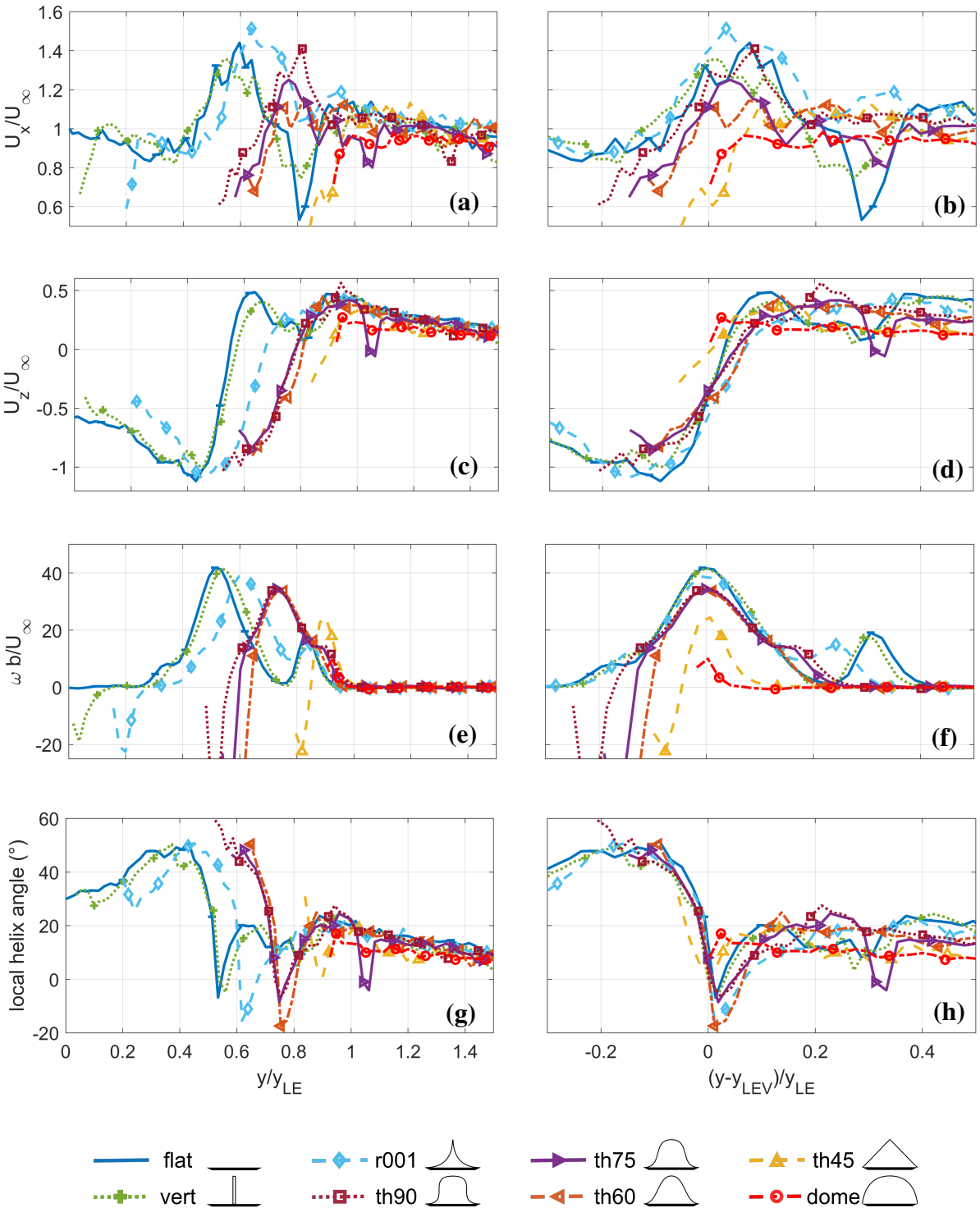

Figure 5.10 Profiles of out-of-plane velocity, vertical velocity and local helix angle along a horizontal line through the LEV center. Right hand plots show the same data as the left but with horizontal distance referenced to the LEV location.

about the vortex. Qualitatively, the profiles resemble the classic Burgers vortex with a shear through the LEV center, peak and then decay to zero far from the vortex. The vertical velocity associated with the leading edge shear layer at $y/y_{LE} = 1$ is approximately the same for all models.

The same patterns are evident in the vorticity profiles in Figures 5.10e and 5.10f. The flatter wings have two distinct vorticity peaks: the LEV and the leading edge shear layer. The leading edge vortex is constrained by the model surface on one hand, and the leading edge on the other. As the model surface moves outboard in the vicinity of the LEV, the LEV begins merge with the leading edge shear layer. This entails a reduction in the slope of the azimuthal velocity corresponding with a drop in peak vorticity.

Interestingly, the local helix angle (defined as $tan(U_z/U_\infty)$) reaches the same peak around 50° for all models except th45 and dome as shown in Figures 5.10g and 5.10h. This peak occurs at the same distance away from the LEV on all models: around $y/y_{LE} = 0.4$ for the three flattest models and closer to $y/y_{LE} = 0.6$ for th90, th75 and th60.

Effect of Vortex Confinement

In all cases, the top of the LEV reaches to about z/y_LE=0.5. This motivates the definition of a vortex confinement parameter, κ, as the ratio of the model cross-sectional area in the bottom half of the cross section (z/yLE<0.5) to the bounding rectangle with area $y_{LE}^2/2$ (Figure 5.11). The total circulation in the LEV and other important parameters are well correlated with this parameter (Figure 5.12). As expected from the previous discussion, circulation in the LEV is negatively correlated with vortex confinement. The same is true for out-of-plane velocity through the LEV core. These two effects balance each other such that the max helix angle is relatively constant across geometries, with the exception of the th45 and dome wings in which no single LEV was detected. The diffusive vorticity flux also appears to be constant as vortex confinement is increased from the flat wing to the th90 wing, then increasing approximately linearly with $\kappa > 0.6$. The dome wing dissipative vorticity flux is suspect because of the proximity of the vorticity gradient to the model surface. Unfortunately the SPIV data do not have sufficient resolution to accurately resolve convective vorticity fluxes through the LE shear layer.

5.3 Force Results

Force measurements for four of the delta wing models are presented in Figure 5.13. For reference, the Polhamus leading edge suction analogy prediction for total and potential lift are also plotted on the lift, drag, and normal coefficient plots (Polhamus, 1966). Lift measurements over a flat 70° delta at a similar Reynolds number of 20000 by Traub (Traub, Moeller, and Rediniotis, 1998) are

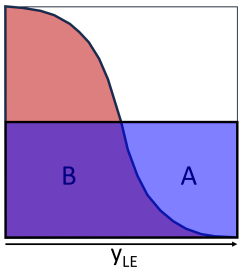

Figure 5.11 Confinement area κ is defined as the ratio of the area below $z/y_L E$=0.5 which is occupied by the model on one half of the cross-section, B/A.

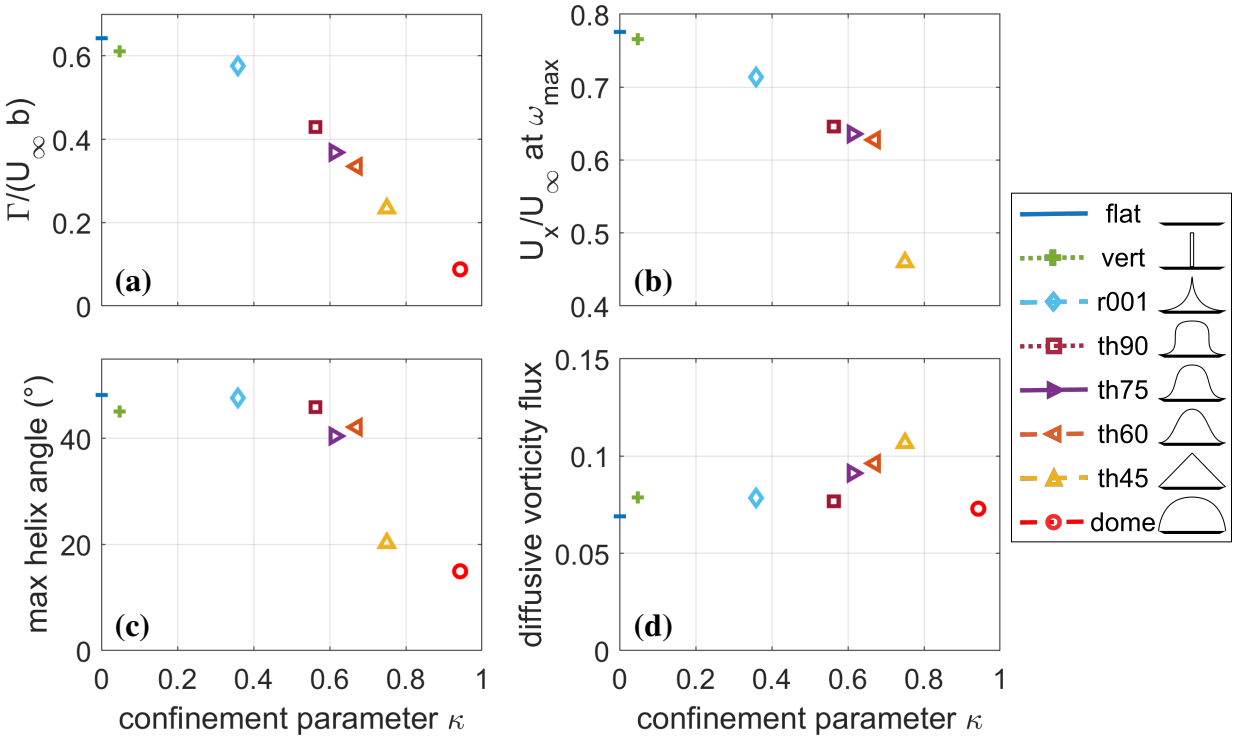

Figure 5.12 LEV circulation (a), axial velocity at location of peak vorticity (b), maximum helix angle (c), and diffusive vorticity flux (d) along a horizontal line from LEV plotted as a function of LEV confinement parameter κ.

plotted as well. The Reynolds number for the current measurements was 16,200.

The lift measurement compares well with Traub's 1998 measurement for the flat wing. Traub's model was 1.3% thick with square edges, so difference in total lift could be related to the difference in leading edge shape. Traub also did not report a freestream turbulence level, which could be relevant at such low Reynolds numbers. The forces on the flat wing are generally well described as a pure normal force with a tangential component near zero across all angles of attack. As expected at a low Reynolds number, the lift, drag, and normal force of the flat plate model lies between the Polhamus total lift and potential lift estimate. The Polhamus model does not include viscous effects or vortex bursting, and so cannot capture the stall process. Interestingly, the normal force of the th45 triangular cross-section model matches the Polhamus potential force prediction quite well, particularly above 15° AOA, which is consistent with that wing having very little vortex lift.

Below 15° AOA, the th45, th60, and th90 wings have a lower normal force and lift curve slopes compared to the flat model. However, above 15° the th90 model recovers to match the force of the flat wing. Beyond 25°, the normal force of the th90 wing plateaus until sharply increasing again above 35° to match the flat wing force at 45°. The normal force on the th60 model lies between that of the th45 and th90 wings, so these wings define a continuum aerodynamically as well as geometrically.

The relationship between each wing's lift and drag highlights the differences between the models. The three thick models have identical lift-drag curves until C_D=0.5, where the th90 and th60 wings experience a reduction in lift for a given amount of drag compared to the th45 wing. At AOA 45° all the tested wings have nearly identical lift and drag coefficients, despite the wide variation among the models at lower angles of attack.

The tangential force on all the thick wings is higher than that of the flat wing at low angles of attack. At around 20° however, the tangential force of all the thick wings enters into a downward trend, eventually dropping lower than the flat wing, and even slightly negative as the angle of attack increases.

The relatively large error bars on the moment data points reflect the fact that this moment is both near the noise floor of the load cell, and similar in magnitude to the moments created by the off-axis loading of the load cell, and the moment due to the sting arm. This measurement could be contaminated if any of these sources have errors. The flat wing does not exhibit the characteristic pitch-up expected near stall, which could be a good reason to be skeptical of these values. However, the differences between the models show that the thicker models have a consistently more negative (nose down) pitching moment compared to the flat wing. These thicker models also all have a rapid

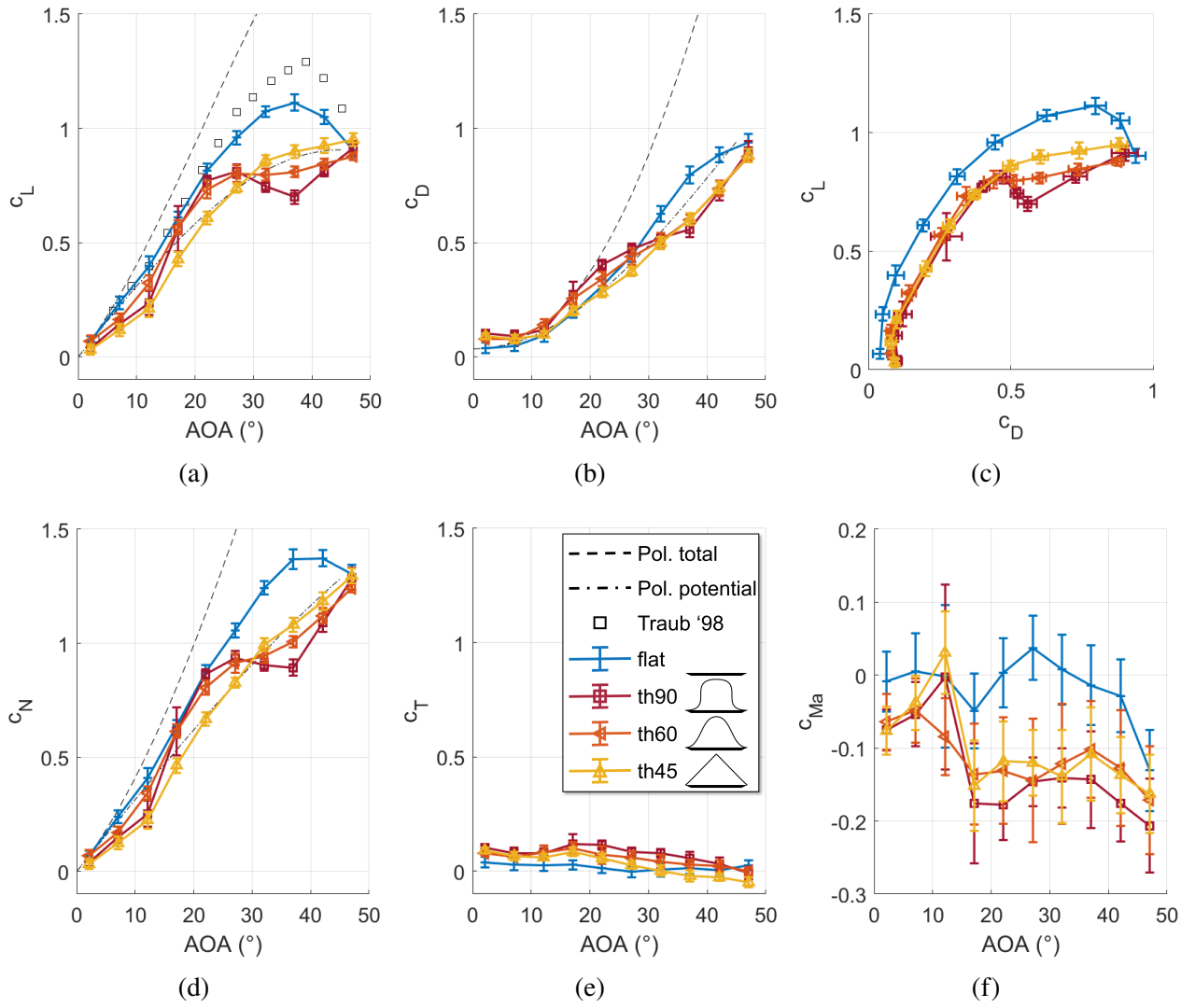

Figure 5.13 Delta wing force measurements.

shift in the pitching moment around 15°, the same angle of attack that shows a rapid increase in the normal force.

5.4 Tomographic Dye Visualization

The three-dimensional flow field of the same three wings is presented in Figures 5.14 through 5.25 as embedded animations. Each animation begins looking at the models from the back and rotates around 110° to see the port side. These animations may only play in Adobe Acrobat. Alternate versions are provided separately as supplementary material. Figures 5.26 and 5.27 show cross-sections of the same four models and angles of attack at $x/c = 0.4$ and $x/c = 0.97$, respectively.

Single slices of each wing cross section are provided for each wing in the apex region at $x/c = 0.4$ (Figure 5.26) and near the trailing edge at $x/c = 0.97$ (Figure 5.27).

Anything bright in the 2D images is rendered visible. This includes the model surface, the injection tubes, and the fluorescent dye. The black and white lookup table is inverted for presentation. The stainless steel dye tube is particularly reflective, which caused an artifact near the trailing edge of the model that looks like a straight line intersecting the tube. There is also some blooming near the brightest locations where dye is injected. As the scans were acquired, dye injection from the apex was reduced in favor of the aft dye tube. This causes the LEV to appear thinner approaching the trailing edge in some cases. A single hot pixel on the camera present in every slice produced a horizontal line through each scan, which is aligned with the scanning direction (freestream). The laser sheet was incident from the top of the wing, so vertical surfaces (particularly on the th90 wing) are less visible. The windward and starboard portions of the wing are not pictured.

Over the flat wing both a primary and secondary vortex are visible at all angles of attack. Dye injected off-axis into a vortex creates a spiral pattern. This is particularly evident over the flat wing at 35°. At 10° and 20° angle of attack the secondary vortex bursts and the dye it contains is entrained into spirals around the primary LEV. Bursting of the primary LEV is obvious at 35°. No dye was injected through the aft tube for the flat wing.

At AOA 10°, the thicker models all appear to exhibit a laminar separation from the central bump. Dye from the aft injection tube is drawn forward by reversed flow along the model's rear surface and swept into a shear layer formed by laminar separation just aft of the model peak. Between this shear layer is a region that is filled with well-mixed diffuse dye, which is at too low of a concentration to be seen in the volume renders without compromising details elsewhere on the model. This region of separated flow is particularly clear in the cross-sections shown in Figure 5.27. As seen previously, no LEV is seen on the th45 wing at 10°. Instead, the apex dye on the th45 model remains attached to the model surface until it too separates near the aft of the model.

As the model angle of attack increases to 20° the flow pattern on the aft of the body changes significantly. Most clearly on the th90 wing, the dye from the injection tube fills a thin region of fluid near the body with clearly defined boundaries at the upstream and downstream edges. Near the corner of the bump, the dye is swept into a helical pattern which is elevated somewhat over the wing surface. No dye is seen inboard of this helical pattern, despite the injection location being on the centerline of the model just upstream. These aft vortices are also visible in the 2D dye visualizations when the dye was injected before an impulsive start of the tunnel (Figure 5.3).

At AOA 35° it is difficult to identify any structure in the flow field aft of the body. Dye from the

burst leading edge vortices tends to remain in a diffuse roughly conical region. Adjacent slices aft of the model body do not appear related, which indicates that the flow field in that region is not stationary in time. Both the th60 and th45 models exhibit more than one vortex emanating from the apex at 35°. Over the th60 wing, two vortices rotate in opposite directions, with the top vortex being the primary LEV and the bottom rotating in the direction of a secondary vortex. On the th45 wing, three vortices can be seen near the apex which have alternating signs (Figure 5.26).

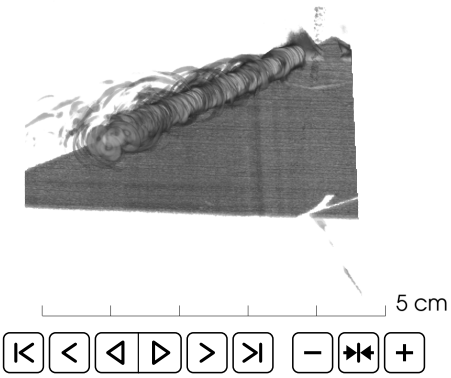

Figure 5.14 flat wing at 10°

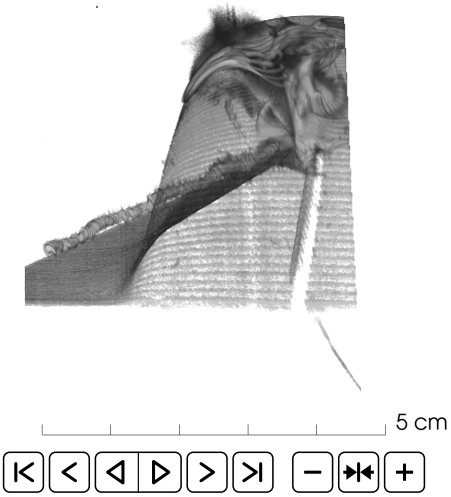

Figure 5.15 th90 wing at 10°

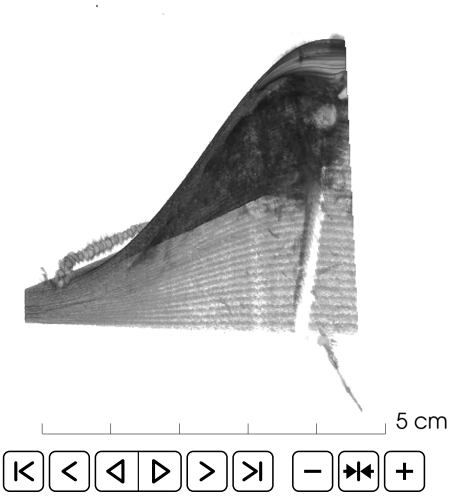

Figure 5.16 th60 wing at 10°

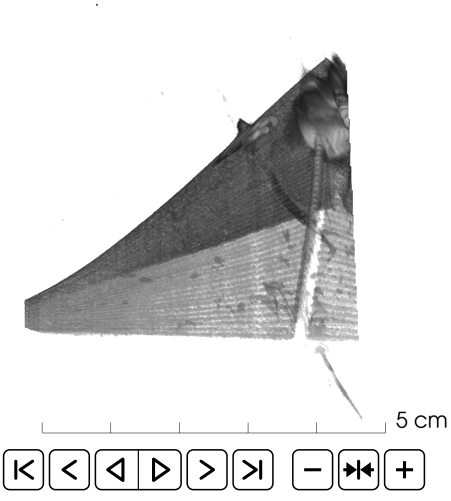

Figure 5.17 th45 wing at 10°

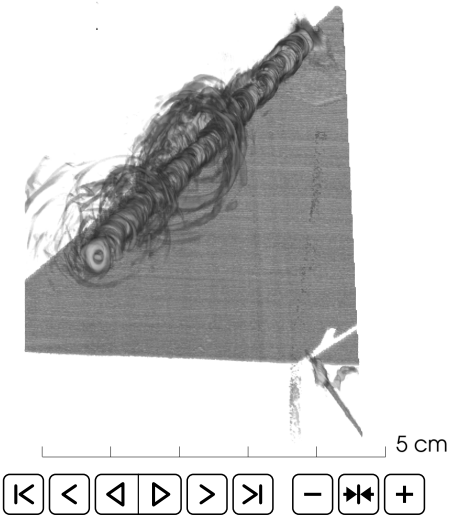

Figure 5.18 flat wing at 20°

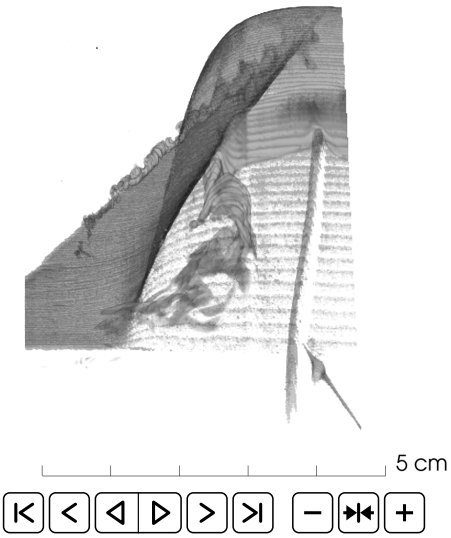

Figure 5.19 th90 wing at 20°

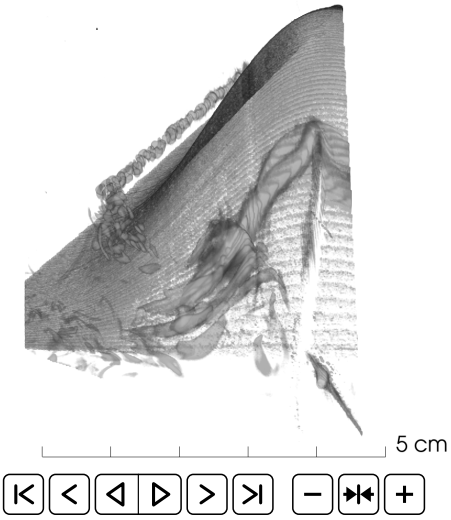

Figure 5.20 th60 wing at 20°

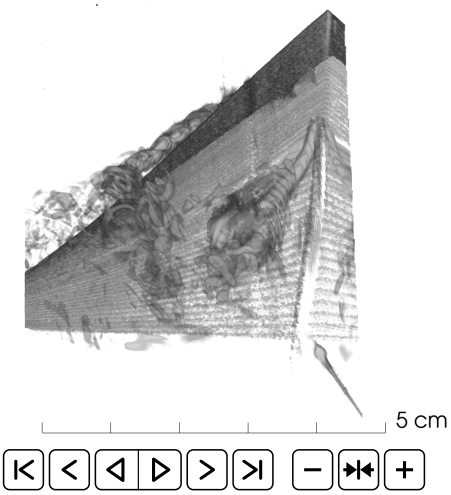

Figure 5.21 th45 wing at 20°

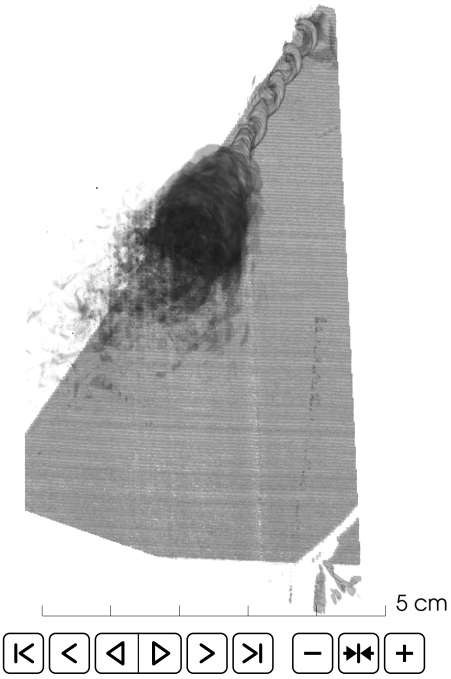

Figure 5.22 flat wing at 35°

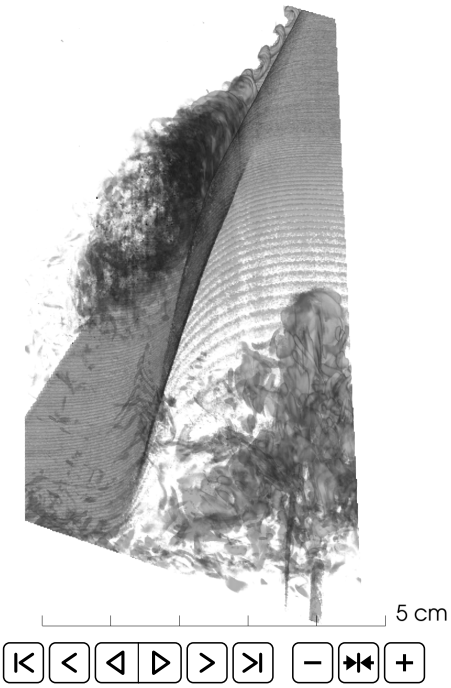

Figure 5.23 th90 wing at 35°

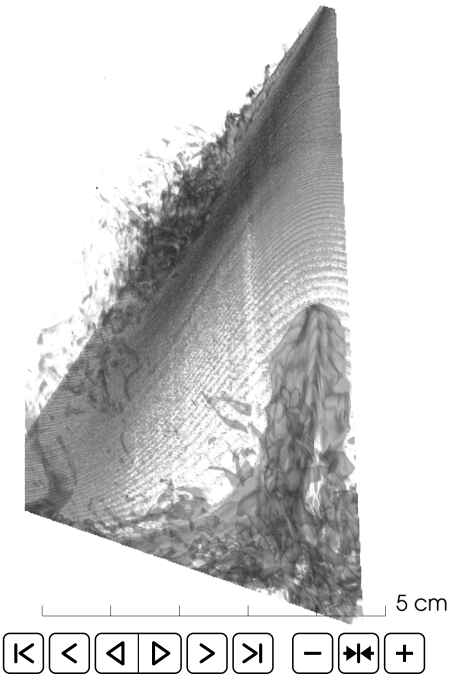

Figure 5.24 th60 wing at 35°

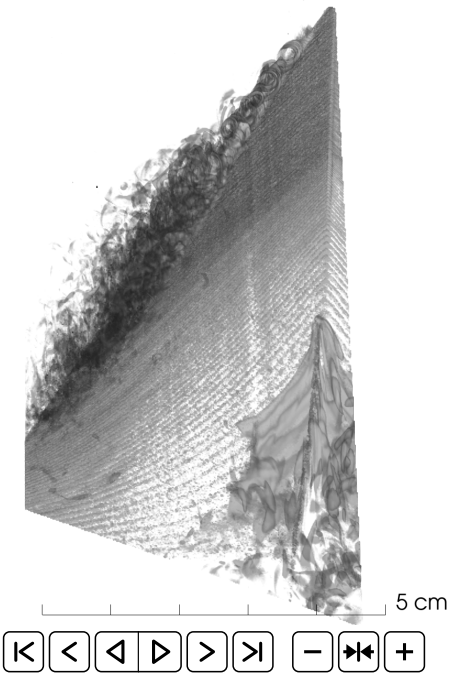

Figure 5.25 th45 wing at 35°

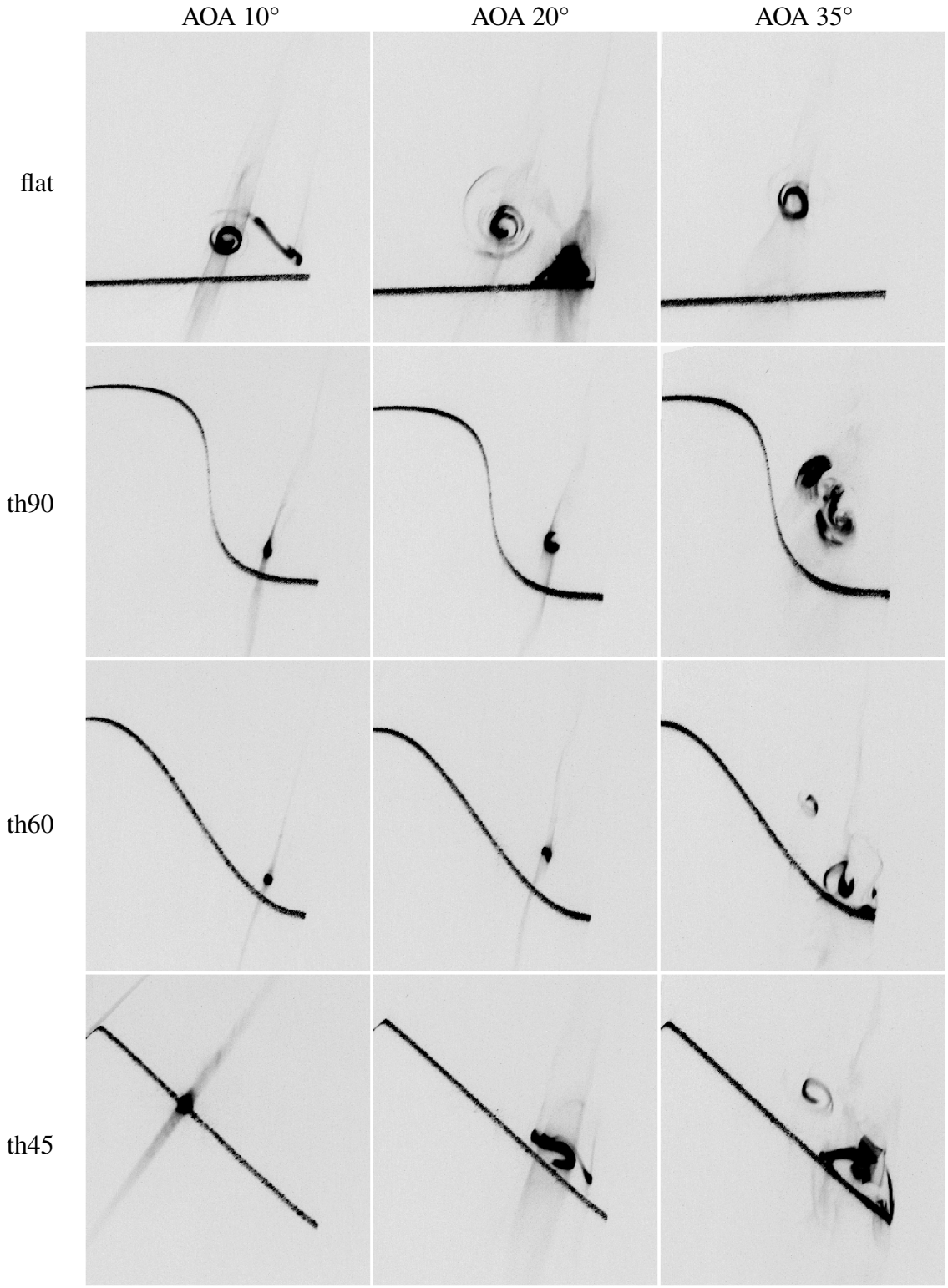

Figure 5.26 Cross-sectional dye visualizations of flat, th90, th60 and th45 wings at AOA 10°, 20°, and 35°, $x/c = 0.4$.

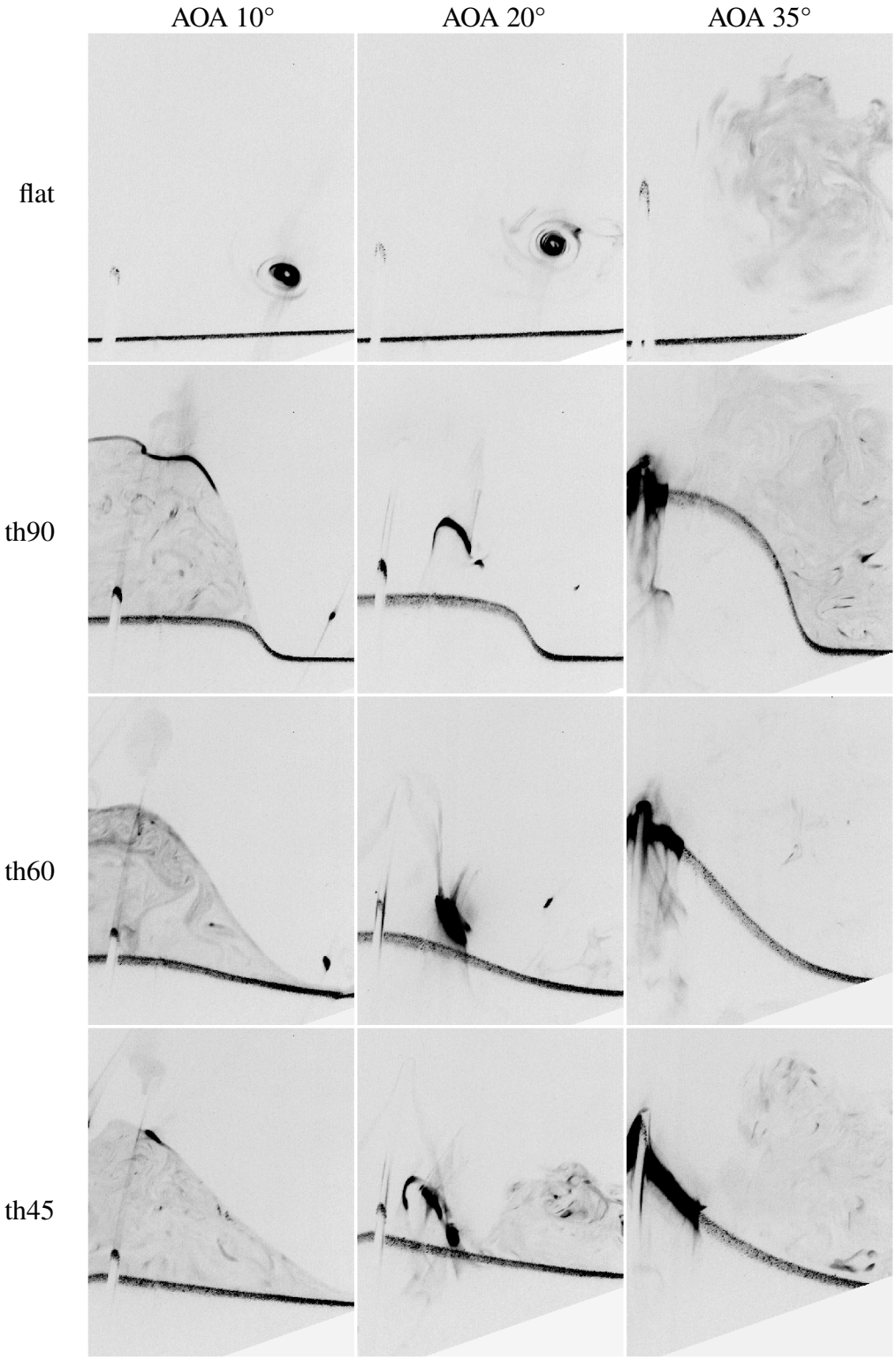

Figure 5.27 Cross-sectional dye visualizations of flat, th90, th60 and th45 wings at AOA 10°, 20°, and 35°, $x/c = 0.97$.

DISCUSSION AND CONCLUSION

The results presented above demonstrate that many differences exist in the flow field and performance of thick delta wings compared to a flat wing. The following discussion explores the mechanisms behind the observed phenomena and offers suggestions for future research directions.

6.1 LEV location and strength

The dye visualization results showed that the location and linearity of the LEV can be significantly altered by introducing a surface proximal to the LEV. Because the LEV has a finite size, it cannot maintain its position as the wing surface begins to encroach upon the space that the LEV would otherwise occupy. Generally, the LEV over a contoured wing appears to move in a direction normal to the local wing surface relative to the flat wing. This suggests that LEV moves to the position closest to the location it would take were the surface absent (over a flat wing) while maintaining some distance determined by the balance of vorticity, convection, and viscous effects.

In addition, the SPIV study demonstrates that the LEV circulation is inversely proportional to the confinement of the vortex after about $\kappa = 0.3$. From the flat wing vorticity contour plot in figure 5.8, the inboard edge of the LEV is at about $y/y_{LE} = 0.25$. A value of $\kappa = 0.3$ corresponds to a model which occupies an area equal to the inner $y/y_{LE} = 0.3$ of the cross section up to a height of $z/y_{LE} = 0.5$. Therefore it appears that the LEV strength does not change until the model surface begins to impinge on the space that it would otherwise occupy. A similar trend seems to exist with the diffusive vorticity flux, which begins to explain what happens to the vorticity generated at the leading edge. It appears that after some confinement threshold the leading edge vorticity begins to annihilate with the opposite sign vorticity from the leeward wing surface at a greater rate, rather than contributing to LEV circulation. It is curious to note that the LEV circulation begins to tail off at a lower confinement value ($\kappa = 0.3$) than the dissipative vorticity flux begins to increase ($\kappa = 0.6$). This difference could suggest that there are other mechanisms at play, like a change in the convective vorticity flux from the LE shear layer, or could be measurement error resulting from insufficient resolution near the wing surface.

In the limiting case of the dome wing, no LEV is observed. All of the wings save for the th45 and dome have the same leading edge and leeward surface geometry, so they might be expected to generate similar amounts of vorticity at their leading edges. Unfortunately the SPIV measurements

did not have sufficient resolution to accurately resolve the convective vorticity flux through the leading edge shear layer, but the vertical velocity profiles in Figure 5.10c indicate similar velocity in the shear layer for each wing. The vorticity contour plots indicate that essentially the entire leading edge shear layer is entrained into the LEV in all cases. If all LEVs have the same vorticity flux from the leading edge shear layer then the cases with less total LEV circulation must lose vorticity either out-of-plane or to annihilation with the viscous boundary layer on the model surface. The out-of-plane velocity contours in figure 5.9 and 5.10a show that the wings with high vortex confinement actually have lower out-of-plane velocity at the vortex core, supporting the latter explanation.

While all of the other wings have the same windward surface geometry, the th45 and dome wings have a higher tangent angle where the leeward surface meets the leading edge. This may effect the way that the flow separates from the leading edge, adding an additional effect beyond that of vortex confinement. In fact the vorticity contours for the dome model indicate positive vorticity near the model surface above the leading edge, indicating that the flow in this location is attached. Despite this difference in leading edge geometry, all the tested wings lie along the same curve of vortex confinement versus total circulation, indicating some universality to this parameter. Without flow separation at the leading edge it is not possible to form a leading edge vortex in the first place.

Thus the condition of vortex suppression can be achieved either by confinement, or by delaying separation at the leading edge by increasing the radius. Both of these mechanisms are likely active. Of course rounding the leading edge can only delay separation, not eliminate it altogether, so we might expect to still observe a vortex on the dome model, just higher up than before. However, the centerline profile of all the wings is inclined at 20° to the chord, so at 20° angle of attack the peak of the wing is aligned with the freestream. This means that the flow over the dome model does not experience an adverse pressure gradient until its cross-sectional area begins to decrease in the aft section. Therefore we should not expect to see separation anywhere on the apex of the model if it does not occur at the leading edge.

6.2 LEV Shape and Dual-Vortex Structure

As the wing surface moves outward, the shape of the LEV also elongates from a round shape to something more like an ellipse with its long axis parallel to the local surface direction. In the case of the th45 wing, the surface is close enough to the LEV that it splits into two distinct concentrations of vorticity, and is less obviously distinct from the leading edge shear layer. It is unclear how common this dual vortex structure might be, but it was observed for the th45 wing over a fairly wide range of angles of attack of 20° through 35°. At 20° the dual vortex structure

is not visible in the 2D dye visualization data, but is clear in the tomographic dye scan and SPIV. This could easily be due to subtle differences in the dye entrainment caused by something like a small air bubble reducing flow on one side of the model, or could indicate that the appearance of this configuration is incredibly sensitive to small changes in flow condition. This structure was not observed by Grellman Grellmann, 1964 in studies of slender delta wings with triangular cross-sections, or Kirkpatrick D. L. I. Kirkpatrick and Field, 1966 over rhombic cross-sections, but both these studies involved only low angles of attack (<20°), high Reynolds numbers (>10^6), and used low resolution measurement techniques (surface pressure taps, keil probe) that may not find two vortices if only one is expected.

The rotation of a vortex tube generally tends to stabilize the vortex into a circular shape without the influence of a nearby surface. Any local increase in the vortex radius generates a restoring Coriolis force depending on the the Rossby number of the flow (Batchelor, 2000). Thus the elongation of vortices as they are confined by the model surface is eventually untenable, forcing the vortex to split into more than one distinct vortex, each with a smaller radius and more circular shape. Perhaps this process can also be related to the break up of a shear layer due to the Kelvin-Helmholtz instability. The split vortices are observed to be stationary, a condition that can also be seen on sub-vortices formed by the Kelvin-Helmholtz instability around the LEVs on thin slender delta wings Gad-el-Hak and Blackwelder, 1985; Ismet Gursul, 2005.

A dual-primary vortex structure is also observed on low-sweep 50° delta wings at low angles of attack (Taylor, Schnorbus, and Ismet Gursul, 2003). This is understood to be due to the strong interaction of the LEV with the wing boundary layer owing to the low height of the LEV above the wing surface. As the angle of attack increases, the LEV lifts away from the surface and the dual primary structure reverts to a single LEV. In the current case, the dual vortex structure appears on the th45 model somewhere between 10° and 20° AOA and persists all the way up to at least 35°. The height of the wing surface is such that the distance between the LEV and the surface is only marginally increased with angle of attack, but the vortex also gains vorticity due to an increase in the flow component normal to the leading edge. For the low sweep delta wings the appearance of a dual-primary structure was found to be highly Reynolds number dependent because it depends on the condition of the leeward surface boundary layer. A similar Reynolds number dependence is to be expected in the current case.

A dual-primary LEV vortex structure has also been observed over rotating wings in experiments meant to emulate insect wings (Lu, Shen, and Lai, 2006). A similar phenomenon is observed in DNS simulations of the starting LEV over a rotating flat plate (Sader et al., 2024). Experiments

and simulations over a blunt edged 65° sweep delta wing for the Second International Vortex Flow Experiment (VFE-2) found co-rotating inner and outer primary vortices, but these appear to be formed by a different mechanism, with the additional vortex forming farther inboard rather than outboard, and not following a conical trajectory emanating from the wing apex (Luckring and Dietrich Hummel, 2013).

It is possible to imagine the leading edge shear layer splitting into more than two primary vortices, though this has not yet been observed to the knowledge of the author. The tomographic dye scan of the th45 wing at 35° provides evidence of a third vortex with negative sign in between the two positive sense primaries. This can perhaps be understood as a secondary vortex in the classic delta wing sense, being the result of ordinary separation from the leeward surface of the spanwise flow induced by the primaries.

It may be that this secondary vortex acts to split the leading edge shear layer, forcing the creation of a pair of co-rotating LEVs rather than one vortex. This could also help to explain why the dual-primary structure only appears to occur when the LEV is close to the wing surface. Shih and Ding (1996) documented such an interaction creating unsteady shedding in the leading edge shear layer over a 75° delta wing at Re 9,000. It remains unclear exactly what conditions are necessary for this shedding to become steady to form two stable LEVs, but from the low-sweep delta results it is clear that Reynolds number and surface proximity are important parameters.

6.3 Aft Section Flow Field

The flow field at the back of the delta wings is found to be highly dependent on model geometry and angle of attack. The th90 wing produces three different flow fields at the three angles of attack that were imaged using the tomographic dye technique. At both 10° and 35° a large separated wake is produced behind the wing's central bump, but at the intermediate 20° angle of attack the wake is considerably smaller. This appears to be because of the formation of a pair of streamwise vortices at 20°, which separate off the corners of the centerbody and induce a downwards flow over the center aft portion of the wing. At 10° the flow separation off of the model appears to be laminar, with a very smooth and stationary shear layer seen in the dye images. At 35° the separation appears more turbulent. It is likely that results could vary with Reynolds number related to the condition of the attached flow on the model upstream of the aft separation point.

As it happens, similar critical geometries in which a critical sweepback angle causes a dramatic change in the flow configuration have been well documented in the literature. Morel (1978) first reported on the flow over the rear window of hatchback cars. He found that as the angle of the

sweepback is increased, a pair of counter-rotating vortices roll up around the corners of the swept rear. These vortices induce a downwards flow which causes the previously detached inboard flow to reattach to the body. The net effect is a sudden and dramatic increase in lift and drag. Then as the sweepback angle is increased even farther, the vortices give way to a fully separated flow Sovran, Morel, and Mason, 1978. Subsequent studies have largely confirmed that a similar flow field exists over similar geometries Ahmed, 1983; Zigunov, Sellappan, and Alvi, 2020. This description matches the observed flow field over the back of the th90 wing quite well. Differences in the direction of the incident flow induced by the action of the delta wing's LEVs appear to change the critical angle at which the phenomenon is observed.

Both the th45 and th60 wings have evidence of the same sort of flow separation patterns off the back end, but as the surface tangent slope is reduced from 90° down to 45° the aft region curvature decreases, and streamlines face a more mild adverse pressure gradient. The corners of the aft region from which the pair of counter rotating vortices separates in the th60 and th45 cases have a much larger radius in the streamwise direction (figure 4.4, 4.6), so flow from outboard portions of the wing is able to travel farther inboard before separating from the surface.

6.4 Wing Forces

All of these flow field features combine to produce the force plots in figure 5.13. While the flat wing has the classic delta wing behavior, the th45 wing has a reduced lift curve slope, looking similar to the Polhamus estimate for potential flow about a thin wing in the absence of vortex lift (Polhamus, 1966). All the thick models have increased profile drag compared to the flat wing. This is consistent with observations by Grellman that taller triangular cross-sections have reduced normal force and increased drag (Grellmann, 1964). Increased profile drag is to be expected due to the increased cross-sectional area.

The angle of the wing surface near the LEV also has implications for the wing forces. Following the reasoning of G. Lee, 1959, integrating the pressure field over an inclined surface can alter the direction of the resulting force vector. In the case of extreme leeward surfaces considered here this is necessarily a coupled problem, with the surface shape affecting both the pressure field and the integrated force direction. From Figure 5.7b, it might be expected that the th90 wing at AOA 30° would have a lower normal and tangential force than the other wings with the same cross-sectional area because the LEV suction force might be inclined forward due to the wing surface shape. This intuition seems to be borne out by experiments, with the th90 wing having the lowest normal force at 30°, though the tangential force remains high. However, the wings are not conical, so it is difficult to separate this effect from that of the aft flow field.

On the th90 wing, the criticality of the aft wing flow field creates a highly non-linear force profile. When the aft flow is separated at 10° and at 35°, the th90 wing generates significantly less normal force than the flat wing. At 20°, when the flow is attached, the normal force of the flat wing is almost entirely recovered. This is despite the fact that the LEV over th90 wing has about 30% less circulation than the flat wing at 20°. The pair of counter-rotating vortices that form over the aft section appear to make up for the reduction in LEV lift.

The normal force of the th90 wing then decreases with angle of attack from 20° to 35°, where it begins increasing again to match the forces from the flat and th45 wings at 45°. At 45° the flow over the model should be fully separated regardless of the leeward surface geometry, so the normal force is almost entirely determined by the wing planform, which is identical for all the models.

The shape of the th90 normal force curve at high angles of attack is somewhat reminiscent of the normal force curves of low sweep delta wings presented by Earnshaw and Lawford (1964). In their study, a similar stagnation and temporary reduction of normal force was found to be related to the transition of the flow field from a conical configuration with attached flow at the center, to a completely reversed flow at the surface. Lower sweep wings were found to have entirely reversed flow from the rear of the model at lower angles of attack than wings with greater sweep. In the present case, the region of flow reversal behind the th90 wing is larger at 35° than the other wings owing to its less streamlined aft shape.

Across all angles of attack, the th60 wing achieves a normal force between that of the th90 wing and the th45 wing, demonstrating that these wings do in fact define a continuum of shapes for which the same salient flow features are relevant. It is interesting to note that while all three of these wings have the same internal volume, the th90 wing is able to generate more lift at 20° angle of attack. This appears to be explained by the retention of most of the LEV strength relative to the th45 wing.

The implication for designers hoping to create vehicles that rely on vortex lift and have large internal volumes is that stronger LEVs comparable to those over flat wings can be generated over thicker geometries, provided that there exists some concave region inboard of the leading edge for the LEV to occupy. This matches Bartol's prediction about concavities near boxfish keels Ian K. Bartol, Gharib, Webb, et al., 2005. The relationship between confinement parameter and LEV strength (Figure 5.12) suggests that vortex lift can be retained by designing a surface that does not overlap the LEV over an equivalent flat plate wing.

However, including a central bump or fuselage does come at a cost of increased profile drag related to the increased cross-sectional area, and the aft shape of the wing is non-trivial: even wings that

generate strong vortex lift can develop non-linear forces with AOA if the flow separates off the back of the central bump.

6.5 Future Directions

The experimental results presented here open up ample opportunity for further study.

One particularly pressing question is that of Reynolds number sensitivity. Ordinary separation of the leeward surface boundary layer has dramatic effects on the flow field and resulting force over the wings tested here. Interactions between the LEVs and the boundary layer in this case likely have much stronger Reynolds number dependence than canonical flat slender delta wings, which have elevated LEVs with minimal surface interaction. Separation off the back of the model and the resulting wake will also depend on Reynolds number. For instance, it is clear from the tomographic dye images that laminar separation occurs at 10°, while at 35° the separation appears more turbulent.

Tests at higher Reynolds numbers via faster flow speeds could also improve the signal-to-noise-ratio of force measurements. The pitching moment measurements in particular could stand to be improved, which would help to understand the wing stability implications of both the LEV position and strength changes, as well as the aft section separation/attachment condition. The FLOWTUB water tunnel test section is large enough to accommodate models with twice the chord length, and has been run at speeds twice as fast as the 10 cm/s used in all the tests done here, so a 4x increase in Reynolds number and 16x increase in pitching moment magnitude should be possible without dramatic changes to the force measurement setup.

Another area of interest would be to collect more SPIV data to investigate the dual primary vortex phenomenon observed over the th45 wing at high angles of attack, as well as the aft section flow field and wing wakes. In an ideal case, this could be accomplished with an extension of the tomographic dye technique to SPIV, wherein the model is traversed though a cross-sectional laser sheet to gather a series of SPIV planes. In this way, a full time-averaged 3D velocity and vorticity field could be measured. However, this technique would be of limited utility for non-stationary flow fields as it requires a steady in time assumption to correlate adjacent planes. Additional challenges related to light intensity, increased noise due to reduced-time averaging for a given slice, and large data sets might make this technique less straightforward to implement. To aid in data processing, a hardware accelerated PIV implementation like rapidPIV could be particularly useful in this case (Bollt, Foxman, and Gharib, 2025).

The results presented here are also over a very limited set of models. There is broad opportunity

to investigate the flow fields over different sets of parameters for within the same family of wing shapes. For example, how does LEV strength and location change if the tangent angle of the surface is held constant and the height or width of the central bump is increased? Does there exist a critical surface height at which the LEV ceases to shift outboard with increasing bump width and instead reattaches or appears above the bump?

The aft shapes investigated here are also arbitrary. One could imagine that a longer aft region with a lower pressure gradient should have less flow separation, which could have dramatic implications for wing performance. This warrants a broader study of airfoil shapes for delta wings with extreme thickness, where the three-dimensional complexity of the flow field will likely benefit from three-dimensional surface geometries controlled by more parameters than were presented here.

This investigation also only considered steady flows. Startup flows (like those presented in figure 5.3) likely contain interesting unsteady physics as this complicated flow field develops temporally. Some of this work is currently being conducted computationally by Caroline Cardinale under Tim Colonius, using an incompressible direct numerical simulation (DNS) code (Liska and Colonius, 2014; Liska and Colonius, 2017; Yu, Dorschner, and Colonius, 2022). Results from these simulations have largely matched up with the experimental measurements, both qualitatively showing the same flow features, and quantitatively matching lift and drag coefficients for the flat and th90 models. CFD could also could offer a way to search a wider parameter space than is feasible with physical models.

There are also many opportunities to develop and compare to existing analytical theories for conical and non-conical wings. The wing surface being closer to the LEV also suggests flow control possibilities like axial blowing.

6.6 Conclusion

Part II of this thesis provided a further demonstration of the utility of the compact tunnel developed in part I. A series of delta wing shapes with large thickness to chord ratios were placed in the tunnel and the resulting flow field was probed with a combination of dye visualizations, SPIV, and force measurements. These investigations yielded a number of preliminary conclusions listed below.

First, confining the leading-edge vortex (LEV) by raising the height of the leeward surface of a delta wing was found to alter both the location and shape of the LEV. As the surface is brought closer to the LEV, the total circulation in the LEV is reduced until the LEV is entirely suppressed. When the LEV, it can split into a pair of co-rotating primary vortices - a phenomenon that, to the author's knowledge, has not been reported on thick delta wings with high wing sweep.

Wings with increased cross-sectional area tend to show degraded aerodynamic performance. This is primarily due to increased profile drag and reduced normal force at a given angle of attack. However, wings with identical cross-sectional area can have drastically different flow fields and force curves depending on the spanwise thickness distribution.

It is possible to retain most of the strength of the LEV even for large wing cross-sections by biasing thickness away from the leading edge, thereby minimizing the extent of vortex confinement. In doing so, it is possible to achieve comparable vortex lift to that of a flat wing with a much greater internal volume, although the longitudinal profile is also important for determining flight performance across angles of attack. The impact of confinement on LEV bursting appeared minimal.

Finally it was observed that the aft section of a thick delta wing can develop its own set of counter-rotating vortices, resembling the vortices seen behind slanted conical bases or Ahmed bodies. These rear vortices can contribute to non-linear force responses with respect to angle of attack, depending on the specific wing geometry and curvature.

These conclusions are specific to the shapes and Reynolds numbers (approximately 10^4) studied here, and further investigation is required to determine their broader generality. An additional outcome of this work is the first demonstration of the tomographic dye visualization technique for generating 3D images of wings and thier flow fields with a moving model and stationary optical system. This work opens several avenues for future research, including numerical modeling, Reynolds number sensitivity studies, and exploration of a wider variety of wing geometries.

Ahmed, S. R. (Dec. 1983). “Influence of Base Slant on the Wake Structure and Drag of Road Vehicles”. en. In: *Journal of Fluids Engineering* 105.4, pp. 429–434. ISSN: 0098-2202, 1528-901X. DOI: 10.1115/1.3241024.

Barlow, Jewel B., William H. Rae, and Alan Pope (1999). *Low-speed wind tunnel testing*. 3rd ed. New York: Wiley. ISBN: 978-0-471-55774-6.

Bartlett, G. E. and R. J. Vidal (Aug. 1955). “Experimental Investigation of Influence of Edge Shape on the Aerodynamic Characteristics of Low Aspect Ratio Wings at Low Speeds”. en. In: *Journal of the Aeronautical Sciences* 22.8, pp. 517–533. ISSN: 1936-9956. DOI: 10.2514/8.3391.

Bartol, I K et al. (Mar. 2008). “Evidence of self-correcting spiral flows in swimming boxfishes”. en. In: *Bioinspiration & Biomimetics* 3.1, p. 014001. ISSN: 1748-3182, 1748-3190. DOI: 10.1088/1748-3182/3/1/014001.

Bartol, I. K. et al. (Nov. 2002). “Flow Patterns Around the Carapaces of Rigid-bodied, Multi-propulsor Boxfishes (Teleostei: Ostraciidae)”. en. In: *Integrative and Comparative Biology* 42.5, pp. 971–980. ISSN: 1540-7063, 1557-7023. DOI: 10.1093/icb/42.5.971.

Bartol, Ian K., Morteza Gharib, Paul W. Webb, et al. (Jan. 2005). “Body-induced vortical flows: a common mechanism for self-corrective trimming control in boxfishes”. en. In: *Journal of Experimental Biology* 208.2, pp. 327–344. ISSN: 1477-9145, 0022-0949. DOI: 10.1242/jeb.01356.

Bartol, Ian K., Morteza Gharib, Daniel Weihs, et al. (Feb. 2003). “Hydrodynamic stability of swimming in ostraciid fishes: role of the carapace in the smooth trunkfish *Lactophrys triqueter* (Teleostei:Ostraciidae)”. en. In: *Journal of Experimental Biology* 206.4, pp. 725–744. ISSN: 1477-9145, 0022-0949. DOI: 10.1242/jeb.00137.

Batchelor, G. K. (2000). *An introduction to fluid dynamics*. Cambridge Mathematical Library. Cambridge: Cambridge University Press.

Bollt, Scott A., Samuel H. Foxman, and Morteza Gharib (Apr. 2025). “RapidPIV: Full Flow-Field kHz PIV for Real-Time Display and Control”. en. In: arXiv:2504.17987. arXiv:2504.17987 [physics]. DOI: 10.48550/arXiv.2504.17987.

Boute, Pim G., Sam Van Wassenbergh, and Eize J. Stamhuis (Apr. 2020). “Modulating yaw with an unstable rigid body and a course-stabilizing or steering caudal fin in the yellow boxfish (Ostracion cubicus)”. en. In: *Royal Society Open Science* 7.4, p. 200129. ISSN: 2054-5703. DOI: 10.1098/rsos.200129.

Breuer, Kenneth et al. (2022). “Design and performance of an ultra-compact, low-speed, low turbulence level, wind tunnel for aerodynamic and animal flight experiments”. en. In: *Experiments in Fluids* 63.11, p. 169. ISSN: 0723-4864, 1432-1114. DOI: 10.1007/s00348-022-03519-1.

Brown, C. E. and W. H. Michael (Oct. 1954). "Effect of Leading-Edge Separation on the Lift of a Delta Wing". en. In: *Journal of the Aeronautical Sciences* 21.10, pp. 690–694. ISSN: 1936-9956. DOI: 10.2514/8.3180.

Bruun, Hans H. (1995). *Hot-wire anemometry: principles and signal analysis.* Oxford science publications. Oxford: Oxford University Press. ISBN: 0198563426.

– (1996). "Hot-film anemometry in liquid flows". en. In: *Measurement Science and Technology* 7.10, pp. 1301–1312. DOI: 10.1088/0957-0233/7/10/003.

Cattafesta, Louis, Chris Bahr, and Jose Mathew (2010). "Fundamentals of wind-tunnel design". en. In: *Encyclopedia of Aerospace Engineering*. Ed. by Richard Blockley and Wei Shyy. 1st ed. New York: Wiley. ISBN: 978-0-470-75440-5 978-0-470-68665-2. DOI: 10.1002/9780470686652.eae532.

Charters, A. C. and S. Miles Anderson (1980). "Low-velocity water tunnel for biological research". In: *J. Hydronautics* 14.1. DOI: https://doi.org/10.2514/3.63180.

Chen, Lin, Yueri Cai, and Shusheng Bi (Aug. 2023). "Central Pattern Generator (CPG)-Based Locomotion Control and Hydrodynamic Experiments of Synergistical Interaction between Pectoral Fins and Caudal Fin for Boxfish-like Robot". en. In: *Biomimetics* 8.4, p. 380. ISSN: 2313-7673. DOI: 10.3390/biomimetics8040380.

Christ, Robert D. and Robert L. Wernli Sr. (2014). *The ROV manual: a user guide for remotely operated vehicles*. 2nd ed. Oxford: Butterworth-Heinemann.

Da Silva Ássi, G et al. (2005). "Design, assembling and verification of a circulating water channel facility for fluid dynamics experiments". In: *Proceedings of COBEM 2005 18th International Congress of Mechanical Engineering, by ABCM*, pp. 6–11.

Delery, Jean M. (Jan. 1994). "Aspects of vortex breakdown". en. In: *Progress in Aerospace Sciences* 30.1, pp. 1–59. ISSN: 03760421. DOI: 10.1016/0376-0421(94)90002-7.

Dougherty, Christopher (2022). "On the experimental simulation of atmospheric-like disturbances near the surface". en. Dissertation. California Institute of Technology. DOI: 10.7907/293w-ev66.

Earnshaw, P B and J A Lawford (1964). "Low-Speed Wind-Tunnel Experiments on a Series of Sharp-Edged Delta Wings". en. In.

Eldredge, Jeff D. and Anya R. Jones (Jan. 2019). "Leading-Edge Vortices: Mechanics and Modeling". en. In: *Annual Review of Fluid Mechanics* 51.1, pp. 75–104. ISSN: 0066-4189, 1545-4479. DOI: 10.1146/annurev-fluid-010518-040334.

Erm, Lincoln P and Michael Ol (2012). *An Assessment of the Usefulness of Water Tunnels for Aerodynamic Investigations*. en. DSTO-TR-2803. Victoria, Australia.

Fedorov, Andriy et al. (Nov. 2012). "3D Slicer as an image computing platform for the Quantitative Imaging Network". en. In: *Magnetic Resonance Imaging* 30.9, pp. 1323–1341. ISSN: 0730725X. DOI: 10.1016/j.mri.2012.05.001.

Gad-el-Hak, Mohamed and Ron F. Blackwelder (June 1985). "The discrete vortices from a delta wing". en. In: *AIAA Journal* 23.6, pp. 961–962. ISSN: 0001-1452, 1533-385X. DOI: 10.2514/3.9016.

Gordnier, Raymond and Miguel Visbal (Jan. 2003). "Higher-Order Compact Difference Scheme Applied to Low Sweep Delta Wing Flow". en. In: *41st Aerospace Sciences Meeting and Exhibit*. Reno, Nevada: American Institute of Aeronautics and Astronautics. ISBN: 978-1-62410-099-4. DOI: 10.2514/6.2003-620.

Gordon, Malcolm S. et al. (Nov. 2000). "Boxfishes as Unusually Well-Controlled Autonomous Underwater Vehicles". en. In: *Physiological and Biochemical Zoology* 73.6, pp. 663–671. ISSN: 1522-2152, 1537-5293. DOI: 10.1086/318098.

Gordon, Robert and Mohammed S. Imbabi (1998). "CFD simulation and experimental validation of a new closed circuit wind/water tunnel design". en. In: *Journal of Fluids Engineering* 120.2, pp. 311–318. ISSN: 0098-2202, 1528-901X. DOI: 10.1115/1.2820650.

Grellmann, Hans Werner (1964). "An Experimental Study of the Separated Flow Field About Slender Delta Wings of Triangular Cross Section". PhD thesis. California Institute of Technology.

Gursul, I., R. Gordnier, and M. Visbal (Oct. 2005). "Unsteady aerodynamics of nonslender delta wings". en. In: *Progress in Aerospace Sciences* 41.7, pp. 515–557. ISSN: 03760421. DOI: 10.1016/j.paerosci.2005.09.002.

Gursul, Ismet (Mar. 2005). "Review of Unsteady Vortex Flows over Slender Delta Wings". en. In: *Journal of Aircraft* 42.2, pp. 299–319. ISSN: 0021-8669, 1533-3868. DOI: 10.2514/1.5269.

Henderson, W. P. (1976). *Effects of wing leading-edge radius and Reynolds number on longitudinal aerodynamic characteristics of highly swept wing-body configurations at subsonic speeds*. Tech. rep. NASA-TN-D-8361. Hampton, Va: NASA Langely Research Center.

Hirschel, Ernst Heinrich et al. (2021). *Separated and Vortical Flow in Aircraft Wing Aerodynamics: Basic Principles and Unit Problems*. en. Berlin, Heidelberg: Springer Berlin Heidelberg. ISBN: 978-3-662-61326-9 978-3-662-61328-3. DOI: 10.1007/978-3-662-61328-3.

Hummel, Deitrich (1981). *Experimental investigation of the flow on the suction side of a thin Delta wing*. Tech. rep. NASA-TM-75897. NASA.

Jia-Ying, Wang et al. (2015). "Multiple-fan active control wind tunnel for outdoor near-surface airflow simulation". en. In: *2015 34th Chinese Control Conference (CCC)*. Hangzhou, China: IEEE, pp. 5959–5964. ISBN: 978-988-15638-9-7. DOI: 10.1109/ChiCC.2015.7260572.

Johnson, Eric and Jamey Jacob (2009). "Development and testing of a gust and shear wind tunnel for NAVs and MAVs". en. In: *47th AIAA Aerospace Sciences Meeting including The New Horizons Forum and Aerospace Exposition*. Orlando, Florida: American Institute of Aeronautics and Astronautics. ISBN: 978-1-60086-973-0. DOI: 10.2514/6.2009-64.

Kegelman, Jerome and Frederick Roos (Jan. 1989). "Effects of leading-edge shape and vortex burst on the flowfield of a70-degree-sweep delta-wing". en. In: *27th Aerospace Sciences Meeting*. Reno,NV,U.S.A.: American Institute of Aeronautics and Astronautics. DOI: 10.2514/6.1989-86.

Kim, Daegyoum et al. (Dec. 2013). "Flapping dynamics of an inverted flag". en. In: *Journal of Fluid Mechanics* 736, R1. ISSN: 0022-1120, 1469-7645. DOI: 10.1017/jfm.2013.555.

Kirby, D A and D L I Kirkpatrick (1971). "An Experimental Investigation of the Effect of Thickness on the Subsonic Longitudinal Stability Characteristics of Delta Wings of 70 Deg Sweep-Back". en. In.

Kirkpatrick, D I I (1965). *Investigation of the Normal Force Characteristics of Slender Delta Wings with Various Rhom bit Cross-Sections in Subsonic Conical Flow*. en. Tech. rep.

Kirkpatrick, D. L. I. and J. D. Field (1966). *EXPERIMENTAL INVESTIGATION OF THE POSITIONS OF THE LEADINC-EDGE VORTICES ABOVE SLENDER DELTA WINGS WITH VARIOUS RHOMBIC CROSS-SECTIONS IN SUBSONIC CONICAL FLOW*. Tech. rep. C.P. No. 925. Ministry of Aviation.

Kodati, Parasar and Xinyan Deng (Oct. 2006). "Towards the Body Shape Design of a Hydrodynamically Stable Robotic Boxfish". en. In: *2006 IEEE/RSJ International Conference on Intelligent Robots and Systems*. Beijing, China: IEEE, pp. 5412–5417. ISBN: 978-1-4244-0258-8. DOI: 10.1109/IROS.2006.282108.

L'Ecuyer, Austin (2021). "Turbulence Generated in a Multi-Fan Wind Tunnel". en. Dissertation. McGill University.

Lambourne, N. C. and D. W. Bryer (1962). *The Bursting of Leading-Edge Vortices–Some Observations and Discussion of the Phenomenon*. en. Reports and Memoranda No. 3282. London, U.K.

Lee, G.H. (1959). *Reduction of Lift-Dependent Drag with Separated Flow*. Tech. rep. C. P. No. 593. Ministry of Aviation.

Lee, Mario and Chih-Ming Ho (Sept. 1990). "Lift Force of Delta Wings". en. In: *Applied Mechanics Reviews* 43.9, pp. 209–221. ISSN: 0003-6900, 2379-0407. DOI: 10.1115/1.3119169.

Li, Songqi et al. (2023). "Aerodynamic Characterization of a Fan-Array Wind Generator". en. In: *AIAA Journal*, pp. 1–11. ISSN: 0001-1452, 1533-385X. DOI: 10.2514/1.J063114.

Liska, Sebastian and Tim Colonius (Dec. 2014). "A parallel fast multipole method for elliptic difference equations". en. In: *Journal of Computational Physics* 278, pp. 76–91. ISSN: 0021-9991. DOI: 10.1016/j.jcp.2014.07.048.

– (Feb. 2017). "A fast immersed boundary method for external incompressible viscous flows using lattice Green's functions". en. In: *Journal of Computational Physics* 331, pp. 257–279. ISSN: 0021-9991. DOI: 10.1016/j.jcp.2016.11.034.

Lu, Yuan, Gong Xin Shen, and Guo Jun Lai (Dec. 2006). "Dual leading-edge vortices on flapping wings". en. In: *Journal of Experimental Biology* 209.24, pp. 5005–5016. ISSN: 1477-9145, 0022-0949. DOI: 10.1242/jeb.02614.

Lucca-Negro, O and T O'Doherty (Jan. 2001). "Vortex breakdown: a review". en. In: *Progress in Energy and Combustion Science* 27.4, pp. 431–481. ISSN: 03601285. DOI: 10.1016/S0360-1285(00)00022-8.

Luckring, James M. and Dietrich Hummel (Jan. 2013). "What was learned from the new VFE-2 experiments". en. In: *Aerospace Science and Technology* 24.1, pp. 77–88. ISSN: 12709638. DOI: 10.1016/j.ast.2011.07.012.

Mangler, K. W. and J. H. B. Smith (May 1959). "A theory of the flow past a slender delta wing with leading edge separation". en. In: *Proceedings of the Royal Society of London. Series A. Mathematical and Physical Sciences* 251.1265, pp. 200–217. ISSN: 0080-4630, 2053-9169. DOI: 10.1098/rspa.1959.0102.

Mann, Steve et al. (2023). "Smart paddleboard and other assistive veyances". en. In: *2022 IEEE International Conference on Cyborg and Bionic Systems (CBS)*. Wuhan, China: IEEE, pp. 298–305. ISBN: 978-1-66549-028-3. DOI: 10.1109/CBS55922.2023.10115303.

McCutchan, Aubrey L. and Blair A. Johnson (2023). "An experimental apparatus for generating homogeneous isotropic turbulence". en. In: *Experiments in Fluids* 64.11, p. 177. ISSN: 0723-4864, 1432-1114. DOI: 10.1007/s00348-023-03711-x.

Mehta, R.D. and P. Bradshaw (1979). "Design rules for small low speed wind tunnels". en. In: *The Aeronautical Journal* 83.827, pp. 443–453. ISSN: 0001-9240, 2059-6464. DOI: 10.1017/S0001924000031985.

Morel, Thomas (Feb. 1978). "Aerodynamic Drag of Bluff Body Shapes Characteristic of Hatch-Back Cars". en. In: p. 780267. DOI: 10.4271/780267.

Moreto, Jose R. and Xiaofeng Liu (2020). "SDSU water tunnel test section flow quality characterization". en. In: *AIAA Scitech 2020 Forum*. Orlando, FL: American Institute of Aeronautics and Astronautics. ISBN: 978-1-62410-595-1. DOI: 10.2514/6.2020-0030.

Nishi, A, H Miyagi, and K Higuchi (1993). "A computer-controlled wind tunnel". In: *Journal of Wind Engineering and Industrial Aerodynamics* 46, pp. 837–846. DOI: https://doi.org/10.1016/0167-6105(93)90360-Z.

Nishi, A. et al. (1997). "Turbulence control in multiple-fan wind tunnels". en. In: *Journal of Wind Engineering and Industrial Aerodynamics* 67-68, pp. 861–872. ISSN: 01676105. DOI: 10.1016/S0167-6105(97)00124-4.

Noca, Flavio et al. (2019). "Wind and weather facility for testing free-flying drones". en. In: *AIAA Aviation 2019 Forum*. Dallas, Texas: American Institute of Aeronautics and Astronautics. ISBN: 978-1-62410-589-0. DOI: 10.2514/6.2019-2861.

Nutter, J. (Apr. 1981). "Leading-edge separation from a thick, conical, slender wing at small angles of incidence". In: *Journal of Engineering Mathematics* 15.2.

Ol, Michael (2001). “The passage toward stall of nonslender delta wings at low Reynolds number”. PhD thesis. Pasadena, CA: California Institute of Technology.

Ol, Michael V. and Morteza Gharib (Jan. 2003). “Leading-Edge Vortex Structure of Nonslender Delta Wings at Low Reynolds Number”. en. In: *AIAA Journal* 41.1, pp. 16–26. ISSN: 0001-1452, 1533-385X. DOI: 10.2514/2.1930.

Olejnik, Diana A. et al. (2022). “An experimental study of wind resistance and power consumption in MAVs with a low-speed multi-fan wind system”. en. In: *2022 International Conference on Robotics and Automation (ICRA)*. Philadelphia, PA, USA: IEEE, pp. 2989–2994. ISBN: 978-1-72819-681-7. DOI: 10.1109/ICRA46639.2022.9811834.

Owen, K and D J Peake (1986). *Vortex Breakdown and Control Experiments in the Ames-Dryden Water Tunnel*. en. NASA-TM-89410. Moffet Field, Ca.

Persen, Leif N. and Lars R. Saetran (1983). “Hot-film measurements in a water tunnel”. en. In: *Journal of Hydraulic Research* 21.5, pp. 379–387. ISSN: 0022-1686, 1814-2079. DOI: 10.1080/00221688309499459.

Pinapatruni, Gangadhar V. R. et al. (2024). “Characterization of the new open surface recirculating water tunnel facility at the Indian Institute of Technology Kharagpur”. en. In: *Fluid Mechanics and Fluid Power, Volume 7*. Series Title: Lecture Notes in Mechanical Engineering. Singapore: Springer Nature Singapore, pp. 243–255. ISBN: 978-981-9970-46-9 978-981-9970-47-6. DOI: 10.1007/978-981-99-7047-6_18.

Polhamus, E C (1966). “A concept of the vortex lift of sharp-edge delta wings based on a leading-edge-suction analogy”. en. In: p. 18.

Pullin, D I (1975). “Calculations of the Steady Conical Flow past a Yawed Slender Delta Wing with Leading-Edge Separation”. en. In.

Qiu, Hongcheng et al. (Jan. 2023). “Analysis of Heading Stability due to Interactions between Pectoral and Caudal Fins in Robotic Boxfish Locomotion”. en. In: *Journal of Bionic Engineering* 20.1, pp. 390–405. ISSN: 1672-6529, 2543-2141. DOI: 10.1007/s42235-022-00271-4.

Raffel, Markus et al. (2018). *Particle Image Velocimetry: A Practical Guide*. en. Cham: Springer International Publishing. ISBN: 978-3-319-68851-0 978-3-319-68852-7. DOI: 10.1007/978-3-319-68852-7.

Rolfe, Sara et al. (Oct. 2021). “SlicerMorph: An open and extensible platform to retrieve, visualize and analyse 3D morphology”. en. In: *Methods in Ecology and Evolution* 12.10, pp. 1816–1825. ISSN: 2041-210X, 2041-210X. DOI: 10.1111/2041-210X.13669.

Rose, E. Ernest et al. (1955). “Direct Resin Filling Materials: Coefficient of Thermal Expansion and Water Sorption of Polymethyl Methacrylate”. en. In: *Journal of Dental Research* 34.4, pp. 589–596. ISSN: 0022-0345, 1544-0591. DOI: 10.1177/00220345550340041501.

Sabatino, Daniel R. and Rijan Maharjan (2015). “Characterizing the formation and regeneration of hairpin vortices in a laminar boundary layer”. en. In: *Physics of Fluids* 27.12, p. 124104. ISSN: 1070-6631, 1089-7666. DOI: 10.1063/1.4936138.

Sader, John E. et al. (Aug. 2024). "The starting vortices generated by bodies with sharp and straight edges in a viscous fluid". en. In: *Journal of Fluid Mechanics* 992. ISSN: 0022-1120, 1469-7645. DOI: 10.1017/jfm.2024.515.

Sargison, J E et al. (2009). "Design and calibration of a water tunnel for skin friction research". en. In: *Australian Journal of Mechanical Engineering* 7.2, pp. 111–124. ISSN: 1448-4846, 2204-2253. DOI: 10.1080/14484846.2009.11464585.

Schlicting, Herman and Erich Truckenbrodt (1979). *Aerodynamics of the airplane*. Trans. by Heinrich J. Ramm. McGraw-Hill.

Sharifi Ghazijahani, Mohammad and Mehmet Metin Yavuz (May 2019). "Effect of thickness-to-chord ratio on aerodynamics of non-slender delta wing". en. In: *Aerospace Science and Technology* 88, pp. 298–307. ISSN: 12709638. DOI: 10.1016/j.ast.2019.03.033.

Shaw, G. W. (July 1970). "Aerodynamic Characteristics of Thick Sharp Edged Cropped Delta and Gothic Wings giving Low Lift-Dependent Drag". en. In: *The Aeronautical Journal* 74.715, pp. 586–589. ISSN: 0001-9240, 2059-6464. DOI: 10.1017/S0001924000049101.

Shih, C. and Z. Ding (Jan. 1996). "Unsteady structure of leading-edge vortex flow over a delta wing". en. In: *34th Aerospace Sciences Meeting and Exhibit*. Reno,NV,U.S.A.: American Institute of Aeronautics and Astronautics. DOI: 10.2514/6.1996-664.

Smith, J H B (1971). "Calculations of the Flow over Thick, Conical, Slender Wings with Leading-Edge Separation". en. In.

– (July 1968). "Improved calculations of leading-edge separation from slender, thin, delta wings". en. In: *Proceedings of the Royal Society of London. Series A. Mathematical and Physical Sciences* 306.1484, pp. 67–90. ISSN: 0080-4630, 2053-9169. DOI: 10.1098/rspa.1968.0138.

Sovran, Gino, Thomas Morel, and William T. Mason, eds. (1978). *Aerodynamic Drag Mechanisms of Bluff Bodies and Road Vehicles*. en. Boston, MA: Springer US. ISBN: 978-1-4684-8436-6 978-1-4684-8434-2. DOI: 10.1007/978-1-4684-8434-2.

Spall, R. E., T. B. Gatski, and C. E. Grosch (Jan. 1987). *On a criteria for vortex breakdown*. en. Tech. rep. NASA-CB-178232. NASA.

Taylor, Gordon, Thorsten Schnorbus, and Ismet Gursul (June 2003). "An Investigation of Vortex Flows over Low Sweep Delta Wings". en. In: *33rd AIAA Fluid Dynamics Conference and Exhibit*. Orlando, Florida: American Institute of Aeronautics and Astronautics. ISBN: 978-1-62410-095-6. DOI: 10.2514/6.2003-4021.

Traub, Lance W. (July 2000a). "Aerodynamic Characteristics of Spanwise Cambered Delta Wings". en. In: *Journal of Aircraft* 37.4, pp. 714–724. ISSN: 0021-8669, 1533-3868. DOI: 10.2514/2.2657.

– (Mar. 2000b). "Effects of Anhedral and Dihedral on a 75-deg Sweep Delta Wing". en. In: *Journal of Aircraft* 37.2, pp. 302–312. ISSN: 0021-8669, 1533-3868. DOI: 10.2514/2.2594.

Traub, Lance W., Brian Moeller, and Othon Rediniotis (July 1998). "Low-Reynolds-Number Effects on Delta-Wing Aerodynamics". en. In: *Journal of Aircraft* 35.4, pp. 653–656. ISSN: 0021-8669, 1533-3868. DOI: 10.2514/2.2352.

Variano, Evan A., Eberhard Bodenschatz, and Edwin A. Cowen (2004). "A random synthetic jet array driven turbulence tank". en. In: *Experiments in Fluids* 37.4, pp. 613–615. ISSN: 0723-4864, 1432-1114. DOI: 10.1007/s00348-004-0833-z.

Veismann, Marcel et al. (2021). "Low-density multi-fan wind tunnel design and testing for the Ingenuity Mars Helicopter". en. In: *Experiments in Fluids* 62.9, p. 193. ISSN: 0723-4864, 1432-1114. DOI: 10.1007/s00348-021-03278-5.

Verhaagen, Nick (Jan. 2011). "Flow over 50o Delta Wings with Different Leading-Edge Radii". en. In: *49th AIAA Aerospace Sciences Meeting including the New Horizons Forum and Aerospace Exposition*. Orlando, Florida: American Institute of Aeronautics and Astronautics. ISBN: 978-1-60086-950-1. DOI: 10.2514/6.2011-991.

W. H. Wentz Jr. and D. L. Kohlman (1971). "Vortex Breakdown on Slender Sharp-Edged Wings". In: 8.3.

Walker, Jeffrey A. (Nov. 2000). "Does a Rigid Body Limit Maneuverability?" en. In: *Journal of Experimental Biology* 203.22, pp. 3391–3396. ISSN: 0022-0949, 1477-9145. DOI: 10.1242/jeb.203.22.3391.

Wassenbergh, S. van et al. (Feb. 2015). "Boxfish swimming paradox resolved: forces by the flow of water around the body promote manoeuvrability". en. In: *Journal of The Royal Society Interface* 12.103, p. 20141146. ISSN: 1742-5689, 1742-5662. DOI: 10.1098/rsif.2014.1146.

Willert, Christian (Dec. 1997). "Stereoscopic digital particle image velocimetry for application in wind tunnel flows". en. In: *Measurement Science and Technology* 8.12, pp. 1465–1479. ISSN: 0957-0233, 1361-6501. DOI: 10.1088/0957-0233/8/12/010.

Yoda, M. and L. Hesselink (Dec. 1990). "A three-dimensional visualization technique applied to flow around a delta wing". en. In: *Experiments in Fluids* 10-10.2-3, pp. 102–108. ISSN: 0723-4864, 1432-1114. DOI: 10.1007/BF00215017.

Yu, Ke, Benedikt Dorschner, and Tim Colonius (June 2022). "Multi-resolution lattice Green's function method for incompressible flows". en. In: *Journal of Computational Physics* 459, p. 110845. ISSN: 0021-9991. DOI: 10.1016/j.jcp.2021.110845.

Zahari, M and S S Dol (2015). "Design and development of low-cost water tunnel for educational purpose". en. In: *IOP Conference Series: Materials Science and Engineering* 78, p. 012040. ISSN: 1757-899X. DOI: 10.1088/1757-899X/78/1/012040.

Zigunov, Fernando, Prabu Sellappan, and Farrukh Alvi (June 2020). "Reynolds number and slant angle effects on the flow over a slanted cylinder afterbody". en. In: *Journal of Fluid Mechanics* 893, A11. ISSN: 0022-1120, 1469-7645. DOI: 10.1017/jfm.2020.214.

TURBULENCE POWER SPECTRA AND BUILDING VIBRATIONS

As referenced in section 2.1, turbulence measurements in the water tunnel were contaminated somewhat by building vibrations. A power spectrum of the CTA voltage at various tunnel speeds shows a consistent set of peaks from around 15-30Hz, which appear unchanged at all tunnel speeds, including with thrusters fully turned off (figure A.1). Flow-related peaks should be expected to change change frequency with freestream velocity, so these are more likely to correspond to some other signal in the measurement system. A back of the envelope estimate assuming a Strouhal number of 0.2 and freestream speed of 10cm/s finds that frequencies in excess of 16Hz require length scales on the order of about a millimeter or smaller.

The source of these $> 16Hz$ frequency peaks can be traced back to vibrations in the laboratory. The water tunnel's structural setup includes a superstructure suspended from the ceiling, which supports elements within the tank and serves as the mounting frame for measurement probes, such as the hot-film probe used in turbulence measurements. To assess the influence of structural vibrations, figure A.2 compares the power spectra of four measurements to identify the source of these vibrations.

The black curve in the power spectrum represents data from the hot-film CTA probe, rigidly mounted to the tunnel superstructure. These measurements were taken with the thruster array

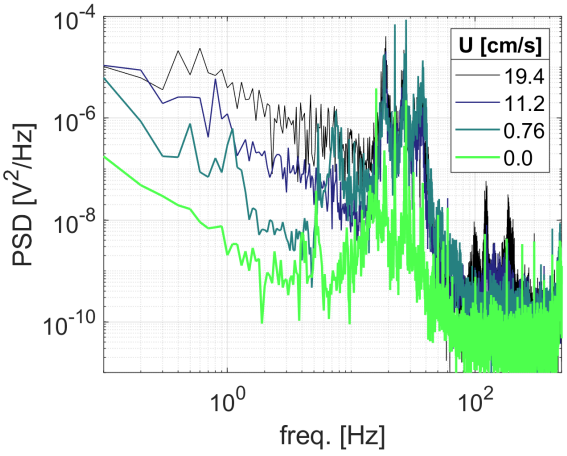

Figure A.1 Power spectrum of freestream flow at center of test section at four different speeds.

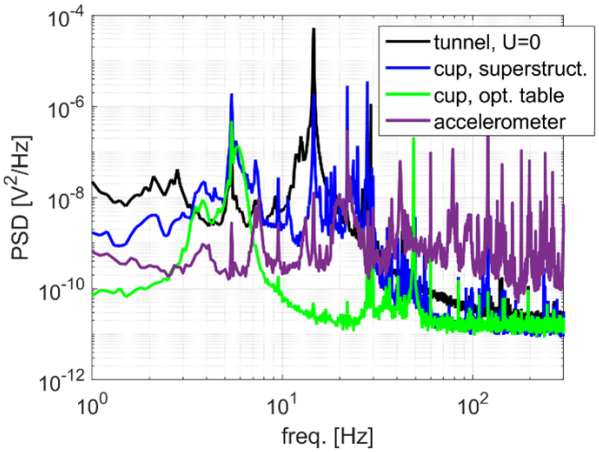

Figure A.2 Caption

powered off and the water in a nominally quiescent state after settling overnight.

For a zero-flow baseline in the absence of structural vibrations, a 125mm diameter cylindrical cup was filled with approximately 0.5 L of water, placed on an optical table with S-2000 laminar flow isolator legs, and covered to block airflow disturbances from HVAC systems. Hot-film measurements from this setup are shown in green and blue on the power spectrum plot. The green curve represents measurements when the probe is mounted on the optical table itself, while the blue curve reflects measurements with the probe mounted from a corner of the tunnel's superstructure.

Mounting the probe on the superstructure yields a similar power spectrum to the measurements in the quiescent tunnel, whereas mounting the probe on the optical table reduces the peaks in the spectrum by several orders of magnitude, particularly in the 10 to 50 Hz range. All the hot-film measurements share a similar low-frequency peak around 5 Hz. At this frequency, vibrations are only attenuated about 80% by the optical table per its specification.

Further supporting the link between vibration and these frequency peaks, the purple curve in the power spectrum displays data from an accelerometer mounted on the tunnel superstructure. The frequencies below 50 Hz in the accelerometer data align closely with those observed in both the quiescent tunnel and superstructure-mounted cup measurements. The power spectrum of load cell measurements described in section 4.4 shows similar peaks as well.